Doctoral Dissertations   Graduate School

12-2018

Investigating the evolution of microtextured region in Ti-6242 using FE-FFT multiscale modeling method

Ran Ma
University of Tennessee, rma8@vols.utk.edu

Follow this and additional works at: https://trace.tennessee.edu/utk_graddiss

To the Graduate Council:

I am submitting herewith a dissertation written by Ran Ma entitled "Investigating the evolution of microtextured region in Ti-6242 using FE-FFT multiscale modeling method." I have examined the final electronic copy of this dissertation for form and content and recommend that it be accepted in partial fulfillment of the requirements for the degree of Doctor of Philosophy, with a major in Civil Engineering.

<div align="right">Timothy Truster, Major Professor</div>

We have read this dissertation and recommend its acceptance:

Reza Abedi, Khalid Alshibli, Dayakar Penumadu

<div align="right">Accepted for the Council:</div>

<div align="right">Dixie L. Thompson</div>

<div align="right">Vice Provost and Dean of the Graduate School</div>

(Original signatures are on file with official student records.)

Investigating the evolution of microtextured region in Ti-6242 using FE-FFT multiscale modeling method

A Dissertation Presented for the

Doctor of Philosophy

Degree

The University of Tennessee, Knoxville

Ran Ma

December 2018

To my mom

Acknowledgments

I want to begin by giving my greatest thanks to my PhD advisor and mentor, Dr Timothy Truster, for guiding me into computational mechanics and helping me to build up my confidence in this area. His rigorous research attitude and long-lasting working passion will always remind me to challenge difficult scientific problems.

Additionally, I wish to acknowledge the comments of my committee members, Dr. Reza Abedi, Dr. Khalid Alshibli, and Dr. Dayakar Penumadu, for helping me to organize and strengthen my dissertation.

During the first year of my PhD study, I collaborated with Mr. Stephen Puplampu and Dr. Dayakar Penumadu on investigating the post fire behavior of aluminum alloy. After that, I also collaborated with Mr. Amirsalar Moslehy and Dr. Khalid Alshibli on investigating the creep response of rock salt. At the same time, I performed the major part of my PhD study based on the preliminary experimental studies from Dr. Adam Pilchak and Dr. Lee Semiatin. I am thankful for the helpful discussions with them, from which I learned the potential applications of my investigation.

I also wish to express my deepest gratitude to the Chancellor Fellowship I have received, which enabled me to conduct my investigations.

I would also like to thank my colleagues for their kindly help, Mr. Omar Nassif, Mr. Sunday Aduloju, and Ms. Elina Geut.

I am also thankful for my roommates, Ms. Tianxue Yang and Ms. Dan Huang, who turned my monochrome PhD life to be colorful. I was not able to finish my PhD program in such an optimistic attitude without your company.

And last but not least, I am thankful to my mom for her love and support for pursuing my dream.

Abstract

Titanium alloy Ti-6242 (Ti-6Al-2Sn-4Zr-2Mo) is frequently used in the high-pressure compressor of aero engines due to its excellent resistance to fatigue and creep failure at high temperature. While exhibiting high strength at elevated temperatures, it is susceptible to dwell fatigue at temperatures below 473 K due in part to the presence of microtextured regions (MTRs), also known as macrozones. MTRs are clusters of similarly orientated alpha particles, which form during alpha/beta processing and remain stable even after large deformation. The major objective of this dissertation is to quantify the evolution of MTRs under different thermomechanical processing parameters, and predict the optimal processing parameters to eliminate the MTRs.

Idealized MTRs with pure initial orientation are first employed as the benchmark case to investigate the loading direction effect on its breakdown efficiency. Three high-temperature compression processes are simulated with different loading directions using crystal plasticity finite element method, and the results are validated against high-temperature compression experiments and EBSD measurement. The evolution of equivalent plastic strain, accumulated shear strain, and misorientation distribution is analyzed in detail to reveal the relationship between loading direction and MTR breakdown efficiency. Lastly, the reorientation velocity divergence of arbitrary loading direction is expressed in the Rodrigues' space in order to predict the optimal processing parameters for MTR elimination.

The MTR breakdown efficiency also depends on the morphology and its position within the specimen. Two different length scales have to be analyzed in order to consider both factors, which present great challenge to the numerical simulation. In this dissertation, a high-efficient FE-FFT multiscale modeling framework is derived and developed to overcome this challenge. The Fourier-Galerkin method is utilized to solve the microscale unit cell

problem, while total Lagrangian finite element is used to solve the macroscopic boundary value problems. Several numerical improvements are derived and implemented to further improve its numerical efficiency, including consistent linearization, consistent homogenized tangent stiffness, and inexact Newton method. A series of numerical studies is conducted to investigate the accuracy, efficiency, and robustness of this algorithm.

Table of Contents

List of Tables

List of Figures

Chapter 1

Introduction

1.1 Motivation

The titanium alloy Ti-6242 (Ti-6Al-2Sn-4Zr-2Mo) has been the structural material of choice for use in high-pressure compressors for gas turbine engines of aircraft due to its high strength-to-weight ratio and excellent mechanical properties. Jet engine efficiency is highly correlated to operating temperature, and Ti-6242 has demonstrated excellent creep and fatigue resistance at high temperatures up to 873 K. Although possessing excellent high temperature performance, this titanium alloy is susceptible to creep fatigue failure under dwell loading below 473 K. Such detrimental performance is mainly caused by the microtextured regions (MTRs), which are clusters of α particles with similar orientation. This kind of microstructure forms during the α/β processing, and remains stable even under large strain processing when the α particles are significantly refined. Therefore, novel processing techniques are required to break down the MTRs in order to improve the dwell fatigue performance of this alloy. Previous experimental investigations have revealed that MTR behavior under α/β processing depends on the loading direction, the morphology of MTRs, and the position of MTRs within the specimen. Considering so many influencing factors at different length scales, numerical simulation is a powerful tool to fully quantify the MTR breakdown efficiency and predict the optimal processing parameters. However, the breakdown process of MTRs is very complicate and involves different length scales, which presents great challenge to the numerical simulations.

The main objective of this dissertation is to derive and develop a high-performance FE-FFT multiscale modeling framework, and further apply this framework to investigate the MTR behavior under different loading conditions. The behavior of idealized MTRs with pure initial orientation is first constructed to investigate the effect of loading direction on its breakdown efficiency. In order to further incorporate the effect of MTR morphology and its position within the specimen, a FE-FFT multiscale modeling framework is developed. In the microscale, the finite strain Fourier-Galerkin method is utilized, which is more efficient than finite element method and other FFT-based methods, making it suitable for the multiscale modeling framework. The resulting framework serves as an efficient platform to investigate the microstructure evolution under macroscopic loading.

1.1.1 Formation, evolution and elimination of microtextured region

Ti-6242 is widely used as the high-pressure compressors for gas turbine engines mainly because of its high resistance to fatigue and creep failure under high temperatures. Although pocessing excellent high-temperature performance, this alloy is susceptible to fatigue failure under dwell loading mainly because of microtextured regions (MTRs) [89]. The MTRs are clusters of similarly orientated grains, which remain stable during the α/β processing [21, 24, 44, 20]. After high-temperature mechanical processing, significantly refined $\alpha_p + \alpha_s$ microstructures are generated, but EBSD results show that particles with similar orientation are still clustered [21, 44, 20]. The MTR size depends on the processing parameters [67], and are usually between 0.1 mm and 1 mm depends on the thermal-mechanical processing procedures. MTRs with "hard" orientation are most detrimental, where c-axis is aligned with the loading direction and stress concentration occurs at the MTR boundaries. In this case, fatigue cracks grow an order of magnitude faster than typical fatigues, leading to a significantly reduced fatigue life [2, 68]. Therefore, it is necessary eliminate the MTRs within this alloy to improve its low temperature dwell fatigue behavior.

Several reasons can account for the stable MTRs under traditional α/β processing:

- The Burgers orientation relation between α phase and β phase remains unaltered even under large strain α/β processing [21, 24, 44];

- The variant selection of α_s laths nucleated after the cooling is influenced by the existing α_p particles [21, 44, 20];

- Limited deformation patterns of crystals with hexagonal closed pack structure [44, 4];

- Nucleated grains during dynamic recrystallization are usually aligned with the parent grains [44, 4].

Recently, it is reported that the behaviors of MTRs under α/β processing depends on several processing parameters: the loading direction [22], the morphologh of MTRs [4], and the position of MTRs within the specimen [22]. However, such influence is difficult to quantify experimentally, and only limited numerical simulations are performed to invetigate the behavior of MTRs under different loading conditions. For example, visco-plastic self-consistent (VPSC) method is used to investigate the relationship between microtexture and macrotexture in Ti-6Al-4V [60].

In this dissertation, idealized MTRs with pure initial orientation is first employed to investigate the effect of loading direction on its breakdown efficiency. The earlier experimental work from our collaborator Dr. Pilchak and Dr. Semiation was performed in Air Force Research Laboratory [67, 69]. Three high-temperature compression experiments were done to investigate the influence of loading direction on the microstructure evolution of MTRs, where the loading direction is 0°, 45° and 90° with respect to the billet axis. High temperature compression tests with three different loading directions are simulated using crystal plasticity finite element method, and the simulation results are validated against high-temperature compression experiments and EBSD measurement. In order to reveal the relationship between loading direction and MTR breakdown efficiency, the evolution of equivalent plastic strain, accumulated shear strain and misorientation distribution is analyzed in detail. Lastly, the reorientation velocity divergence within the MTR under arbitrary loading direction is presented in the Rodrigues' space to predict the optimal loading direction for breaking MTRs.

Several assumptions are adopted to isolate the effect of loading direction. First, it is assumed that α_p particles control local strain distribution at 1172 K, which is based on the experimental observation that the volume percentage of α_p particles is about 75 % at 1172 K ([69]). It is also assumed that the grain interaction and MTR breakdown efficiency can be captured by using regular shaped MTRs with pure initial orientations. This assumption is motivated by taking advantage of numerical simulation to isolate the effect of MTR orientation.

Additionally, two extensions are performed to take into account the influence from realistic microstructure and β phase. First, the strain history from selected material points in the prior simulations were imposed onto microscale models of clustered α particles with initial texture representative of orientation spread within an MTR, and sharpening or softening of texture was compared with the mesoscale results. Second, microstructure models of Ti-6242 at higher processing temperatures with greater than β phase fraction were simulated to study interaction of α particles as a function of separation and orientation.

1.1.2 Multiscale modeling

Previous experimental investigations reveal that the behavior of MTR also depends on the morphology [4] and its position within the specimen [22] under α/β processing. Again, such simulation requires the microstructure description from mesoscale and the boundary condition from macroscale, which presents great challenge to the numerical simulation. In this dissertation, a highly-efficient FE-FFT multiscale modeling framework is derived and developed to overcome this challenge.

The idea of multiscale modeling was originally proposed to enable image-based simulation of realistic structure without reasonable computational cost [54]. The multiscale modeling algorithms are classified to concurrent ones and hierarchical ones based on the coupling of both scales. A boundary value problem defined in the representative volume element (RVE) is usually solved in the microscale, and the homogenized stress is feed back to the macroscale for material update. Different numerical methods are used to solve the microscale RVE problems, including Taylor homogenization [83], grain cluster method[88], and self consistent method [74]. All these methods are based on certain homogenization

assumptions, and therefore inappropriate for exactly capturing the grain interaction required in this dissertation. FE2 method is the most popular full field multiscale modeling, which uses FE method to solve the microscale RVE problem [59]. The expensive computational cost of FE method prevents applying the FE2 method to image-based simulations

The major alternative to the FE2 method for the full-field multiscale modeling is to use FFT-based methods to solve the microscale unit cell problems. The FFT-based method was first proposed by Moulinec and Suquet [63, 64], with later improvements to increase its numerical efficiency and robustness for high-contrast problems [16, 58]. The FE-FFT multiscale modeling technique was first proposed to handle failure evolution problems in hyperelastic material [81]. Later, this framework was extended to solve phase field problems [36] and crystal plasticity problems [34]. However, this framework was based on infinitesimal strain assumption. The first finite strain FE-FFT multiscale modeling algorithm was proposed in for hyperelastic material with a consistent homogenized tangent stiffness for the basic scheme [25]. The basic scheme was used in the microscale, which is less efficient and the convergence rate depends on the reference material.

Recent development of efficient FFT-based algorithms make it possible to further accelerate the multiscale modeling method. For example, the variational frameworks can deal with high-contrast problems efficiently [5] and the Fourier-Galerkin method eliminate the dependence on reference material [91]. The latter was recently applied to solve small strain [95] and finite strain problems [8], but this method is never employed to solve crystal plasticity problems and consistent homogenized tangent stiffness is absent.

In this dissertation, a general interface is derived and implemented between the Fourier-Galerkin method and objective rate constitutive relation. One key feature of this interface is that small-strain based elasto-plastic constitutive relations, for example return mapping algorithm, can be incorporated with objectivity. Specifically, the Fourier-Galerkin method is employed to solve a Green-Naghdi rate based crystal plasticity model where most existing crystal plasticity constitutive relations can be conveniently implemented. The consistent homogenized tangent stiffness is derived to enable mixed boundary condition and concurrent multiscale modeling. Inexact Newton method is utilized to further improve the numerical efficiency of this spectral method. Lastly, the implemented spectral method is compared with

finite element method and other FFT-based methods to illustrate its numerical efficiency. The high efficiency of the current implementation makes it suitable for concurrent multiscale modeling, where extremely high computational cost is required.

Additionally, the highly efficient FE-FFT multiscale modeling framework is derived and implemented for investigating the behavior of MTRs under different loading conditions. While traditional FE-FFT multiscale modeling implementations are either based on small strain or employed to solve only hyperelastic constitutive models, here we move one step further by extending it to solve finite strain crystal plasticity constitutive relation. A total Lagrangian finite element framework is employed to solve the macroscale boundary value problem, where the material update at each integration point is performed through the spectral solver mentioned before. By accounting for finite strain in both scales, the multiscale modeling framework provides a general platform to investigate local microstructure evolution under macroscopic boundary condition. In particular, we want to do forgings, which involve large percent strain changes, like 1:2 depth reduction.

1.2 Dissertation outline

The development of the FE-FFT multiscale modeling framework and its application to the investigation of microtextured region behavior under processing conditions are described in the following chapters

- In Chapter 2, the breakdown efficiency of microtextured regions is investigated by performing crystal plasticity finite element simulations. Idealized MTRs with pure initial orientation are chosen as the benchmark case, and the simulation results are validated against high-temperature compression experiment and EBSD measurement. The evolution of dislocation density and misorientation distribution are investigated in detail to reveal the relation between loading direction and MTR breakdown efficiency. The optimal loading direction to breakdown MTRs is determined by quantifying the breakdown efficiency of arbitrary loading direction in the Rodrigues' space.

- In Chapter 3, two extensions were performed based on the results in Chapter 2. First, the strain history from selected material points in the prior simulations were imposed onto microscale models of clustered α particles with initial texture representative of orientation spread within an MTR, and sharpening or softening of texture was compared with the mesoscale results. Second, microstructure models of Ti-6242 at higher processing temperatures with greater than zero beta phase fraction were simulated to study interaction of α particles as a function of separation and orientation. In both cases, specific initial crystal orientations were found to develop large orientation gradients.

- In Chapter 4, a general interface is derived and implemented between the Fourier-Galerkin method and the objective rate constitutive model. The consistent homogenized tangent stiffness is derived to enable mixed boundary condition and concurrent multiscale modeling. Inexact Newton method is introduced to further improve the numerical efficiency. Lastly, the numerical efficiency of the Fourier-Galerkin method is compared with finite element method and other FFT-based implementation.

- In Chapter 5, a concurrent FE-FFT multiscale modeling framework is developed to further investigate the influence of MTR morphology and its position on the breakdown efficiency. The highly efficient Fourier-Galerkin implementation developed in Chapter 4 is utilized to solve the microscale RVE problem. A total Lagrangian formulation of finite element is utilized to solve the macroscopic boundary value problem. Numerical results for a single element simulation is presented to illustrate the capability and numerical efficiency of the FE-FFT multiscale modeling implementation.

- In Chapter 6, concluding remarks are presented which summarize the major contributions of this dissertation to the modeling of MTRs breakdown efficiency in Ti-6242. Additionally, possible directions for future investigation are outlined.

Chapter 2

Evolution of microtextured region in Ti-6242[1]

2.1 Introduction

The titanium alloy Ti-6242 (Ti-6Al-2Sn-4Zr-2Mo) has been the structural material of choice for use in high-pressure compressors for gas turbine engines of aircraft ([27]) due to its high strength-to-weight ratio and excellent mechanical properties. Jet engine efficiency is highly correlated to operating temperature, and Ti-6242 has demonstrated excellent creep and fatigue resistance at high temperatures up to 873 K. While the near α alloy Ti-6242 was developed for high temperature applications, its microstructural characteristics have an impact on low temperature fatigue resistance ([2]). The degraded dwell fatigue strength has been linked to the presence of microtextured regions (MTRs, also known as macrozones), which are formed during the secondary α/β hot working. This secondary α/β hot working is imposed to spheroidize the α colonies as well as to produce a microstructure of fine equiaxed α_p particles. However, the processed material may still contain large clusters ($\sim$1 mm) of primary α_p particles and secondary α_s colonies with similar c-axis orientations. For example, Figure 2.2 (c) shows a typical microstructure of the billet material after α/β processing ([67]).

---

[1]This Chapter has been adapted from "Ma, R., Pilchak, A.L., Semiatin, S.L. and Truster, T.J., 2018. Modeling the evolution of microtextured regions during α/β processing using the crystal plasticity finite element method. International Journal of Plasticity, 107, pp.189-206".

While the α_p particles are refined in size, several groups can be found of similarly oriented α_p particles in close proximity. Faceted initiation sites with sizes and shapes commensurate with those of the MTRs in the material are routinely observed on fracture surfaces formed by dwell fatigue loading. These facets typically form in so-called "hard" MTRs which have their c-axis nearly parallel to the loading direction (e.g. within 10°), and crack growth occurs over an order of magnitude faster in these orientations leading to the formation of physically large defects in a small number of cycles ([2, 68]). The size of MTRs depends significantly on prior processing steps ([67]), but are typically in the range of 0.1 mm to ∼1 mm for well processed material and several millimeters larger for poorly processed material. Therefore, it is necessary to reduce the prevalence of MTRs in order to improve the dwell fatigue behavior of Ti-6242.

Because the final microstructure is a strong function of all prior processing steps, a deep understanding of the complete thermomechanical processing sequence for $\alpha + \beta$ titanium alloys and the operative mechanisms for globularization is crucial for developing processing routes to reduce or suppress the appearance of MTRs. There have been numerous investigations that have provided a mechanism-based understanding of microtexture formation, but quantitative treatments remain limited ([89]). Early work by [93] revealed that low angle dislocation walls would develop within individual α lamellae during deformation. The β phase would penetrate these walls during subsequent static annealing in an attempt to balance interfacial energy, but this process does not induce any additional lattice rotation. Hence the resulting microstructure appears *morphologically* equiaxed and recrystallized, but electron backscatter diffraction (EBSD) analyses reveal that these grains remain similarly oriented ([21, 24, 44, 20]). [94] were the first to highlight the importance of MTRs and draw the correlation between the size of prior α colonies and the resulting MTR size after deformation. Later, [4] provided a mechanism-based understanding explaining why some colonies randomize during deformation while others persist. Recently, it was found that two α colonies from different prior β grains might have the same orientation, resulting in larger effective MTR size than prior α lamellae during the following heat treatment ([21]).

While static heat treatment cannot randomize the microstructure, strategies may be employed to solution heat treat at a temperature where the volume fraction of α is

low enough such that discrete α_p particles are separated by at least a particle distance, on average. Cooling from this temperature at moderately fast rates will produce a fine, basket-weave microstructure in the secondary alpha phase to breakup the continuity of orientation. Nevertheless, there are a number of microstructural arrangements that still intensify microtexture despite this heat treatment: (1) the persistence of Burgers orientation relationship (BOR) between α_p particles and β matrix even at severe deformation ([21, 24, 44]), (2) the variant selection of inherited α_s phase affected by existing α_p phase ([21, 44, 20]), (3) limited texture components of deformed α_p particles ([21]), and (4) dynamic recrystallization (DRX) within both primary α lamellae and β layers where new grains usually have an orientation similar to the parent grains ([44, 4]). Additional α/β processing proves to be effective in breaking down MTRs ([22]). The forging sequence of this additional processing should be chosen carefully to achieve an optimum breakdown efficiency ([4]).

Considering the extensive experimental work required to optimize the breakdown processing, numerical simulation should be included in designing forging sequences for breakdown of MTRs. However, simulating the α/β processing remains a challenge especially when prediction of microtexture is required. In addition to the plastic anisotropy and multi-scale microstructure of near α and $\alpha + \beta$ titanium alloys, modeling high temperature deformation of these alloys is further complicated by the occurrence of significant amounts of flow softening. The following studies have addressed this issue for single phase and two-phase titanium. Macroscopic phenomenological models prove to be effective in predicting the strong anisotropic plastic behavior of titanium alloys under non-proportional loading ([30, 31]). Such models also correlate well with the post-yield behavior of ultrafine-grained titanium ([46]). However, in order to investigate the microtexture evolution at high temperature and large strains, crystal plasticity based modeling is required, where strain-aging effect ([80]), recrystallization ([17]) and microstructure based modeling ([23]) can be incorporated. [45] explicitly simulated dynamic recrystallization (DRX) of TA15 alloy compressed in β regime by combining crystal plasticity finite element (CPFE) method and 3D cellular automata. [1] proposed a continuum scale physics-based model which can capture the mechanical response of Ti-6Al-4V at a large range of strain rate and temperature. [53] utilized a crystal plasticity based Mechanical Threshold Stress (MTS) model and a viscoplasticity self-consistent (VPSC)

method to simulate the mechanical response of Ti-5553 both below and above the β transus and at different loading rates. Till now, only limited investigation has been done on modeling the microtexture evolution during thermomechanical processing. For example, [60] used the viscoplastic self-consistent (VPSC) method to investigate the role of microtexture on macrotexture evolution in Ti-6Al-4V at room temperature. Thus, the relationship between MTR evolution and α/β processing sequence still remains unclear.

The current research serves as the first attempt to use the CPFE method to investigate the effect of compression direction on the efficiency of MTR breakdown. Herein, numerical analyses are carefully designed to complement the earlier experimental work from [67, 69]. The primary modeling assumption is that, the texture evolution of Ti-6242 deforming at 1172 K is mainly controlled by slip-based deformation of α_p particles. Therefore, single-phase α is considered in the current simulations. Key emphasis is placed on investigating the evolution of lattice rotation and the development of crystallographic misorientations within each MTR. To account for plastic anisotropy and unequal slip resistance, a stress update framework was developed, incorporating the Green-Naghdi stress rate along the lines of [56]. This framework is general for implementing a wide class of crystal plasticity constitutive models with multi-hardening variables by isolating the specific model dependent terms in the stress update equations. The crystal plasticity constitutive model used in [10] was extended to account for the effects of flow-softening and stress relaxation. Macroscopic stress-strain curves for Ti-6242 under compression at 1172 K and constant strain rate were used for calibrating the constitutive parameters ([69]). Subsequently, idealized microstructures were generated to capture key features from the billet textures in [67]. Typical extrusion processing leads to high-aspect-ratio MTR often having $\langle 10\bar{1}0 \rangle$ parallel to the billet extrusion axis. To gain understanding of the thermomechanical processing (TMP) parameters that reduce MTR size, [69] performed hot-compression tests at 1172 K on specimens cored from the same billet. The compression directions were 0°, 45° and 90° with respect to the extrusion axis. To approximate these tests, highly-resolved finite element models of paired MTRs embedded in a random-textured α matrix were subjected to compression in these same directions to gain a deeper understanding of the MTR breakdown process. Evolution of lattice rotation

11

and misorientation distribution within the MTRs were analyzed in detail and compared with results of rotational velocity divergence to quantify orientation stability.

The chapter is organized as follows: In Section 2.2, the numerical modeling approach is introduced in detail, including the extended crystal plasticity constitutive model, proposed stress update algorithm, material parameter calibration and CPFE microstructure description. In Section 2.3, critical results are presented, with an emphasis on the slip system activity, lattice rotation and misorientation distribution. Additional discussion is contained in Section 2.4, followed by concluding remarks in Section 2.5.

2.2 Modeling and simulation approach

The material studied is the near alpha titanium alloy Ti-6242 (Ti-6Al-2Sn-4Zr-2Mo). Flow softening is a well-known phenomenon for Ti-6242 when deformed above 973 K, which is mainly caused by: (1) Deformation induced heating with an adiabatic temperature increase, especially when forging at low temperatures and high strain rate ([78]); (2) Breakdown of coarse-grain lamellar, such as α lamellae spheroidization ([78]); (3) Slip transfer across α/β interfaces such that grain refinement strengthening and Hall-Petch effect are neutralized ([76]). To capture this softening response due to elevated temperature, a constitutive model for Ti-6242 developed in [10] was extended and implemented into the crystal plasticity finite element model of the Warp3d code ([11]). The stress update algorithm in Warp3d includes specific features; for example, the Green-Naghdi stress rate is adopted in the presence of finite rotations for the hypoelastic description of material response. These features are essential for modeling MTR evolution, which requires large deformation and lattice rotation. However, the previous CPFE implementation in Warp3d used identical hardening for all slip systems ([56, 85]), limiting the incorporation of newer CP models. In the current research, we extended this CPFE implementation to slip-system-dependent hardening and material parameters, which is required for accommodating the dissimilar slip system resistance exhibited by Ti-6242 α phase. Another feature of our implementation is that the tangent stiffness is formulated such that most existing CP models can be incorporated into this framework conveniently.

2.2.1 Crystal plasticity based constitutive law with updated lattice rotation

A brief discussion of the relevant kinematic assumptions for the implementation of crystal plasticity in the finite element program Warp3d ([11]) is given below. Further details are contained in ([56]).

The particular objective stress rate employed is the Green-Naghdi rate, $\check{\boldsymbol{\sigma}}$, expressed in terms of the spin tensor $\boldsymbol{\Omega}$ as follows:

$$\check{\boldsymbol{\sigma}} = \dot{\boldsymbol{\sigma}} + \boldsymbol{\sigma}\boldsymbol{\Omega} - \boldsymbol{\Omega}\boldsymbol{\sigma} \tag{2.1}$$

where $\boldsymbol{\sigma}$ is the Cauchy stress tensor, and the spin tensor $\boldsymbol{\Omega} = \dot{\mathbf{R}}\mathbf{R}^T$ is defined in terms of the rotation tensor $\mathbf{R}$ from the polar decomposition of the deformation gradient $\mathbf{F} = \mathbf{R}\mathbf{U}$. A primary advantage of the Green-Naghdi rate is that employing a constant elastic material moduli tensor induces minimal impact on the quality of the computed response at large rotations.

Within crystal plasticity theory, the motion of dislocations on particular crystallographic slip systems characterizes the plastic deformation, and strain compatibility is restored locally through lattice elastic deformation. The multiplicative split of the deformation gradient $\mathbf{F}$ into elastic and plastic parts expresses this deformation mode through continuum kinematics:

$$\mathbf{F} = \mathbf{F}^e\mathbf{F}^p \approx (\mathbf{I} + \boldsymbol{\varepsilon})\,\mathbf{R}^e\mathbf{R}^p\mathbf{U}^p \tag{2.2}$$

where the additional assumption of small elastic strains $\boldsymbol{\varepsilon} \ll \mathbf{I}$ is employed to simplify the resulting formulation.

The stress-strain relation obtained from (2.1) and (2.2) invokes the unrotated Cauchy stress $\mathbf{t}$ and its work conjugate deformation rate $\mathbf{d}$ in the intermediate configuration as:

$$\dot{\mathbf{t}} = \mathbf{C}_0 : \left(\mathbf{d} - \bar{\mathbf{d}}^p\right) + \mathbf{R}\bar{\mathbf{w}}^p\mathbf{R}^T\mathbf{t} - \mathbf{t}\mathbf{R}\bar{\mathbf{w}}^p\mathbf{R}^T \tag{2.3}$$

in which $\mathbf{t} = \mathbf{R}^T \boldsymbol{\sigma} \mathbf{R}$ is the unrotated Cauchy stress and $\mathbf{d} = \frac{1}{2}\left(\dot{\mathbf{U}}\mathbf{U}^{-1} + \mathbf{U}^{-1}\dot{\mathbf{U}}\right)$ is the unrotated rate of deformation. The plastic deformation rate $\bar{\mathbf{d}}^p$ and plastic vorticity $\bar{\mathbf{w}}^p$ are defined subsequently through constitutive relations in terms of the corotational plastic velocity gradient $\bar{\mathbf{l}}^p$. In the numerical implementation, the backward Euler time integration scheme is applied to evolve equation (2.3), and the nodal displacements and applied incremental strains are directly employed to compute $\mathbf{F}$ and $\mathbf{d}$ at the element level. Further details of the derivation and implementation are provided in [56]. In particular, the additional stress and rotation terms in (2.3) are correction terms accounting for the effect of plastic spin.

For single crystal plasticity, the plastic strain rate is commonly represented through slip rates $\dot{\gamma}^{(s)}$ resolved onto the primary slip systems $s = 1, \ldots, n_{slip}$:

$$\tilde{\mathbf{l}}^p = \sum_{s=1}^{n_{slip}} \dot{\gamma}^{(s)} \left(\tilde{\mathbf{b}}^{(s)} \otimes \tilde{\mathbf{n}}^{(s)}\right) \tag{2.4}$$

$$\bar{\mathbf{d}}^p = \sum_{s=1}^{n_{slip}} \dot{\gamma}^{(s)} \mathbf{R}^{pT} \tilde{\mathbf{m}}^{(s)} \mathbf{R}^p \tag{2.5}$$

$$\bar{\mathbf{w}}^p = \sum_{s=1}^{n_{slip}} \dot{\gamma}^{(s)} \mathbf{R}^{pT} \tilde{\mathbf{q}}^{(s)} \mathbf{R}^p \tag{2.6}$$

$$\tilde{\mathbf{m}}^{(s)} = \mathrm{sym}\left(\tilde{\mathbf{b}}^{(s)} \otimes \tilde{\mathbf{n}}^{(s)}\right) \tag{2.7}$$

$$\tilde{\mathbf{q}}^{(s)} = \mathrm{skew}\left(\tilde{\mathbf{b}}^{(s)} \otimes \tilde{\mathbf{n}}^{(s)}\right) \tag{2.8}$$

where $\tilde{\mathbf{b}}^{(s)}$ is the slip direction within a crystal plane s and $\tilde{\mathbf{n}}^{(s)}$ is the unit normal to plane s. The "tilde" overbar refers to quantities in the lattice frame while the flat overbar denotes quantities in the current deformed frame. Additionally, the evolution of the plastic rotation rate is expressed through the plastic vorticity as $\dot{\mathbf{R}}^p = \bar{\mathbf{w}}^p \mathbf{R}^p$.

The extended grain-scale crystal plasticity model for the Ti-6242 near alpha titanium alloy accounting for flow softening follows from the bimodal titanium model proposed in [10]. For the current developments, only microstructures containing primary α_p particles are considered. This constitutive model incorporates a decreasing slip resistance due to plastic

deformation. The slip rate $\dot{\gamma}^{(s)}$ on each slip system s is taken as a power law expression involving the resolved shear stress $\tau^{(s)}$ and the slip resistance $\xi^{(s)}$:

$$\dot{\gamma}^{(s)} = \dot{\gamma}_0^{(s)} \left| \frac{\tau^{(s)}}{\xi^{(s)}} \right|^{1/m} \text{sign}\left(\tau^{(s)}\right) \tag{2.9}$$

Here $\dot{\gamma}_0^{(s)}$ is the reference strain rate, m is a constant exponent and $\xi^{(s)}$ is the slip resistance of slip system s. The slip resistance evolution is expressed through a combination of self-hardening and latent hardening:

$$\dot{\xi}^{(i)} = \sum_{j=1}^{n_{slip}} h^{(ij)} \left| \dot{\gamma}^{(j)} \right| = \sum_{j=1}^{n_{slip}} q^{(ij)} h^{(j)} \left| \dot{\gamma}^{(j)} \right| \tag{2.10}$$

Here $h^{(ij)}$ is the combination of self-hardening rate $h^{(j)}$ and latent hardening rate $q^{(ij)}$. The value of $q^{(ij)}$ is set to 1 for all i and j, such that full latent-hardening is considered. The self-hardening rate follows a Voce-type equation:

$$h^{(j)} = h_0^{(j)} \left| 1 - \frac{\xi^{(j)}}{\xi_s^{(j)}} \right|^r \text{sign}\left(1 - \frac{\xi^{(j)}}{\xi_s^{(j)}} \right), \ \xi_s^{(j)} = \tilde{\xi}^{(j)} \left(\frac{\dot{\gamma}^{(j)}}{\dot{\gamma}_0} \right)^n . \tag{2.11}$$

Here $h_0^{(j)}$ is the initial hardening rate, and the saturation resistance $\xi_s^{(j)}$ is taken as a power-law relation of the current slip rate with exponent n and pre-factor $\tilde{\xi}^{(j)}$. Section 2.2.3 describes the slip system families employed for the α_p phase and its relative constitutive parameters. Note that this model does not have contributions from geometrically necessary dislocation or strain gradient terms and hence is not size dependent.

The CP constitutive model (2.9)–(2.11) was originally developed to describe the rate-sensitive strain hardening relation between shear strain rate $\dot{\gamma}^{(s)}$ and resolved shear stress $\tau^{(s)}$, and was applied to model Ti-6242 in [10]. We extended this model to describe also the strain softening behavior by simply setting the initial hardening variable ξ_0 to be larger than the saturated resistance $\xi_s = \xi_s\left(\dot{\gamma}_0, \tilde{\xi}\right)$, such that the hardening rate $h^{(j)}$ becomes negative according to equation (2.11).

Remark: *For initial elastic loading or the case when certain slip systems are not activated during the deformation, the slip rate $\dot{\gamma}^{(i)}$ and consequently $\xi_s^{(i)}$ on certain slip systems remain*

close to zero, which causes numerical issues in (2.11). To avoid this deficiency, the lower bound of $\xi_s^{(i)}$ was set to be $\tilde{\xi}^{(i)}/4$, which is smaller than the actual saturation stress of an activated system.

2.2.2 Generalized implicit material update algorithm

In order to account for slip system dependence of the flow resistance, the Green-Naghdi stress rate based material update algorithm was modified from the work of [56], where only one hardening variable is allowed. This algorithm was modularized to accommodate any crystal plasticity model with multi-hardening variables, where only 6 terms are model dependent, i.e. two residual terms and four tangent stiffness terms.

In the finite element setting, the material evolution equations (2.3) and (2.10) are tracked at the integration points of elements within the mesh during a series of time steps. Therefore, the objective of the material update routine is to advance the values of the stress and hardening variables to time $t_{n+1} = t_n + \Delta t$. Both equations (2.3) and (2.10) will be integrated using a backward Euler scheme, and together represent an implicit system of equations to be solved. The equations are:

$$0 = \mathbf{R}_1 = \mathbf{t}_{n+1} - \left[\mathbf{t}_n + \dot{\mathbf{t}} \left(\mathbf{t}_{n+1}, \boldsymbol{\xi}_{n+1}, \Delta\mathbf{d}_{n+1} \right) \Delta t \right] \tag{2.12}$$

$$0 = \mathbf{R}_2 = \boldsymbol{\xi}_{n+1} - \left[\boldsymbol{\xi}_n + \dot{\boldsymbol{\xi}} \left(\mathbf{t}_{n+1}, \boldsymbol{\xi}_{n+1}, \Delta\mathbf{d}_{n+1} \right) \Delta t \right] \tag{2.13}$$

where the incremental deformation rate $\Delta\mathbf{d}_{n+1} = \mathbf{d}_{n+1}\Delta t$ is specified from the current best estimate of the nodal displacement increment, and $\boldsymbol{\xi}$ is the set of hardening variables (presently, the slip resistances $\xi_s^{(s)}$, $i = 1, \ldots, n_{slip}$).

The quantities within the objective stress update (2.12) and hardening variable update (2.13) are defined with respect to the time discrete counterparts:

$$\dot{\mathbf{t}}_{n+1}\Delta t = \mathbf{C}_0 : \left(\Delta\mathbf{d}_{n+1} - \Delta\bar{\mathbf{d}}_{n+1}^p \right) + \Delta\bar{\mathbf{W}}_{n+1}^p\mathbf{t}_{n+1} - \mathbf{t}_{n+1}\Delta\bar{\mathbf{W}}_{n+1}^p \tag{2.14}$$

Table 2.1: Newton-Raphson algorithm for stress update

procedure	equation
1. Check	compare $\|\mathbf{R}\|$ and R_{tol}
2. Solve	$\begin{bmatrix} \mathbf{J}_{11} & \mathbf{J}_{12} \\ \mathbf{J}_{21} & \mathbf{J}_{22} \end{bmatrix} \begin{bmatrix} \delta\mathbf{t} \\ \delta\boldsymbol{\xi} \end{bmatrix} = - \begin{bmatrix} \mathbf{R}_1 \\ \mathbf{R}_2 \end{bmatrix}$
3. Update	$\begin{bmatrix} \mathbf{t}_{n+1}^{i+1} \\ \boldsymbol{\xi}_{n+1}^{i+1} \end{bmatrix} = \begin{bmatrix} \mathbf{t}_{n+1}^{i} \\ \boldsymbol{\xi}_{n+1}^{i} \end{bmatrix} + \begin{bmatrix} \delta\mathbf{t} \\ \delta\boldsymbol{\xi} \end{bmatrix}$
4. Form	$\begin{bmatrix} \mathbf{R}_1 \\ \mathbf{R}_2 \end{bmatrix} = \begin{bmatrix} \mathbf{R}_1\left(\mathbf{t}_{n+1}^{i}, \boldsymbol{\xi}_{n+1}^{i}\right) \\ \mathbf{R}_2\left(\mathbf{t}_{n+1}^{i}, \boldsymbol{\xi}_{n+1}^{i}\right) \end{bmatrix}, \ \mathbf{J}_{jk} = \mathbf{J}_{jk}\left(\mathbf{t}_{n+1}^{i}, \boldsymbol{\xi}_{n+1}^{i}\right)$

$$\Delta\bar{\mathbf{d}}_{n+1}^{p} = \sum_{s=1}^{n_{slip}} \Delta\gamma_{n+1}^{(s)} \mathbf{R}_n^{pT} \tilde{\mathbf{m}}^{(s)} \mathbf{R}_n^{p} \tag{2.15}$$

$$\Delta\bar{\mathbf{W}}_{n+1}^{p} = \mathbf{R}_{n+1} \left[\sum_{s=1}^{n_{slip}} \Delta\gamma_{n+1}^{(s)} \mathbf{R}_n^{pT} \tilde{\mathbf{q}}^{(s)} \mathbf{R}_n^{p} \right] \mathbf{R}_{n+1}^{T} \tag{2.16}$$

$$\Delta\gamma_{n+1}^{(s)} = \dot{\gamma}^{(s)} \left(\tau_{n+1}^{(s)}, \xi_{n+1}, \frac{\Delta\mathbf{d}_{n+1}}{\Delta t} \right) \Delta t \tag{2.17}$$

$$\tau_{n+1}^{(s)} = \mathbf{t}_{n+1} : \left(\mathbf{R}_n^{pT} \tilde{\mathbf{m}}^{(s)} \mathbf{R}_n^{p} \right) \tag{2.18}$$

$$\mathbf{R}_{n+1}^{p} = \exp\left(\Delta\bar{\mathbf{w}}_{n+1}^{p} \right) \mathbf{R}_n^{p} \tag{2.19}$$

$$\dot{\xi}_{n+1}^{(i)} = \dot{\xi}_n^{(i)} + \sum_{j=1}^{n_{slip}} h_{n+1}^{(ij)} \left| \dot{\gamma}_{n+1}^{(j)} \right| \Delta t. \tag{2.20}$$

Notice that the plastic rotation tensor $\mathbf{R}^p$ is treated in an explicit fashion since the value from time t_n is used in equations (2.15)–(2.18). This algorithmic assumption greatly simplifies the nonlinear system of equations (2.12)–(2.13) and generally is appropriate because the evolution of plastic rotation $\mathbf{R}^p$ is relatively slow compared to the plastic strain rate $\bar{\mathbf{d}}^p$ ([56]). Equation (2.20) specializes the hardening variable update for the material model described in equation (2.9)–(2.11).

The residual equations (2.12)–(2.13) are solved using a Newton-Raphson scheme with appropriate initial guesses for the stress $\mathbf{t}_{n+1}$ and hardening $\boldsymbol{\xi}_{n+1}$. A generic iteration of this algorithm is summarized in Table 2.1, where the superscript i denotes the value at the indicated iteration.

At each iteration, the norms of the residuals $\|\mathbf{R}_1\|$, $\|\mathbf{R}_2\|$ are computed, and the algorithm is terminated when either the absolute norm or the relative norm of both residuals is below a user-specified tolerance R_{tol}. The Jacobian sub-matrices are obtained from the consistent

linearization of (2.12)–(2.13), with $\mathbf{J}_{ij} = \partial \mathbf{R}_i / \partial \mathbf{x}_j$ and $\mathbf{x}_{j=1,2} = \{\mathbf{t}, \boldsymbol{\xi}\}$. Accounting for the specific forms assumed for the plastic slip rates (2.9) and the hardening variables (2.10), these derivatives can be expressed as follows, using index notation for clarity:

$$
J_{11,ijkl} = \frac{\partial R_{1,ij}}{\partial t_{kl}} = \frac{1}{2}\left(\delta_{ik}\delta_{jl} + \delta_{il}\delta_{jk}\right) + \frac{1}{2}\left(\delta_{ik}\Delta\bar{W}^p_{lj} + \delta_{il}\Delta\bar{W}^p_{kj}\right) - \frac{1}{2}\left(\Delta\bar{W}^p_{ik}\delta_{jl} + \Delta\bar{W}^p_{il}\delta_{jk}\right)
$$
$$
+ \sum_{s=1}^{n_{slip}}\left[\left(C_{0,ijmn}\frac{\partial\Delta\bar{d}^p_{mn}}{\partial\Delta\gamma^{(s)}_{n+1}} + t_{im}\frac{\partial\Delta\bar{W}^p_{mj}}{\partial\Delta\gamma^{(s)}_{n+1}} - \frac{\partial\Delta\bar{W}^p_{im}}{\partial\Delta\gamma^{(s)}_{n+1}}t_{mj}\right)\underbrace{\frac{\partial\Delta\gamma^{(s)}_{n+1}}{\partial\tau^{(s)}}}_{\text{model}}\frac{\partial\tau^{(s)}}{\partial t_{kl}}\right]
$$

$$(2.21)$$

$$
J_{12,ij\beta} = \frac{\partial R_{1,ij}}{\partial\xi_\beta} = \sum_{s=1}^{n_{slip}}\left[-C_{0,ijmn}\frac{\partial\Delta\bar{d}^p_{mn}}{\partial\Delta\gamma^{(s)}_{n+1}} + t_{im}\frac{\partial\Delta\bar{W}^p_{mj}}{\partial\Delta\gamma^{(s)}_{n+1}} - \frac{\partial\Delta\bar{W}^p_{im}}{\partial\Delta\gamma^{(s)}_{n+1}}t_{mj}\right]\underbrace{\frac{\partial\Delta\gamma^{(s)}_{n+1}}{\partial\xi_\beta}}_{\text{model}} \qquad (2.22)
$$

$$
J_{21,ij\alpha} = \frac{\partial R_{2,\alpha}}{\partial t_{kl}} = -\Delta t\underbrace{\frac{\partial\dot{\xi}_\alpha}{\partial t_{kl}}}_{\text{model}} \qquad (2.23)
$$

$$
J_{22,\alpha\beta} = \frac{\partial R_{2,\alpha}}{\partial\xi_\beta} = \delta_{\alpha\beta} - \Delta t\underbrace{\frac{\partial\dot{\xi}_\alpha}{\partial\xi_\beta}}_{\text{model}} \qquad (2.24)
$$

Each of the Latin alphabet subscripts varies from 1 to 3 for the spatial dimensions of the problem, although accounting for the symmetry of the stress tensor enables condensing from $3 \times 3 = 9$ indices to 6 indices. Each of the Greek alphabet subscripts varies from 1 to the number of hardening variables n_{hard}. When the Newton-Raphson algorithm (Table 2.1) has been terminated after sufficient reduction of the residuals, the consistent values for $\mathbf{t}$ and $\boldsymbol{\xi}$ have been found for the current value of the strain increment $\Delta\mathbf{d}_{n+1}$ at the integration point. The unrotated stress $\mathbf{t}$ is then transformed to the Cauchy stress $\boldsymbol{\sigma}$ and used by the element subroutine to compute the internal force vector for assembly in the global equilibrium residual vector. Similarly, the tangent moduli $\mathbf{T}_{n+1} = \partial\mathbf{t}_{n+1}/\partial\Delta\mathbf{d}_{n+1}$ for the global equilibrium tangent matrix are computed from (2.21)–(2.24) along with other terms described in [56].

18

Table 2.2: Elasticity constants of Ti-6242 in the material coordinates (1172 K)

C_{11}(GPa)	C_{33}(GPa)	C_{12}(GPa)	C_{13}(GPa)	C_{44}(GPa)	C_{66}(GPa)
132.8	159.4	76.56	67.19	39.84	28.12

The significance of this generalized stress update algorithm is that the model dependent terms are clearly isolated from the crystal plasticity kinematics as two scalar constitutive terms $\dot{\gamma}^{(s)}$ and $\dot{\xi}_\alpha$, and four tangent terms as shown in (2.21)–(2.24). Thus, other constitutive models, e.g. mechanical threshold models ([37]) and dislocation density based models ([48]), can be conveniently implemented in this framework.

2.2.3 Parameter identification

Anisotropic elastic constants of single crystal Ti-6242 are listed in Table 2.2. The relative ratio between elastic constants was fixed according to the values at room temperature reported in [10], and the magnitude was adjusted according to the temperature-dependence of the Young's modulus experimentally measured in [69]. Transverse isotropy was adopted for the hexagonal close-packed α_p phase, and the c-axis coincides with the z direction. Elastic constants measured at 1172 K are about 20 % smaller than those at room temperature.

The material parameters from [10] were recalibrated to match the softening observed at 1172 K ([69]). The calibration was performed through a series of finite element simulations that employed a single finite element with 100 random orientations of crystals homogenized through the Taylor assumption. Constant true strain rate simulations were performed at $\dot{\varepsilon} = 0.01 \text{ s}^{-1}$, which is consistent with the experiment ([69]). The material parameters $\tilde{\xi}^{(j)}$, $h_0^{(j)}$ and $\xi_0^{(j)}$ were varied until the difference between experiment and simulation was minimized. Three slip system families were considered: basal $\langle 11\bar{2}0 \rangle \{0001\}$, prismatic $\langle 11\bar{2}0 \rangle \{10\bar{1}0\}$, and 1st order pyramidal$- \langle c+a \rangle \langle 11\bar{2}3 \rangle \{10\bar{1}1\}$. The ratio of slip system strengths was held fixed at 1.0:0.67:3.0 according to the critical resolved shear stress measured at 1088-1228 K from [77]. The importance of the unequal slip resistances for the three systems versus a uniform resistance for properly capturing Ti-6242 MTR breakdown is demonstrated by a reference simulation in Section 2.3.2.

Table 2.3: Crystal plasticity parameters for Ti-6242 α_p particles at 1172 K

	Basal	Prismatic	Pyramidal
$\dot{\gamma}_0$ (s^{-1})	0.12	0.12	0.12
$\tilde{\xi}$ (MPa)	69.38	46.25	208.13
h_0 (MPa)	4.69	9.72	28.22
ξ_0 (MPa)	68.08	54.46	163.4
n	0.14	0.15	0.15
r	0.30	0.29	0.29
m	0.20	0.20	0.20

The calibrated material parameters are listed in Table 2.3. Figure 2.1 compares the measured true stress-strain curve from constant strain rate (~ 0.01 s^{-1}) tests under three compression directions with the results from the displacement-controlled finite element simulation. The measured and simulated responses match well, and the softening behavior of stress-strain relation is well captured. Note that softening response is achieved when the initial resistance ξ_0 exceeds the saturated resistance $\xi_s = \xi_s \left(\dot{\gamma}_0, \tilde{\xi} \right)$, which for example takes a value of about 49 MPa for the basal systems at the applied 0.01 s^{-1} strain rate. Here, ξ_0 is the initial value of the hardening variable ξ, where the latter evolves under continued deformation. Due to the random texture assumption, the simulated stress-strain curve is less loading-axis dependent than the experimental curves, which are obtained from cylinders extracted at various angles relative to the long axis of a textured billet ([69]). The initial yield stress is about 120 MPa, and gradually converges to 80 MPa as the applied strain increases to -0.8. The plastic anisotropy caused by initial texture is apparent, especially at the onset of plastic yielding where flow stress in axial direction is 10 MPa larger than that in radial direction and 45° direction. It should be noted that the material parameters in Table 2.3 were calibrated only for the hot-compression tests conducted at 1172 K with constant true strain rate of $\dot{\varepsilon} = 0.01$ s^{-1}. These material parameters are sufficient to correlate the simulation and EBSD measurements in Section 2.3 to interpret the effect of loading axis on breakdown efficiency. However, to also include the effects of temperature and strain rate, this model (or another temperature sensitive model) would likely need to be recalibrated based on stress-strain curves obtained from the billet material at multiple temperatures and strain rates.
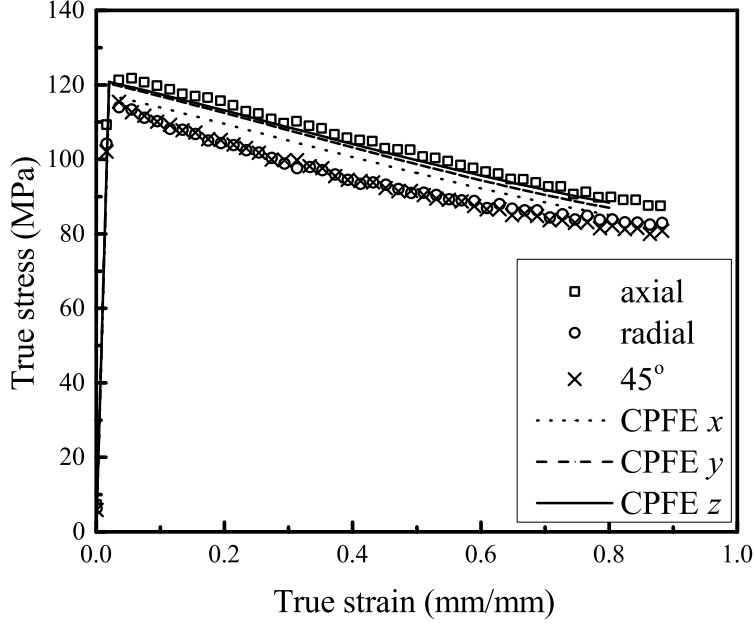
Figure 2.1: True stress-strain response from Taylor simulation (random texture) and cylinder compression experiments (1172 K) ([69])

2.2.4 Simulation microstructure description

The initial microstructure and texture for the CPFE simulations were designed to capture the main features of the experimental methods in [69]. Therein, the billet material is a commercially produced near-α alloy Ti-6Al-2Sn-4Zr-2Mo-0.1Si (Ti6242S). Experiment characterizations suggest that this 209-mm-diameter billet was obtained from preliminary extrusion, resulting in a microstructure of equiaxed 10 μm diameter α_p particles. Typically, such extrusion leads to a fiber texture with $\langle 10\bar{1}0 \rangle$ parallel to the axial direction, while the c-axis equally distributes along the radial direction ([67]). The actual macrotexture pole figures of the 209-mm-diameter billet material are reproduced in Figure 2.2 (a). Overall, the macrotexture is relatively weak ($\sim$ 2.5$\times$random), and $\langle 10\bar{1}0 \rangle$ parallel to the axial direction is one major texture component. Because of the low strain from preliminary processing, the texture components are not strong, and low density peaks scatter throughout the (0001) pole figure. α/β processing by cogging and/or extrusion to produce billet or bar stock generally leads to the formation of a $\langle 10\bar{1}0 \rangle$ texture at large strains, but the extrusion strain of the current sample was only sufficient to rotate some grains to this orientation. As the extrusion strain increases, such as the case of the 57-mm-diameter billet material shown in

21

Figure 2.2 (b), the exhibited texture components are stronger and closer to the theoretical components. However, strong MTRs with moderate aspect ratio ($\sim 4:1$) do exist in the 209-mm-diameter billet material, as shown by the inverse pole figure of Figure 2.2 (c). The mean diameter of MTR is about 800 μm, and the volume fraction of MTR is about 0.6 ([67]). Pairs of neighboring MTRs with orthogonal c-axis are still present. Previously, successive extrusion processing was found to be less effective at eliminating such pairs of MTRs with stable orientation ($\langle 10\bar{1}0 \rangle$ parallel to the axial direction).

In order to optimize the TMP parameters for eliminating such stable MTRs, samples taken from the billet material were compressed isothermally at 1172 K with different compression directions ([69]). Specifically, the compression direction is 0° (axial compression), 45° and 90° (radial compression) to the billet axis. In order to obtain the morphology of α_p particles and β matrix at elevated temperature, samples were water quenched after compression up to 1.07 true strain. More details about the experiment are given in [69].

Herein, a 5 mm $\times$ 5 mm $\times$ 5 mm idealized volume element (IVE) containing two MTRs was employed to investigate the breakdown of MTRs under different compression directions, as shown in Figure 2.3. Also, the present CPFE model assumes that texture evolution of Ti-6242 deformed at 1172 K is mainly controlled by slip-based deformation of α_p particles. The green and red regions are sufficiently large that they represent collections of similarly oriented α_p particles, or two MTRs, while the blue region is a homogeneous matrix with random orientation. These two MTRs have an elongated capsule shape, such that the length and diameter of the geometry is comparable to the experimental observations. The adjacent MTRs also makes it straightforward to see the interaction between two MTRs. The total volume of the MTRs in the simulation domain is about 5 %. Actually, at 1172 K, the microstructure of Ti-6242 from typical processing contains equiaxed α_p particles with similar orientation (75 %) with the remaining balanced by β phase (25 %) ([69]). Herein, idealized MTRs with simplified shape and uniform initial orientation were chosen as a benchmark case. The hexahedral mesh is a uniform grid with 100 voxels along each domain edge, and the MTR-matrix interfaces are non-smooth. The size of each element is 50 μm, which is equivalent to a few α_p particle diameters. The mesh resolution in the MTRs is significantly refined in order to capture the lattice rotation gradients within and between both MTRs.

22
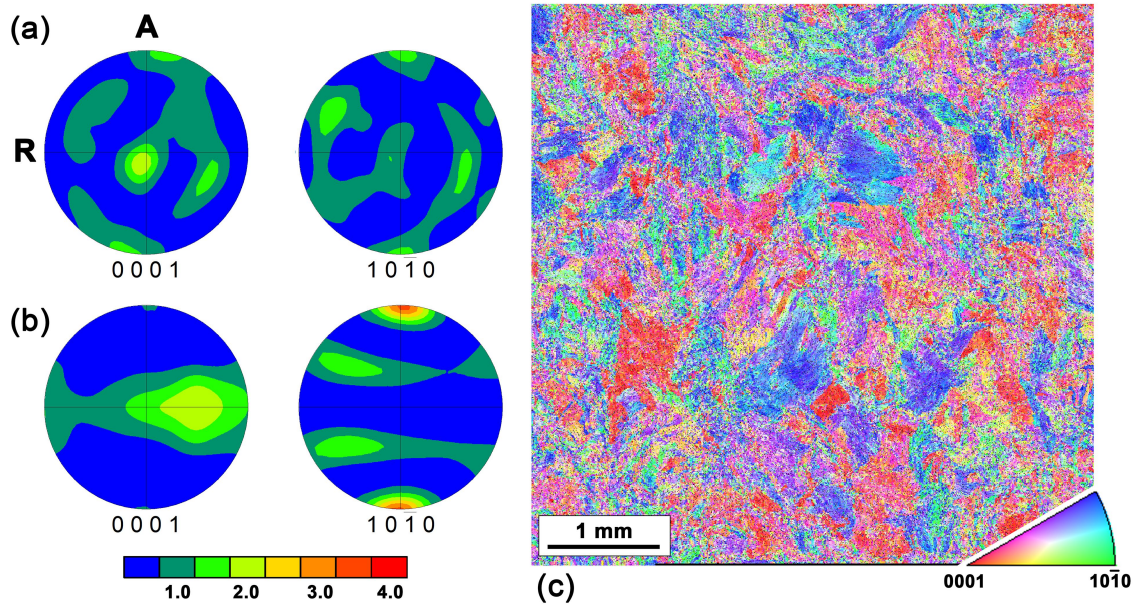
Figure 2.2: Representative EBSD measurement of the macrotexture and microtexture distribution within the billet material: Macrotexture pole figures ((0001) and (10$\bar{1}$0)) of (a) the 209-mm-diameter billet and (b) the 57-mm-diameter billet at mid-radius location ([67]). (c) Axial direction crystal-orientation maps for 209-mm-diameter billet at mid-radius location, where the billet axis is perpendicular to the plane. A spatial cluster of similar or identical color indicates alpha particles forming a microtextured region (MTR).
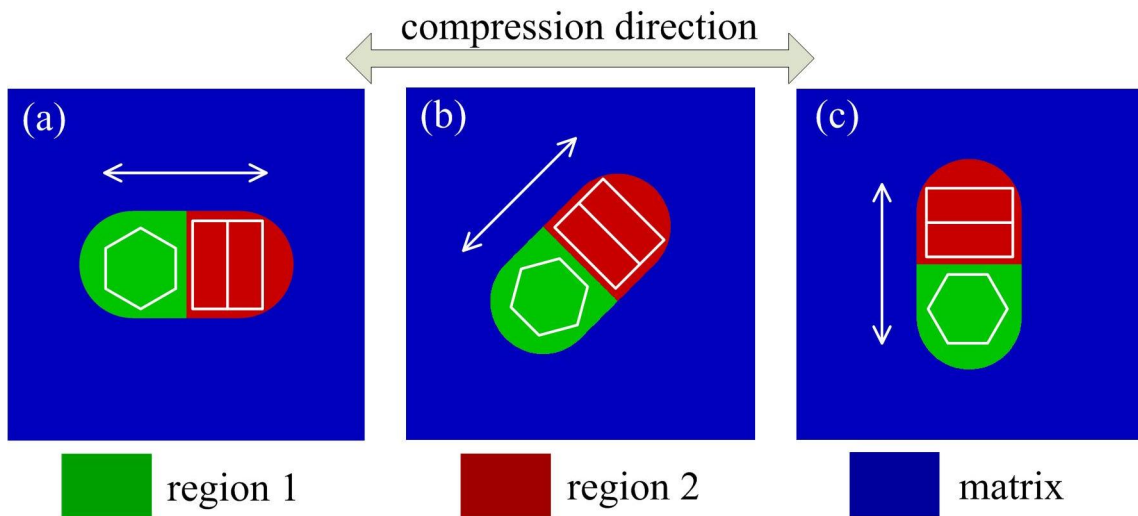
Figure 2.3: Initial configuration of the MTR (slice of 3D geometry) used in the present study for three loading cases. White arrows indicate billet axis, hexagons depict the MTR lattice orientation, and the black arrow indicates compression direction. (a) compression 0° to billet axis; (b) compression 45° to billet axis; (c) compression 90° to billet axis.

Compression was applied to the IVE along three different directions to investigate the corresponding MTR breakdown efficiency, as shown in Figure 2.3. The orientations of the two MTRs are selected from the theoretical extrusion macrotexture to approximate the billet textures in Figure 2.2, where the $\langle 10\bar{1}0\rangle$ direction is parallel to the billet axis and the c-axis is along the radial direction. Thus, these two idealized regions act as samples of MTR from within the macrotexture of the three compression cylinders described previously. This orientation of MTR is different from those after rolling as described in [3, 13], where the c-axis coincides with RD and TD while the common crystal direction $\langle 11\bar{2}0\rangle$ coincides with ND. In the RVE, each finite element in the matrix was assigned a different orientation from a random initial texture. Notice that the MTRs are compressed in series for Figure 2.3 (a) and in parallel for Figure 2.3 (c). Also notice for the radial case Figure 2.3 (c) that region 1 is oriented with the c-axis perpendicular to load axis (soft orientation) while region 2 has its c-axis parallel to load axis (hard orientation).

Prescribed displacements were applied on the loading surface such that the true strain rate was 0.01 s^{-1}. Multi-point constraints (MPC) were applied on the transverse surfaces to approximate a uniaxial state of remote stress on the IVE. The IVE simulations were performed using Warp3d ([11]) in a high performance parallel computing environment. Approximate wall clock time for each IVE simulation is about 30 hours when 18 shared memory threads are used. The resulting plastic strain, slip system activity and lattice rotation were compared to understand the breakdown of the two MTRs. The deformed Euler angles from the models were imported into MTEX ([52]) to calculate the corresponding orientation distribution functions (ODF) and subsequently generate pole figures and inverse pole figures.

2.3 Results

2.3.1 Equivalent plastic strain distribution within MTRs

MTR breakdown efficiency is often influenced by inhomogeneous plastic strain. Figure 2.4 shows the equivalent plastic strain distribution within MTRs plotted on the deformed

configuration after compression at 1172 K up to -0.51 true strain. Figure 2.5 presents the equivalent plastic strain distribution along the central line inside each MTR at -0.51 macroscopic strain. The arc length measures the length along the selected path within the MTRs from one end to the other, with 0.0-1.5 mm representing region 1 and 1.5-3.0 mm representing region 2 for all three figures. These results reveal that plastic strain is more inhomogeneous for the $0°$ (axial) compression case compared with the other two compression directions. For $0°$ (axial) compression, the circular cross-section evolves into an elliptical shape. The long axis of the ellipse is perpendicular to the crystal plane $(11\bar{2}0)$ for both regions. Due to strain accommodation of the two regions, the plastic strain along the interface between the two regions is lower than that in the region interiors, and the transition is rather smooth. Moreover, strong fluctuations appear in the equivalent plastic strain distribution within both regions, indicating a possibility of high breakdown efficiency. For $45°$ compression, the MTRs exhibit relatively unchanged shape and rotate as a unit toward the radial direction of the sample after deformation. Both maximum and minimum local strain exists at the interface between the two regions, while the local strain within each region is relatively homogeneous. For $90°$ (radial) compression, equivalent plastic strain in region 1 is as high as 0.6, while in region 2 the average value is generally lower than 0.3. Strain transition from region 1 to region 2 is rather smooth.

Previous studies found that the choice of element type may influence the quality of CPFE simulation results, especially at MTR boundaries where stress concentrations exist ([6]). To quantitatively understand this influence, meshes with linear hexahedral elements and meshes with quadratic tetrahedral elements were generated for all three compression directions, and the resulting plastic strain distributions were compared. For brevity, the results are not shown here. The major conclusion is that the deformed shape of the MTRs as well as the plastic strain distribution away from the boundaries ($1 \sim 2$ element diameters) are in close agreement for both mesh types, indicating that the interior response has not been affected.

2.3.2 Slip system activity

The development of orientation distribution within each MTR indicates that different lattice rotations have occurred over the MTR region. Differences in lattice rotation result from
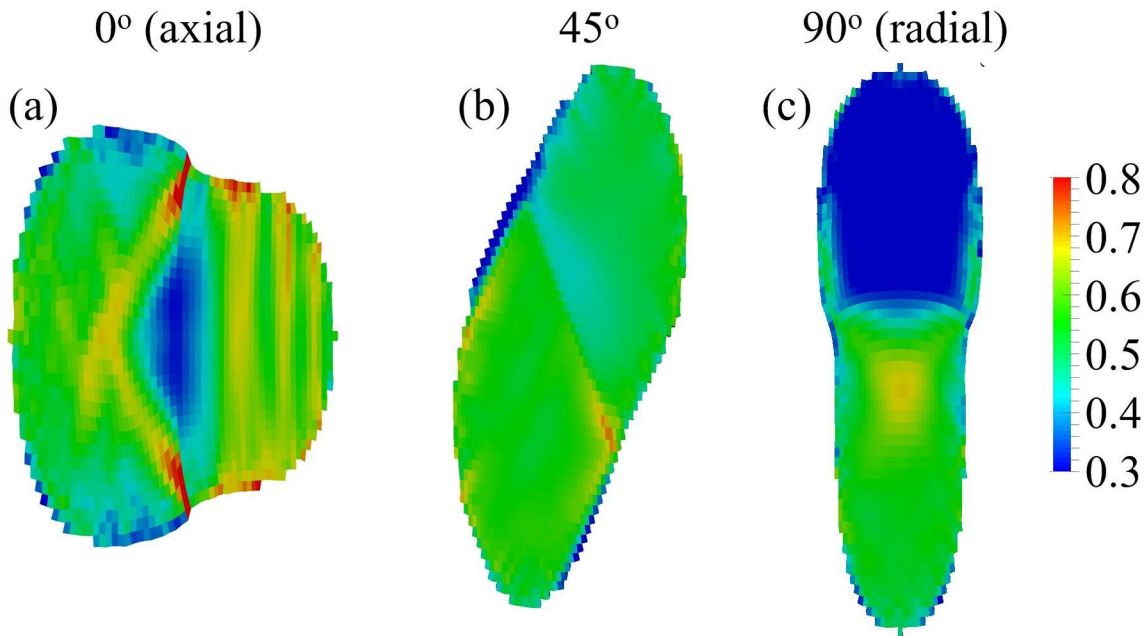
Figure 2.4: Equivalent plastic strain distribution within MTRs on deformed configuration after compression at 1172 K to -0.51 true strain (cross-section view on the mid plane).
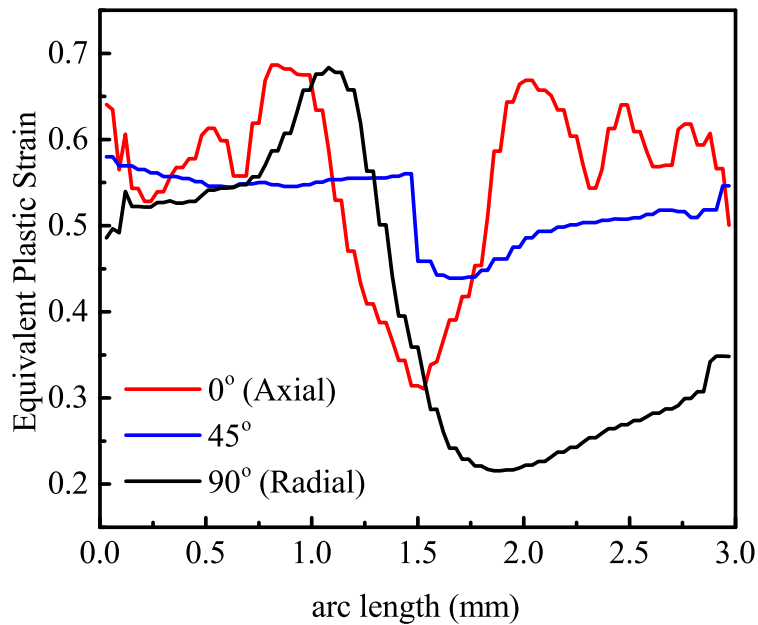
Figure 2.5: Equivalent plastic strain distribution along center line of MTR. (a) 0° (axial) compression; (b) 45° compression; (c) 90° (radial) compression.

differences in slip system activity. This section compares the accumulated shear strain, defined by $\int_0^t |\dot{\gamma}^{(s)}| \mathrm{d}t$, for the three most activated slip systems under different loading directions. Figure 2.6 demonstrates the predicted activities of slip systems along the central line from these two MTRs with different initial orientations at macroscopic true strain -0.51. Contribution from the pyramidal slip systems is fairly low in each case.

For $0°$ (axial) compression, the compression direction is along $[10\bar{1}0]$ of both regions, such that two prismatic slip systems are most activated. It is interesting to find that in some places, the prismatic system $[\bar{1}2\bar{1}0]$ is more activated while in other places the prismatic system $[\bar{2}110]$ becomes more activated. Such competitive activity in both regions will result in increasing misorientation within both MTRs. The slip system activity at the MTR boundary is much lower than in the interior, mainly because the high $75.5°$ angle between the slip planes on both sides makes the transfer of shear strain more difficult across the regions. Further interpretations about the competitive slip system activity are discussed in Section 2.4.

When the compression direction is aligned at $45°$ to the billet axis, a single prismatic slip system dominates in region 1 while two basal slip systems are equally activated in region 2. The distribution of accumulated shear strain of each slip system is rather smooth compared with $0°$ (axial) compression, even when two basal slip systems are equally activated in region 2. In both regions, other slip systems are also activated, but the accumulated shear strain is generally less than 30 % of the most activated slip system.

For $90°$ (radial) compression, the slip system activity is quite different. In region 1, two prismatic slip systems are equally activated across the MTR domain. Minimum shear strain also exists at the region boundary where dislocation transfer across the boundary is restricted. For region 2, since the compression direction is perpendicular to the basal plane, only pyramidal slip systems are activated, and the accumulated shear strain is less than 0.1.

The variety of results for the accumulated plastic strain and slip system activity depend crucially upon the differing slip system resistances assigned in Table 2.3. Ti-6242 is known to exhibit anisotropic response at high temperatures ([77]). As a comparison, the $0°$ (axial) compression case was simulated again using the averaged initial and saturation parameters from Table 2.3 assigned to all of the basal, prismatic and pyramidal slip systems. The
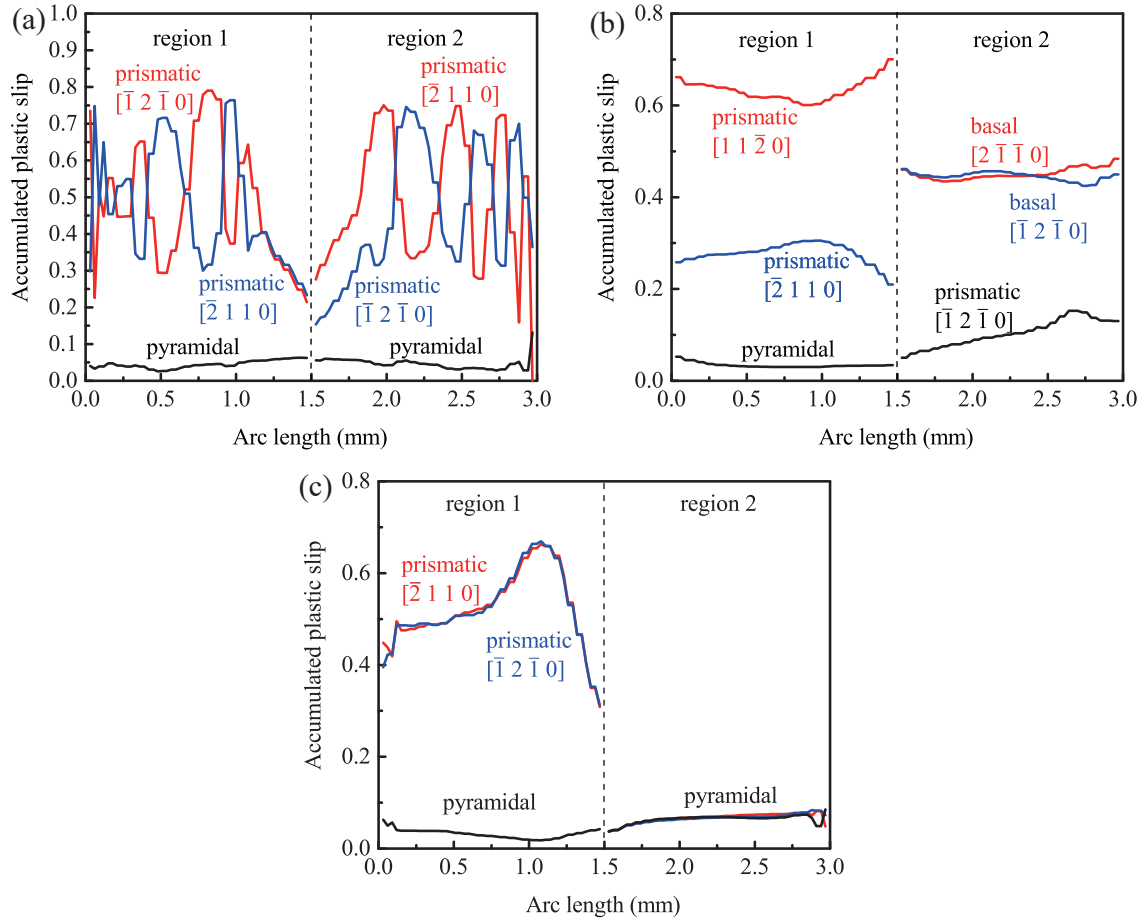
Figure 2.6: Accumulated shear strain of three most activated slip systems in each region: (a) 0° (axial) compression; (b) 45° compression; (c) 90° (radial) compression.

resulting macroscopic stress-strain curve for equal hardening is only slightly different from the simulation with distinct hardening values. However, the equivalent plastic strain and accumulated shear strain distribution vary significantly from Figure 2.4 and Figure 2.6(a). In the single-hardening-constant case, the equivalent plastic strain within the MTRs is essentially homogeneous at about 0.55. The pyramidal slip systems also contribute a larger fraction to the macroscopic plastic strain. Therefore, the single-hardening-constant model cannot accurately predict the MTR breakdown efficiency.

2.3.3 Lattice rotation

Previous experimental studies ([4]) revealed a profound influence of the slip system activity on the breakdown of MTR in Ti-6Al-4V. Also, slip system activity is influenced by the orientation of MTRs with respect to the compression direction. Presently, the CPFE numerical simulations provide a prediction of the microtexture evolution to suggest which compression direction is more effective at breaking down the MTR. The following sections examine the texture that develops in the matrix and the MTR for each loading case. Also, the disorientation about the average deformed orientation is quantified within each MTR.

Matrix texture evolution

The texture of the matrix after high temperature compression contains two dominant components, similar to the macrotextures in [3, 13]. For the major component, the c-axis is within $15° - 30°$ of the compression direction with random distribution around the compression axis. The other major component consists of α_p particles for which the c-axis is perpendicular to the compression direction. For brevity, matrix pole figures are not shown. The results for all 3 loading directions are quantitatively similar such that the individual MTR at 5 % volume fraction do not impact the bulk matrix response.

Compression $0°$ to billet axis (axial compression)

The lattice rotation evolution within the MTRs differs significantly from that of the matrix. Pole figures of region 1 and region 2 after primary processing are shown in Figure 2.7 (a) and

(b), respectively. Figure 2.7 (c) shows the experimentally measured pole figure of the test specimen after $0°$ (axial) compression at 1172 K, with the final true strain of 1.07 (i.e., a 3 : 1 reduction). For both regions, the loading axis is perpendicular to $(10\bar{1}0)$, and prismatic slip systems are most activated (see Figure 2.6 (a)). Generally, the c-axis remains fixed, while other crystallographic directions exhibit very large rotation around the c-axis ($< 30°$). The orientation of both regions is unstable such that different α_p particles have either a positive or negative rotation about the transverse (radial) axes. Similar randomization is observed in the EBSD measurement of Figure 2.7 (c), where the $(10\bar{1}0)$ pole figure exhibits much reduced intensity compared with the specimen response for other compression directions, shown in later figures. However, the texture components in the (0001) pole figure still remain relatively strong ($\sim 1.5\times$random). Logical explanations for why the $0°$ (axial) compression causes unstable lattice rotation are given in Section 2.4.1.

The spatial distribution of lattice rotation is also critical for assessing the breakdown of MTRs. Figure 2.8 shows the cross-section plot of the orientation map for $0°$ (axial) compression on the deformed configuration. The compression direction is along the horizontal direction of the figure. For both regions, in-plane rotation around the c-axis is obvious at both the MTR boundary and interior, indicating that breakdown of this region is effective. However, the change of the c-axis direction is quite limited, so that the basal planes of most α_p particles are still aligned.

Compression $45°$ to billet axis

Unlike $0°$ (axial) compression, lattice rotation is much more obvious when the compression direction is $45°$ to billet axis (Figure 2.9), although the orientation spreading is limited. In region 1 (Figure 2.9 (a)) where the c-axis is perpendicular to the compression direction, the basal-plane does not rotate while the slip plane of the most activated slip system rotates toward compression direction. Since only prismatic slip systems are activated, and the initial orientation distribution is homogeneous, spreading of texture components within this region is very limited ($< 10°$). On the other hand, for region 2 (Figure 2.9 (b)) where the c-axis is $45°$ to the compression direction, the normal direction of the basal slip plane rotates about $15°$ towards the compression direction. This lattice rotation comes mainly
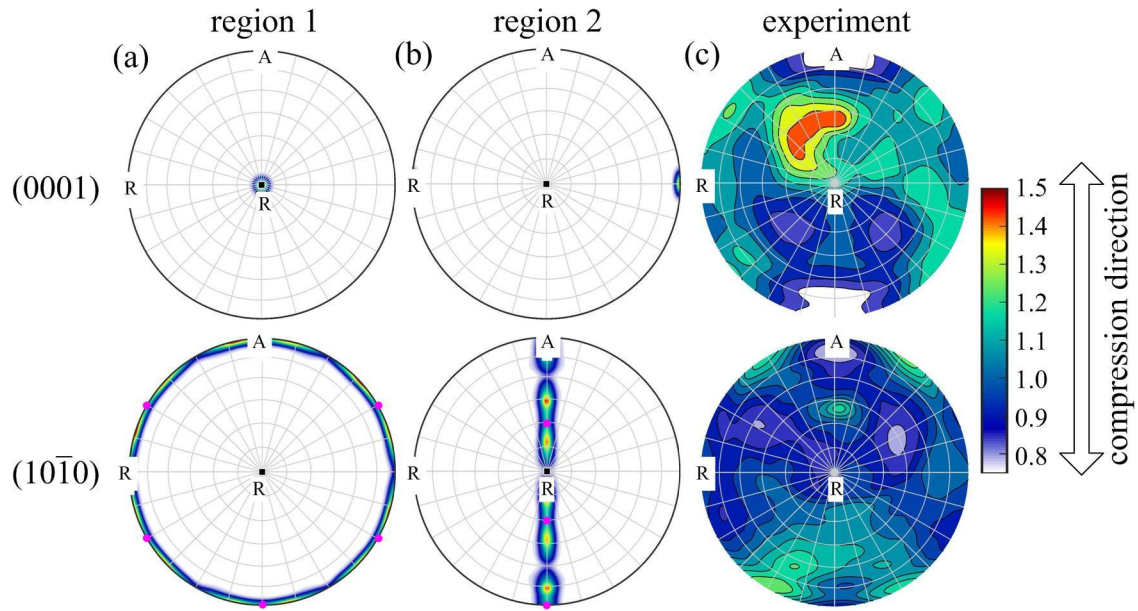
Figure 2.7: Pole figures corresponding to 0° (axial) compression: (a) region 1 from CPFE ($\varepsilon = -0.51$); (b) region 2 from CPFE ($\varepsilon = -0.51$). Magenta dots denote the initial MTR orientation. (c) EBSD measurement ($\varepsilon = -1.07$). The EBSD measurement ([69]) also includes α_p particles with other orientations besides the major components adopted in simulation (same for the following figures).
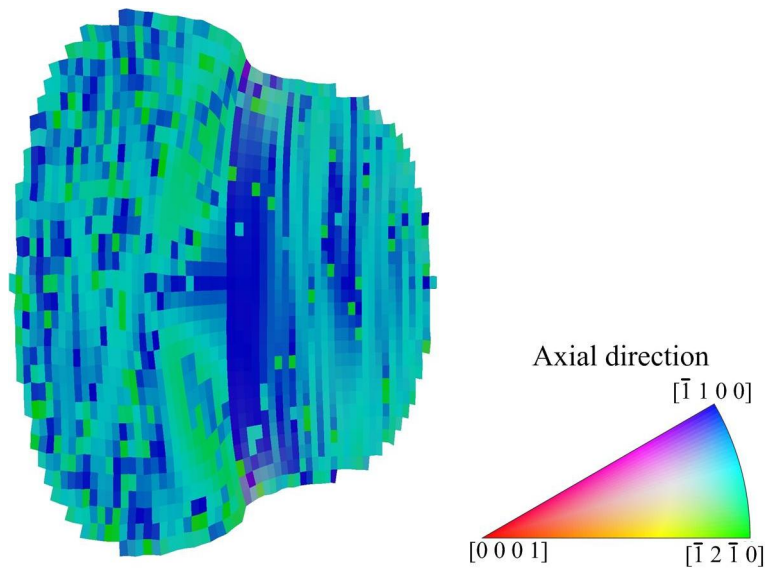
Figure 2.8: Orientation map of MTRs with respect to axial direction after 0° (axial) compression ($\varepsilon = -0.51$, cross-section view on the mid plane)
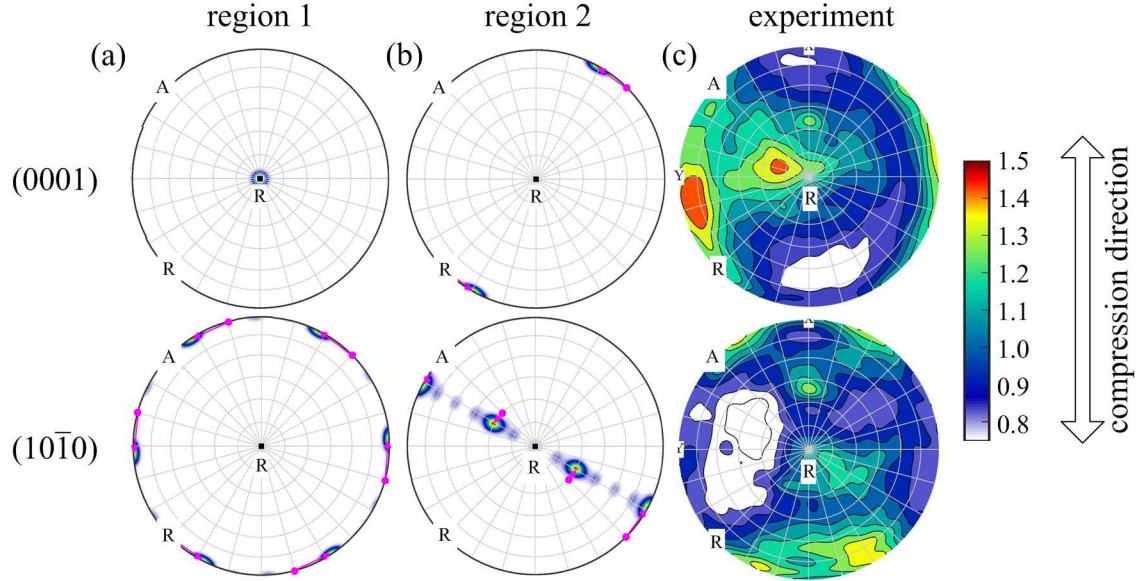
Figure 2.9: Pole figures corresponding to 45° compression: (a) region 1 from CPFE ($\varepsilon = -0.51$); (b) region 2 from CPFE ($\varepsilon = -0.51$). Magenta dots denote the initial MTR orientation. (c) EBSD measurement ($\varepsilon = -1.07$).

from the boundary condition induced macroscopic strain instead of particle interaction and local instability. Similar lattice rotation is also observed in EBSD measurement in Figure 2.9 (c), where the major texture components co-rotate instead of spreading out. However, in EBSD measurement, it seems that the normal direction of basal slip plane rotates towards the transverse direction (perpendicular to the compression direction), while ($10\bar{1}0$) components rotate towards compression direction. This difference is probably caused by the different loading direction with respect to the MTR orientation, since the c-axis is not evenly distributed along radial direction. It is still reasonable to conclude that, for 45° compression, although the lattice rotation is large, the spreading of major texture components within each MTR is still quite limited.

Compression 90° to billet axis (radial compression)

Finally, for 90° (radial) compression, lattice rotation and spreading within each MTR is shown in Figure 2.10. In this case, the c-axis is perpendicular to the compression direction in region 1, while it is parallel to the compression direction in region 2. This is the most interesting case in practice, since region 2 is well known for its difficulty to break down

and high potential for crack initiation when loaded along the compression direction at room temperature. Our results show that both regions still behave stably when the specimen is compressed at 1172 K. It is interesting to find that after such large deformation, MTRs are not noticeably broken down, and the average of each deformed texture component coincides with that of the initial configuration, suggesting that both MTRs behave as stable regions under this compression direction. Only minor spreading of the c-axis is observed in region 2 (hard orientation) for the (0001) pole figure, coinciding with the activity on the pyramidal slip systems in Figure 2.6 (c). Therefore, 90° (radial) compression is a stable compression direction, where rotations of α_p particles are quite limited. Similarly, the EBSD measured pole figure also shows strong texture components even after 1.07 true compression strain. Compared with simulated texture components, the pole figure from EBSD measurement is very similar to the region 1 pole figure, while the texture component of region 2 is not observed. Since the compression specimen was taken randomly from the mid-radius position of the billet, the texture component corresponding to region 2 may not have been present in the specimen. Although the initial orientation is pristine, we can still conclude that subtransus compression along the radial direction is not a very effective path for MTR breakdown.

Remark: *The CPFE simulations use exemplary microstructures with a pair of representative MTR to investigate the influence of compression direction on MTR breakdown efficiency, as opposed to the real yet complex microstructure shown in Figure 2.2 (c). The advantage of this simplified approach is that the simulation size can be reduced (which is still very large), and the influence of external force can be isolated and analyzed independently. On the other hand, the disadvantage is also obvious: there is a larger discrepancy between CPFE and EBSD measurement, especially for the reference experimental case where only one extrusion processing is applied and the initial texture component is not sharp enough. However, by comparing the three loading direction results for the CPFE simulations and EBSD measurements as distinct groups, we can still find interesting common features which support our major conclusions: (1) the most smooth and dispersed $(10\bar{1}0)$ pole figure appears in the 0° (axial) compression case (Figure 2.7); (2) the most obvious lattice rotation occurs in the 45° compression case (Figure 2.9); and (3) the strongest texture components remain*
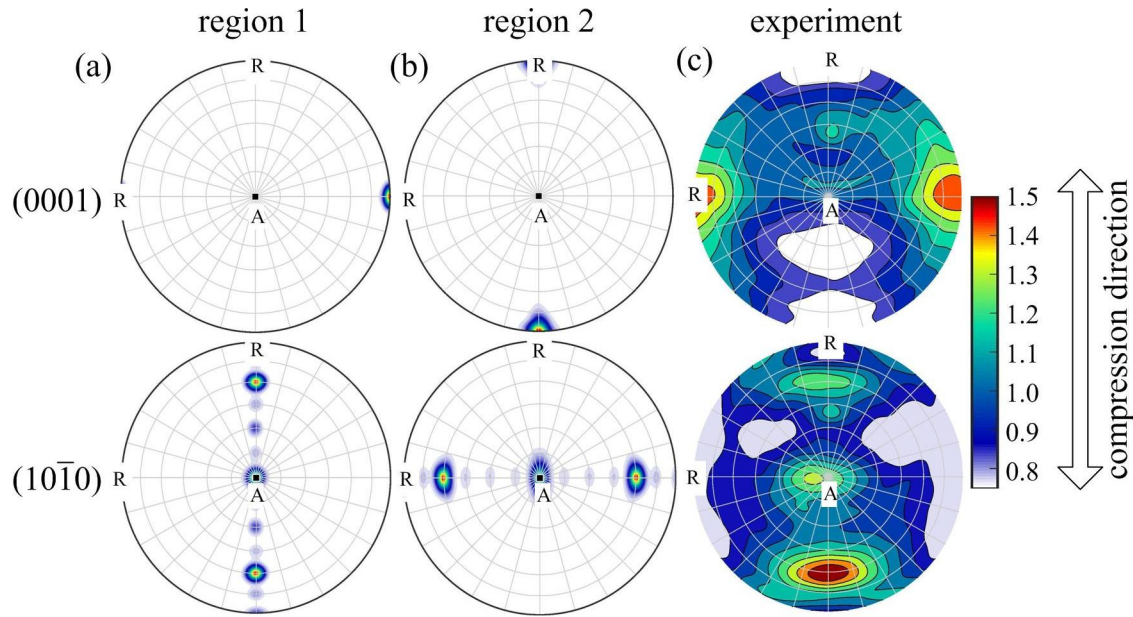
Figure 2.10: Pole figures corresponding to 90° (radial) compression: (a) region 1 from CPFE ($\varepsilon = -0.51$); (b) region 2 from CPFE ($\varepsilon = -0.51$). The location prior to deformation coincides with that at -0.51 true strain. (c) EBSD measurement ($\varepsilon = -1.07$).

in the 90° (radial) compression case (Figure 2.10). Certain major texture components are also consistent between the simulations and experiments, but not all of them.

Disorientation distribution

The pole figures qualitatively suggest that axial compression shows random lattice rotation around c-axis, 45° compression has bulk rotation but limited disorientation, and radial compression has minor disorientation of the c-axis. The disorientation distribution within each MTR is employed to quantify the breakdown efficiency. Figure 2.11 shows the probability density distribution of disorientation with respect to mean orientation within each MTR after compression. Disorientation distribution behaves quite differently when the compression direction is 0°, 45° and 90° to the billet axis. Specifically, for region 1, the breakdown efficiency of 45° compression is only slightly less compared with loading 90° (radial) compression, both of which are less compared with 0° (axial) compression. Similarly, for region 2, disorientation distribution after 0° (axial) compression is much larger than 45° compression. We note that the disorientation distribution for the 90° (radial) compression case is the most spread out of all cases other than the 0° (axial) case, indicative of the minor
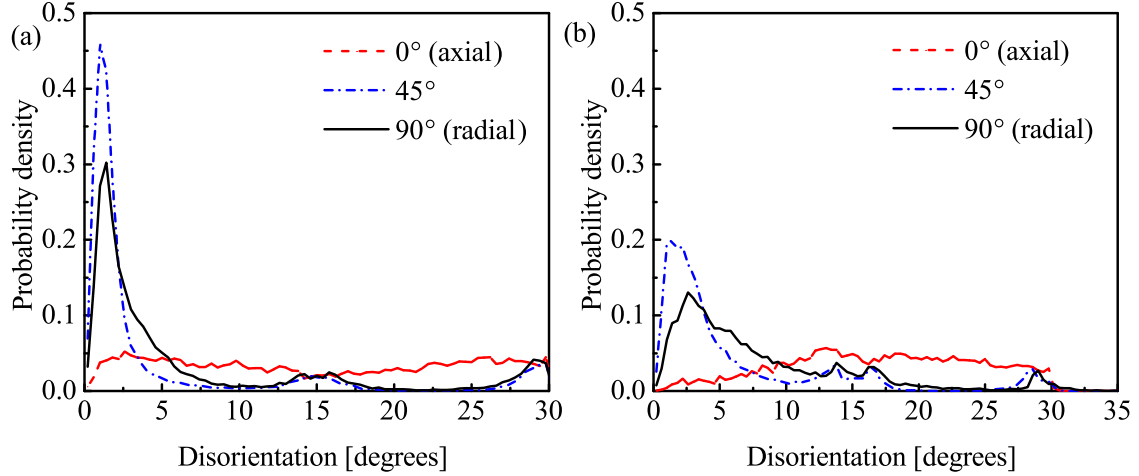
Figure 2.11: Disorientation distribution within MTRs after compression at 1172 K to -0.51 true strain: (a) region 1; (b) region 2. Horizontal axis is the average disorientation with respect to the mean MTR orientation after compression. The maximum disorientation value was deliberately limited to 30°, since the actual disorientations are almost all about the c-axis.

c-axis rotation that occurs as in Figure 2.10(c). Overall, disorientation for the majority of elements in the MTR is less than 10° for 45° compression and 90° (radial) compression. The limited disorientation in 45° compression and 90° (radial) compression is mainly because the MTR is oriented such that the normal of a stable crystallographic plane coincides with the compression direction ([70]).

To further investigate the characteristic disorientation distribution pattern for each loading case, disorientation of each α_p particle (finite element) with respect to mean rotation is shown in Rodrigues space where hexagonal-hexagonal symmetry is considered, as shown in Figure 2.12. In general, the disorientation distribution pattern in Rodrigues space is quite different when external loading is 0°, 45° and 90° to the billet axis. When the compression direction is parallel to the billet axis, α_p particles mainly rotate around the c-axis, and the rotation angles are almost evenly distributed. Although the disorientation within both regions for axial compression is very large, the c-axis still remains similarly oriented. When the compression direction is 45° to the billet axis, both c-axis rotation and rotation around the c-axis are limited. The smaller clusters of disorientation at 15° and 30° disorientation may be caused by the interaction between MTR boundary layer and the surrounding matrix. When compression is 90° to the billet axis, the disorientation is fairly limited especially in
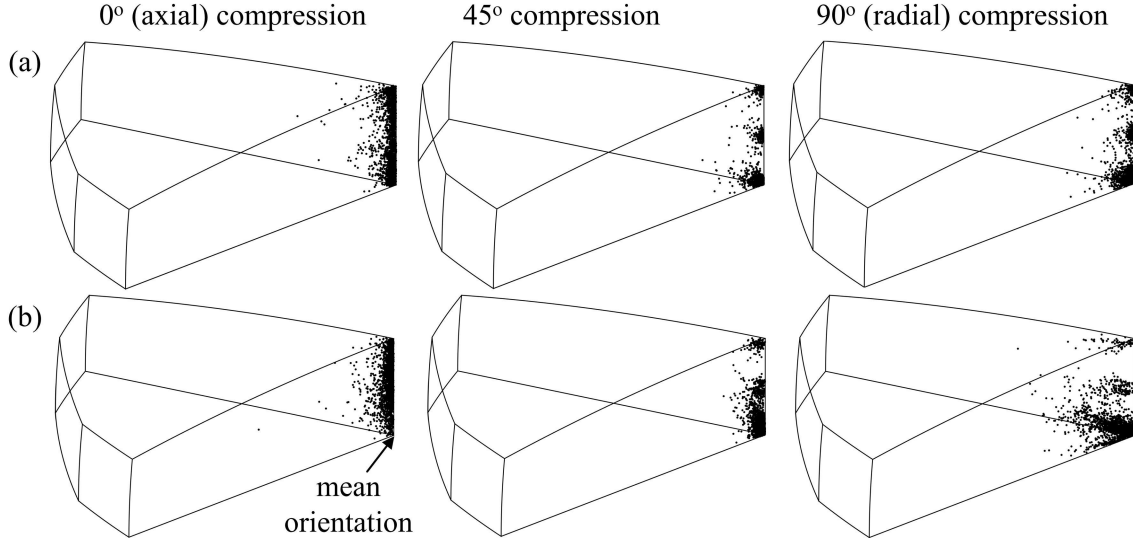
Figure 2.12: Disorientation distribution in Rodrigues space after compression at 1172 K to −0.51 true strain. The disorientation is calculated by multiplying inverse rotation matrix and mean rotation matrix, which represents the orientation deviation of each element with respect to the mean orientation after compression. The hexagonal-hexagonal symmetry is considered: (a) region 1; (b) region 2

region 1 that is in a stable orientation with respect to the external loading. The c-axis rotation is mildly evident in region 2 where compression direction is perpendicular to (0001) plane. The c-axis spreading of 90° (radial) compression is the largest among the three cases, though its extent is limited by the ability to deform plastically. It is also worth noting that the 45° and 90° compression cases produce distinct concentrations at 0°, 15° and 30°. These less intense peaks are mainly associated with finite elements at the MTR boundaries.

2.4 Discussion

In this study, a crystal plasticity finite element (CPFE) model was used to investigate the influence of compression direction on MTR breakdown efficiency in Ti-6242 during primary processing. The main modeling assumption was that slip-based deformation in α_p particles controls the evolution of texture components at 1172 K. Also, a previously developed phenomenological based model for room temperature behavior was extended to consider strain softening at processing temperature. To account for plastic anisotropy and unequal slip resistance, a general stress update procedure was developed for crystal plasticity

constitutive models with multiple hardening variables. Simulation results of paired MTRs under compression demonstrate a significant influence of compression direction on the plastic strain distribution, slip system activity as well as lattice rotation.

A mechanism-based explanation for why some colonies randomize during deformation while others persist was discussed previously by [4]. The authors found that orientations with a high Taylor factor that are amenable to slip on multiple families of slip systems would result in more randomization compared to those oriented for slip on a single family of slip planes. In the latter case, all particles would tend to co-rotate due to the restricted slip while the availability of multiple slip planes promotes more heterogeneous deformation within colonies. The most difficult colonies to spheroidize have c-axis parallel to the compression direction and hence need to operate the higher strength pyramidal $\langle c + a \rangle$ slip systems to deform.

Our current investigation provides a deeper understanding of the MTR-breakdown process with different compression directions. An interpretation of this influence is suggested by the analysis of reorientation velocity divergence as described below.

2.4.1 Reorientation velocity and divergence field

The lattice rotation rate vector $\dot{\mathbf{r}}^\mathbf{e}$ and its divergence div $\dot{\mathbf{r}}^\mathbf{e}$ was originally employed in Euler space to characterize the texture evolution of ideal texture components ([84]). Recently, both $\dot{\mathbf{r}}^\mathbf{e}$ and div $\dot{\mathbf{r}}^\mathbf{e}$ were expressed in the Rodrigues fundamental region of the FCC symmetry group to investigate grain fragmentation in hot-deformed aluminum ([70]). In the current investigation, $\dot{\mathbf{r}}^\mathbf{e}$ and div $\dot{\mathbf{r}}^\mathbf{e}$ are expressed in the fundamental zone of the HCP symmetry group to quantify the MTR breakdown efficiency under uniaxial compression. Figure 2.13 explains the relationship between initial orientation and lattice reorientation velocity based on the Taylor model assumption. Figure 2.13 shows the magnitude and divergence of the reorientation velocity field in the Rodrigues' fundamental zone (FZ). The FZ was first discretized into a mesh containing 9000 nodes by 10-node tetrahedral finite element shape functions, where the spatial coordinate of each node gives the axis-angle representation of the initial orientation. These axis-angle coordinates were transformed into Euler angle triplets and supplied to a Taylor-homogenized crystal plasticity simulation. Then after 0.08
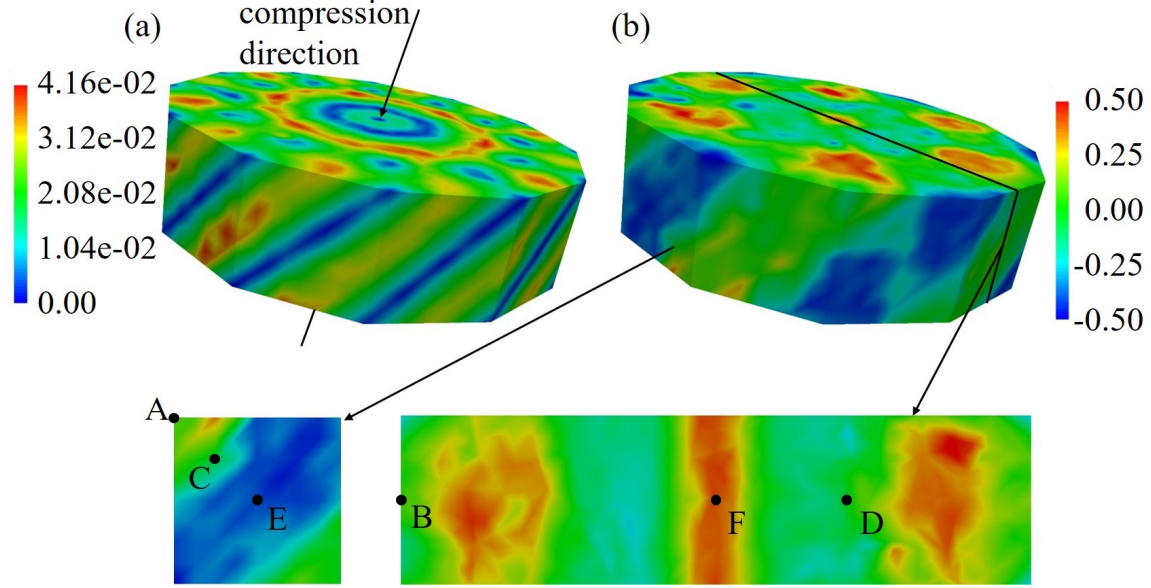
Figure 2.13: Lattice rotation velocity and its divergence expressed in Rodrigues' fundamental zone after compression at 1172 K to -0.08 true strain: (a) lattice rotation velocity; (b) divergence of lattice rotation velocity. Point A, C and E represents the initial orientation of region 1 for 0°, 45° and 90° compression. Point B, D and F represents the initial orientation of region 2 for 0°, 45° and 90° compression.

Table 2.4: Rotational velocity in Rodrigues' fundamental zone

		rotational velocity	divergence
0°	region 1	1.90×10^{-9}	9.53×10^{-2}
compression	region 2	5.00×10^{-10}	7.94×10^{-2}
45°	region 1	3.01×10^{-2}	-7.76×10^{-2}
compression	region 2	2.21×10^{-2}	-1.15×10^{-1}
90°	region 1	9.96×10^{-8}	-4.16×10^{-1}
compression	region 2	2.13×10^{-3}	4.11×10^{-1}

compression strain with large enough plastic strain and lattice rotation, the final orientations were transformed back to axis-angle representation. In this way, the reorientation velocity on the 9000-node mesh is defined as the orientation increment in Rodrigues' space divided by the time step. The divergence of the interpolated reorientation velocity field is then obtained by calculating the trace of its gradient tensor field using the shape function derivatives. This velocity field is not the actual reorientation velocity in axis-angle notation, since Rodrigues' space is not a linear vector space and does not follow the typical parallelogram law for vector addition. Nevertheless, this velocity field serves as a valid indicator of the orientations that tend to break down and is appropriate for the following analysis.

The magnitude and divergence of the reorientation velocity field is shown in Figure 2.13. The magnitude field represents the lattice reorientation velocity, while the divergence field reflects the stability of the initial orientation under fixed compression direction. A positive divergence indicates the possibility of increasing disorientation under compression, while negative divergence leads to decreasing disorientation. The reorientation velocity and divergence are influenced by both the c/a ratio and the CRSS of each slip system. The values corresponding to the initial orientations shown in Figure 2.3 are then extracted and shown in Table 2.4. Generally, the reorientation velocity magnitude field does not correlate with the divergence field, indicating that the reorientation stability is not determined by the magnitude of reorientation velocity alone.

When the compression direction is parallel to the billet axis (axial compression case), the MTRs with stable orientations are compressed along $[10\bar{1}0]$ direction. Then, the average rotational velocity is almost 0 and the divergence of rotational velocity (point A, B for region 1 and 2 in Figure 2.13) is positive according to the Taylor model prediction. This means that both regions are in a metastable initial orientation where small perturbation from this balanced position will increase rotational velocity significantly. This is consistent with the orientation deviation of each element with respect to the mean orientation after compression as shown in Figure 2.11 and Figure 2.12, where orientation dispersion is obvious. Also, the equivalent plastic strain in both regions (~ 0.60) is about 20 % larger than macroscopic true strain in Figure 2.6, which further increases the disorientation.

For the 45° compression case, the divergence of reorientation velocity field is negative (point C, D for region 1 and 2 in Figure 2.13), even though the rotational velocity is relatively large. The Taylor model is also consistent with Figure 2.11 and Figure 2.12, where orientation deviation with respect to the mean orientation after compression is negligible. This happens when one single slip system, either basal or prismatic, is activated, or the accumulated shear strain of two slip systems are equal and homogeneously distributed within the MTR (Figure 2.6(b)). Therefore, the entire region rotates as a unit towards one direction with limited orientation dispersion.

When the compression direction is 90° to the billet axis, the behavior of lattice rotation is quite different. In region 1 where this compression direction is along $[11\bar{2}0]$ direction, the

39

rotational velocity is relatively small and the divergence is negative (point E in Figure 2.13), even though two slip systems are activated (Figure 2.6). Figure 2.11 and Figure 2.12 also exhibit similar trends for region 1 where the orientation deviation is negligible. In region 2, the average rotational velocity is relatively large and the divergence is positive (point F in Figure 2.13), indicating that region 2 should be broken down efficiently. However, this large value is only true for the Taylor model where the equal strain assumption is adopted and greatly exceeds the CPFE computed response in Figure 2.11 and Figure 2.12. In fact, the compression direction is perpendicular to the basal plane in this region, and only pyramidal slip systems are activated (see Figure 2.6). The actual equivalent plastic strain in region 2 is only about 40 % of the average equivalent plastic strain in region 1 (Figure 2.5). Therefore, the lattice rotational velocity is much smaller compared with the Taylor model prediction but nonetheless shows dispersion. The divergence of the reorientation velocity field computed from the Taylor model is only an indicator of the breakdown efficiency, the quantification of which also depends on the amount of plastic strain in the local vicinity of the material.

2.4.2   Major assumptions and future work

Although the strain softening behavior for compression at 1172 K is comparable between the simulation and the experimental results in [69], our investigation is based on several assumptions that future research should revisit. First, our simulations assume that evolution of texture component is controlled by slip-based deformation of α_p particles. Actually, the β transus temperature of Ti-6242 is 1268 ± 15 K, and the volume fraction of α_p particles is about 75 % at 1172 K ([69]). Since the texture component of the matrix is well captured and we are focused more on the interaction of α_p particles, adopting only α phase in the simulation appears to be justified. A similar assumption is adopted for the MTS model based simulation of Ti-5553 (near β) compression at elevated temperature ([53]), where α phase substitutes about 30 % of β matrix at 1073 K and only BCC β phase is considered. It becomes increasingly important to account for the β phase as the deformation temperature increases, particularly when individual alpha particles are entirely surrounded by β matrix. Hence, the differences in flow stress and rate sensitivity can play an important role on strain partitioning between the constituent phases.

Notwithstanding the axial compression case, the extent of MTR breakdown in the simulation is less than the experimental result in [22]. One possible explanation is that the initial slip resistance of each slip system is not well defined by existing test data, and differential latent hardening is not considered in the model, i.e. q_{ij} equals 1. The relative slip resistance for basal, prismatic and first order pyramidal is held fixed at 1:0.67:3.0 according to the critical resolved shear stress measured at 1088-1228 K in [77], which is for Ti-6Al-4V. Accurate calibration of the relative resistance can help to further optimize the study of compression direction on breakdown efficiency ([4]). Another limitation is that the current microstructure model neglects the initial orientation distribution within each MTR. Further simulations are needed to determine the sensitivity of this distribution on the MTR response. Also, the maximum true strain reached by the simulations is -0.51 due to convergence issues caused by mesh distortion within the Lagrangian formulation. Larger compressive strain could be applied if an adaptive remeshing technique is employed.

In summary, the current research provides useful information on the simulation of Ti-6242 α/β processing and the influence of compression direction on the MTR breakdown process. Plastic strain distribution, slip system activity and lattice rotation within each microtextured region depend significantly on compression direction. Realistic α_p particle geometry with MTRs accounting for misorientation distribution will be employed in future work to explore in greater detail the breakdown of MTRs in Ti-6242 during primary processing.

2.5   Conclusion

For the first time, crystal plasticity finite element modeling was employed to investigate the influence of compression direction on MTR breakdown efficiency during primary processing. The major conclusions are summarized as follows:

1. The extended crystal plasticity constitutive model captures the strain softening behavior of Ti-6242 at 1172 K observed in hot-compression experiments.

2. To account for plastic anisotropy and unequal slip resistance, an implicit stress update algorithm based on Green-Naghdi stress rate is extended. This algorithm provides

a general framework for conveniently implementing models with multi-hardening variables, using isolated model-dependent terms.

3. Compression direction has a significant influence on the plastic strain distribution, slip system activity and lattice rotation within MTRs. The pole figures obtained from CPFE simulations are qualitatively consistent with the EBSD measurement of evolved texture of samples from an extruded Ti6242 billet.

4. For $0°$ (axial) compression, disorientation within MTRs is obvious but c-axis still remains aligned. For $45°$ compression, lattice rotation occurs but all α particles co-rotate such that MTRs remain stable. For $90°$ (radial) compression, the (0001) texture component is most scattered when the basal plane is perpendicular to external load, but the efficiency is limited by its high slip resistance. These conclusions are consistent with the analyses based on the reorientation velocity and divergence in Rodrigues' space, where uniform strain assumption is applied.

Chapter 3

Mechanical interaction of alpha and beta phases in Ti-6242 at high temperatures

3.1   Introduction

Simulations of c-axis breakdown in microtextured regions (MTR) in Ti-6242 using crystal plasticity finite element method were conducted in previous section. These studies consisted of two ellipsoid alpha phase regions with single orientation embedded in a uniform-textured matrix. Two extensions to these studies were performed herein. First, the strain history from selected material points in the prior simulations were imposed onto microscale models of clustered α particles with initial texture representative of orientation spread within an MTR, and sharpening or softening of texture was compared with the mesoscale results. Second, microstructure models of Ti-6242 at higher processing temperatures with greater than zero beta phase fraction were simulated to study interaction of α particles as a function of separation and orientation. In both cases, specific initial crystal orientations were found to develop large orientation gradients.

3.2 Motivation for computational modeling of micro-textured regions

The titanium alloy Ti-6242 (Ti-6Al-2Sn-4Zr-2Mo) has been the structural material of choice for use in high-pressure compressors for gas turbine engines of aircraft due to its high strength-to-weight ratio and excellent high temperature mechanical properties. However, Ti-6242 is susceptible to dwell fatigue at low temperature due to crack growth on low-angle boundaries along the primary α grains, in particular small faceted cracks that link up to form a "quasi-cleavage" surface. These low-angle boundaries occur within so-called microtextured regions (MTR) that consist of many neighboring primary α grains with similarly oriented [0001] axes of the hexagonal close-packed (HCP) atomic lattice. In post-mortem observations, Pilchak et al. observed facet clusters along the fracture surface within the MTR. Mill processing techniques impacting MTR distribution are currently under experimental investigation.

3.3 Approach

The scope of this section for crystal plasticity modeling of Ti-6242 involves two major phases. First, microscale models of clustered alpha particles with representative microtexture are subjected to various strain histories from mesoscale 1173 K microtexture simulations from previous term. Second, a constitutive model for the β grains of Ti-6242 is implemented in WARP3D to study the behavior of pairs of alpha particles embedded in the softer beta phase at higher temperatures.

3.3.1 Titanium crystal plasticity model calibration

In crystal plasticity (CP) theory, plastic strains arise from the motion of dislocations along preferential slip systems, where $\mathbf{b}^{(s)}$ is the slip direction within a crystal plane s and $\mathbf{n}^{(s)}$ is the unit normal to plane s. Ti-6242 contains α phase which is hexagonal close packed (HCP) and β phase which is body-centered cubic (BCC). The reduced symmetry of the HCP lattice gives rise to slip systems with highly disparate resistances to dislocation motion.

The constitutive model for Ti-6242 [10] is adopted for the alpha-phase to relate the plastic slip rates $\dot{\gamma}^{(s)}$, the resolved applied shear stress $\tau^{(s)} = \mathbf{b}^{(s)}\boldsymbol{\sigma}\mathbf{n}^{(s)}$, and the critical slip resistance $g^{(s)}$. The slip rate $\dot{\gamma}^{(s)}$ on each slip system s is taken as a power law expression involving the resolved shear stress $\tau^{(s)}$ and the slip resistance $g^{(s)}$:

$$\dot{\gamma}^{(s)} = \dot{\gamma}_0^{(s)} \left| \frac{\tau^{(s)}}{g^{(s)}} \right|^{1/m} \text{sign}\left(\tau^{(s)}\right), \quad \dot{g}^{(i)} = \sum_{i=1}^{n_{slip}} h^{(ij)} \left|\dot{\gamma}^{(j)}\right| = \sum_{i=1}^{n_{slip}} q^{(ij)} h^{(j)} \left|\dot{\gamma}^{(j)}\right| \qquad (3.1)$$

where $\dot{\gamma}_0^{(s)}$ is a reference strain rate and m is a constant exponent. The slip resistance evolution is expressed through a combination of self hardening and latent hardening:

$$h_{HCP}^{(j)} = h_0^{(j)} \left|1 - \frac{g^{(j)}}{g_s^{(j)}}\right| \text{sign}\left(1 - \frac{g^{(j)}}{g_s^{(j)}}\right), \quad g_s^{(j)} = \tilde{g}^{(j)} \left(\frac{\dot{\gamma}^{(j)}}{\dot{\gamma}_0}\right)^n \qquad (3.2)$$

The material parameters are calibrated for room temperature where hardening of the stress-strain response is apparent. At high temperatures, softening is observed, and therefore the material parameters of the model are re-calibrated using a homogenized iso-strain finite element model to address this observation. Three slip system families are considered: basal $\langle 11\bar{2}0\rangle\{0001\}$, prismatic $\langle 11\bar{2}0\rangle\{10\bar{1}0\}$, and 1st order pyramidal $\langle 11\bar{2}3\rangle\{10\bar{1}0\}$. The ratio of slip system strengths is held fixed at $1 : 0.67 : 3.0$ according to material response measured by Lee Semiatin and T.R. Bieler in 2001 [4]. The calibrated material parameters, obtained last term, are listed in Table 2.2 and 2.3, where the designations (1) = basal, (4) = prismatic, and (7) = pyramidal. The units of $\tilde{g}^{(j)}$, $h_0^{(j)}$, and $g_0^{(j)}$ are MPa; other parameters are unitless. For the β phase, which has a BCC lattice structure, a simplified Voce model with equal slip resistance across the 12 $\langle 111\rangle\{110\}$ systems was employed, since it is already implemented in WARP3D:

$$\dot{\gamma}^{(\alpha)} = \frac{\dot{\gamma}_0^{(\alpha)}}{\tau_v + \tau_w} \left| \frac{\tau_{rss}^{(\alpha)}}{\tau_v + \tau_w} \right|^{n-1} \tau_{rss}^{(\alpha)}, \quad \dot{\tau}_w = \theta_0 \left|1 - \frac{\tau_w}{\tau_v}\right|^m \text{sign}\left(1 - \frac{\tau_w}{\tau_v}\right) \sum_{\alpha=1}^{n_{slip}} \left|\dot{\gamma}^{(\alpha)}\right| \qquad (3.3)$$

where τ_y is the yield flow stress and τ_v is the saturation hardening (softening) stress. According to the modeling approach of Dunst and Mecking supported by recent small scale experiments at high temperatures, the beta phase strength is set to approximately 1/3 of the
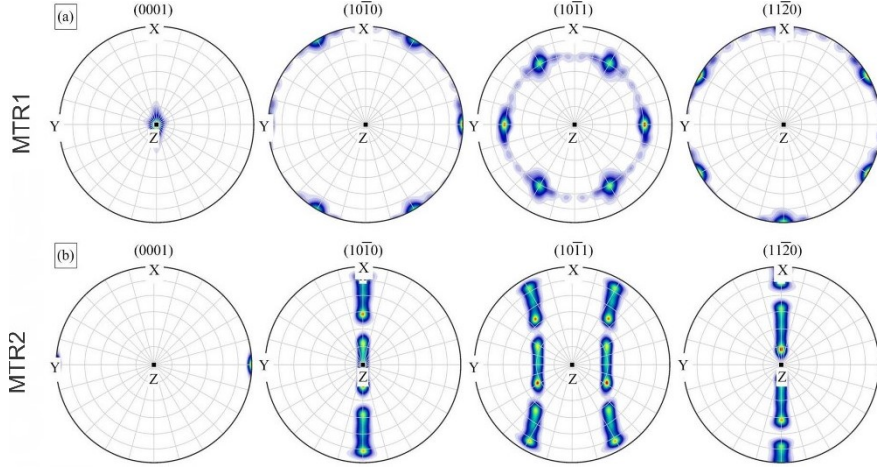
Figure 3.1: Pole figures of evolved texture within two microtextured regions loaded in z-direction at 1173 K.

prismatic slip strength. A 200-orientation iso-strain model was used for calibrating the beta parameters to match 1173 K flow curves from Adam Pilchak. Isotropic elastic moduli were adjusted from the values in [10] for higher temperature. The calibrated α-phase constitutive model was then applied to model the orientation breakdown of ideal microtextured regions (MTR) during the previous term.

3.3.2   Modeling setup

Highly resolved finite element models are developed with $100 \times 100 \times 100$ linear hexahedral finite elements for a cube with 0.5 mm edge length. Within the center of the 3D cell model, two MTR with single orientation are placed in close proximity; surrounding elements contain a random texture, as illustrated in the greenish square on the left of Figure 3.2. The 3D cell model is simulated under prescribed constant strain rate imposed as a uniform displacement increment on one face of the cube at a time. The strain rate is $\dot{\varepsilon} = 9 \times 10^{-3} \mathrm{s}^{-1}$. A maximum true strain of 0.51 is reached. Out of the six uni-directional load paths considered, the most efficient direction for MTR breakdown was the loading parallel to the c-axis in one MTR and activating multiple slip systems in the second MTR to induce an unstable orientation gradient, as shown through pole figures in Figure 3.1. Pole figures generated using MTEX package [52]. These mesoscale results help guide the microscale models conducted this term.

3.4 Results and discussion

3.4.1 MTR microstructure models of alpha particles

Actual MTR in Ti-6242 contain many α particles with similar but distinct c-axis alignment, illustrated by the experimental pole figure shown in the right of Figure 3.2. Therefore, we were interested to study if the initially heterogeneous makeup of an MTR, when deformed according to the mesoscale finite element simulations, would exhibit similar texture evolution, thereby justifying the prototypical modeling of MTR using mesoscale behavior as a guide. Thus, a microscale model was generated with 75 hexahedral elements along each edge and a log-normal distribution of grain sizes consisting of voxels, as shown in the red-blue cube in the center, containing about 800 particles. The input texture, from MTEX, was a $1.0\times$ intensity fiber plus a $1.5\times$ intensity unimodal component each with 7.5 degree half-width. Alignment of the poles was chosen to agree with the selected point from the mesoscale MTR, shown by the dots on the red-blue ellipsoid. Compression simulations were performed for 6 strain histories, taken from points in the diagonal x compression and uniaxial z compression mesoscale models. Finite elements are selected along the MTR centerline at outside, midpoint, and near-interface locations, and the deformation gradient is used to compute displacements to apply as periodic boundary conditions. Strain history from three points for the z-direction case are given in Figure 3.3, showing that the transverse axial strains as well as the shear strains are distinct. Thus, we can study the effect of mild strain path changes to the resulting texture evolution.

The resulting texture evolution for 3 points in the diagonal x load case are shown in Figure 3.4 through pole figures. The initial configuration exhibits the 7.5 degree half-width initial distribution. For both the MTR, which have different initial orientations, the texture sharpens to produce higher peak intensities. Thus, c-axis orientation of neighboring crystallites is expected to come closer together at the larger strain levels.

The intensity is particular for the second MTR, where the fiber texture has almost disappeared, retaining only a unimodal component. Thus, this loading direction is very ineffective at breaking down the initial microtexture. Also, dependence on the strain path
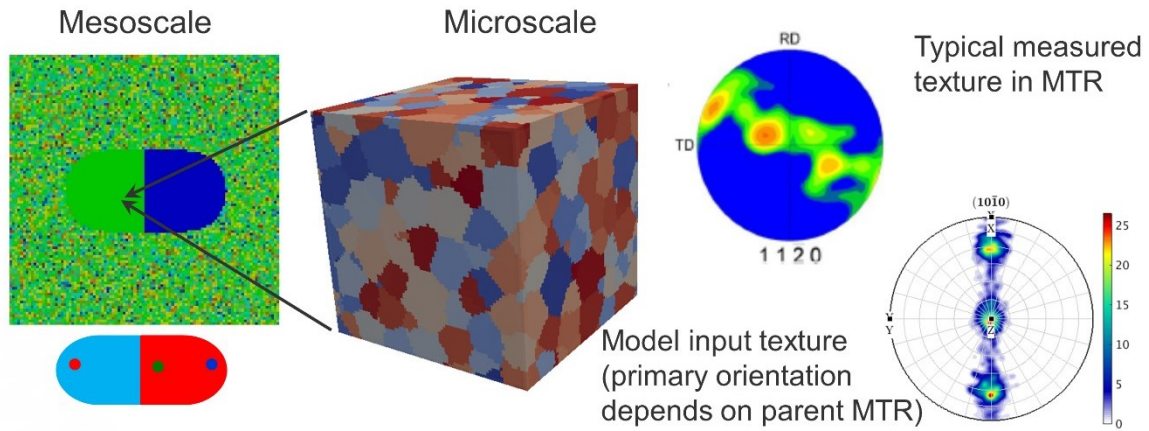
Figure 3.2: Description of microscale model of alpha particles within MTR subjected to strain path from individual finite elements at mesoscale; input texture contains fiber texture about mesoscale c-axis
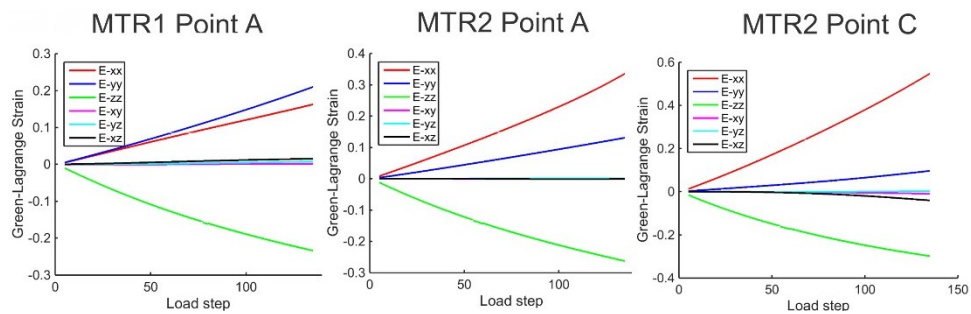
Figure 3.3: Green-Lagrange strain history of selected MTR points in z-direction compression simulation
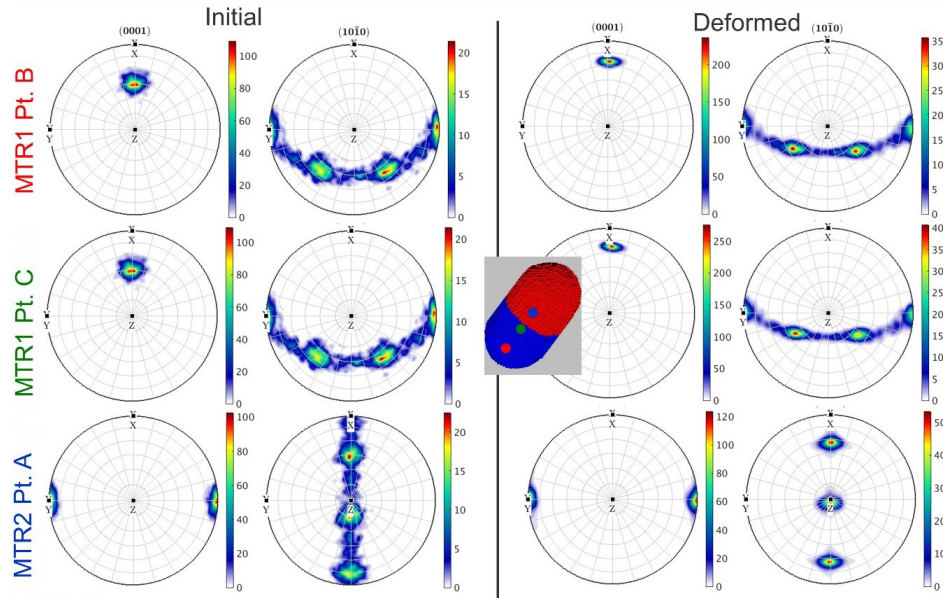
Figure 3.4: Texture development during diagonal x compression simulation. Texture components sharpen in both MTRs, and macro rotation of primary directions is evident
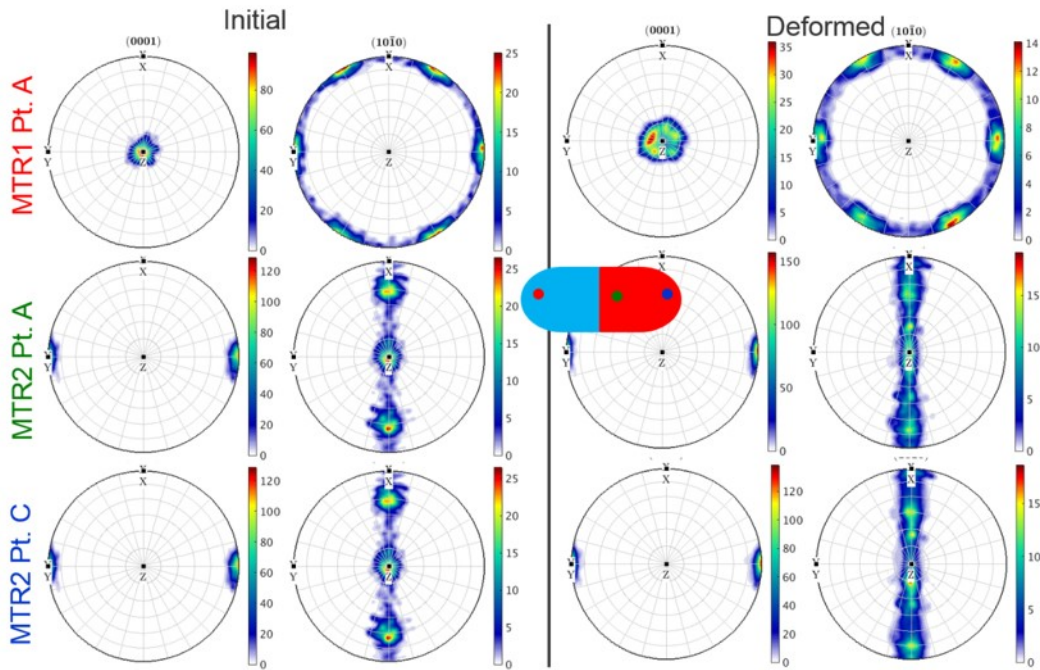
Figure 3.5: Texture development during uniaxial z compression simulation. Texture components soften in both MTR, unstable orientation apparent in MTR2
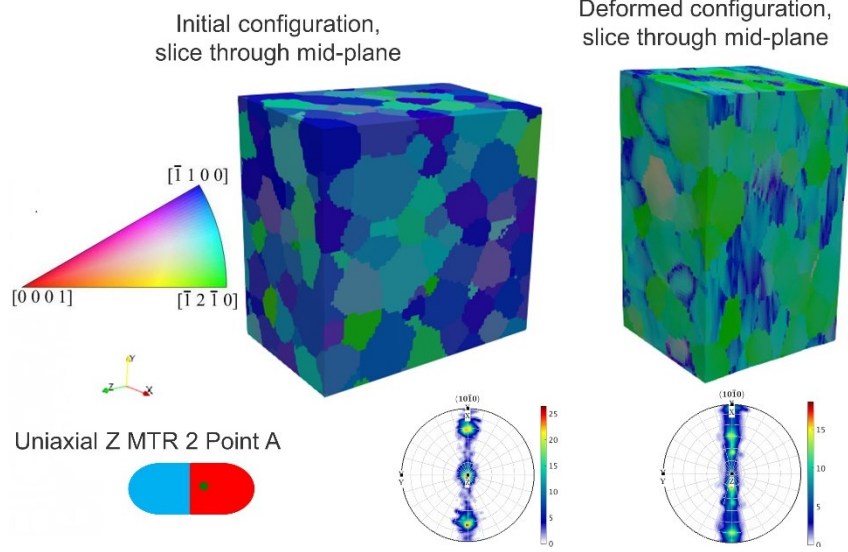
Figure 3.6: Spatial inverse pole figure of MTR2 (*c*-axis perpendicular to loading) before and after compression

for MTR1 is fairly mild. Bulk rotation of the MTR is also evident from the motion of the peaks by about $15 - 30°$ through the grid lines.

In contrast, the *z*-direction compression cases exhibit a softening of the texture components from the initial condition. The first MTR has *c*-axis parallel to loading direction, and the orientation spread increases from $15 - 30°$ in the (0001) pole figure after 50% strain. In the second MTR, the intensity of the (1010) pole figure also reduces by a factor of two, and the smearing of the unimodal to a fiber texture is also present for both strain histories. This behavior agrees with the mesoscale model of ideal initial orientation that develops orientation gradients; thus, orientation instability does not require a single perfect direction but can be triggered in imperfect starting texture as well. This is analogous to column buckling/bifurcation in structures, where critical load agrees for perfect and imperfect initial condition. This orientation gradient is visualized through Figure 3.6, comparing the inverse pole figure plotted on the microstructure in the undeformed and deformed states. Misorientation is present within certain grains.

The texture breakdown in the microscale simulations is quantified through the disorientation curves given in Figure 3.7. Disorientation is measured with respect to the mean orientation of the respective simulated domain, at the initial and final strain level. The curves in the left plots correspond to the mesoscale results from the previous term, highlighting the
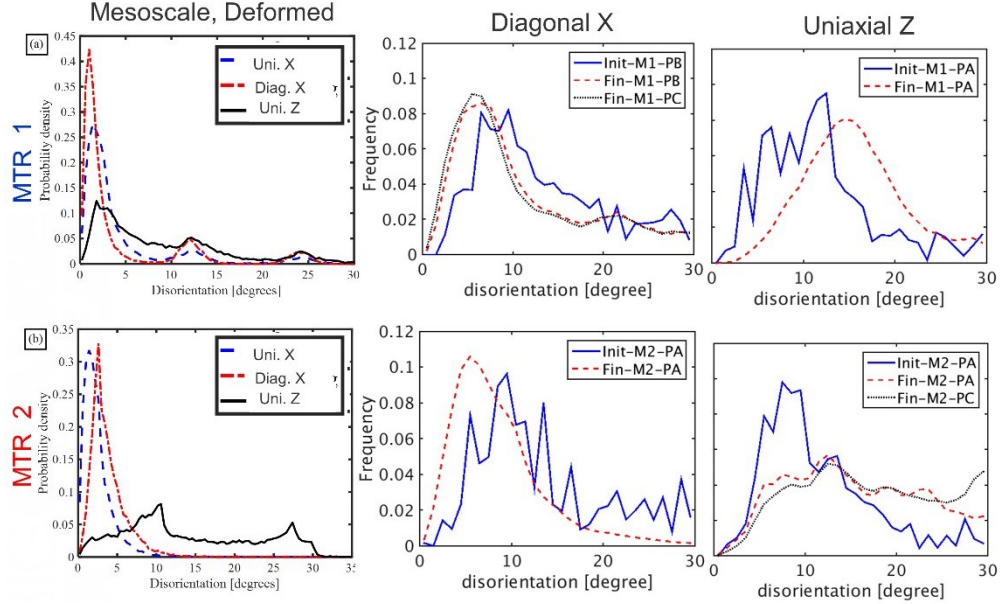
Figure 3.7: Disorientation with respect to mean orientation in MTR: mesoscale results from previous report, initial and final curves for diagonal x compression, and initial and final curves for uniaxial z compression

large disorientation for the z-compression case and the low disorientations in the other two cases. The disorientation from the microscale model with diagonal MTR shows a reduction in disorientation between the initial and final configuration; the peak has shifted to the left and intensified. Also, the final frequency distribution is smoother than the initial condition, which is true in all cases. In contrast, the z-compression case shows a spreading out of the distribution of disorientation angle and a reduction in the peak, showing effective breakdown. Also, the dependence of the behavior with respect to the strain path (comparing the blue and black curves) is a bit larger. In conclusion, microscale and mesoscale trends have strong correspondence, and z-case is most effective.

3.4.2 Interaction of alpha and beta phases

As the processing temperature increases, a greater percentage of softer BBC β phase is present in Ti-6242, typically greater than 75%. This reduces the required force to deform the billet, but also the soft phase may fail to induce much strain into the remaining α phase, and subsequent phase transformation during cooling can lead to unfavorably clustered textures of α particles. Thus, models are desirable to understand the stress and strain partitioning

51
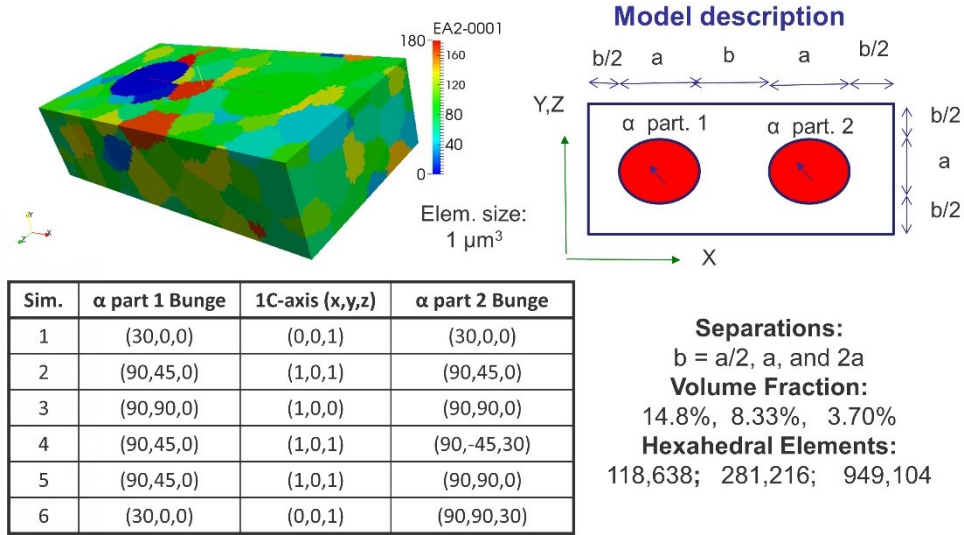
Figure 3.8: Description of alpha-beta phase models at 1173 K: separation of spherical alpha particles and orientation of each alpha particle for 18 individual simulations; log-normal distribution of beta-matrix

in bi-modal titanium during 1173 K processing. As a benchmark study, microstructures of beta-phase grains are generated as shown in Figure 3.8, with a random initial texture. Two spherical alpha particles are embedded in this matrix, with a diameter of 26 microns. Three separations of the particles are given, as multiples of the diameter, and correspond one-to-one with the volume fraction in the assumed periodic arrangement. Uniaxial compression is applied parallel to the x-axis (passing through both particles, in series) at a fixed strain rate $\dot{\varepsilon} = 9 \times 10^{-3}\mathrm{s}^{-1}$. Six combinations of c-axis orientations are selected for the alpha particles, given in the table below, with either identical or misoriented c-axes. A constant number of 26 hexahedral finite elements span the diameter of the alpha spheres, to fix the level of mesh resolution in the models.

Examples of the deformed configuration of the models are shown in Figure 3.9. The maximum strain before divergence in the c-axis parallel case was 20% due to the hard orientation; the spheres remained almost rigid, and the beta elements became highly distorted. Higher 60% max strain was achieved for the c-axis perpendicular cases, since the alpha particles deform as well, though about 1/3 less because of the slip resistance disparity. Since the levels of imposed strain are much lower than typical inputs for mill processes, these results are considered as preliminary and warrant further study for FE mesh robustness.
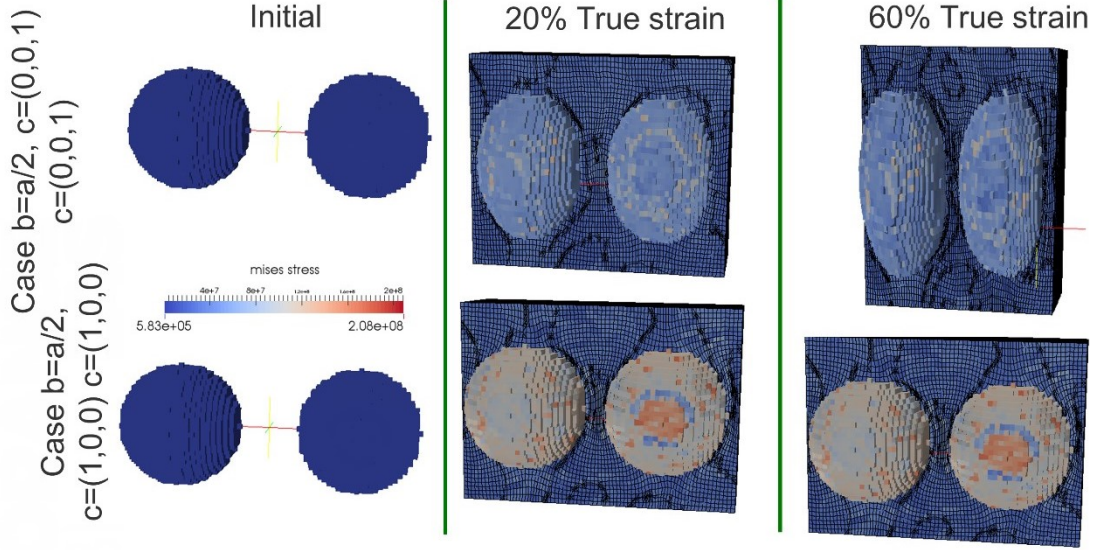
Figure 3.9: Deformed shape of alpha particles during compression and distortion of β-phase finite elements

Comparisons of disorientation developed at the maximum imposed strain for each orientation configuration and two particle separations are given in Figure 3.10. Disorientation is slightly greater for larger separation, and soft particles become less disordered when in series with hard particles than with soft particles. Note that the c-axis=(0,0,1) case was oriented at 30 degrees to have an orientation gradient.

3.5 Conclusion

Crystal plasticity modeling of alpha and beta phase Ti-6242 of mechanical processing at high temperature is performed using the WARP3D finite element code. Mesoscale results of texture evolution in ideal-oriented microtextured regions (MTR) from previous term were used to inform microscale models of alpha particle distributions to determine the effect of heterogeneity on the MTR evolution. For the cases of strain history imposed on the microscale models, the disorientation remained small when the mesoscale disorientation was small and became larger when the mesoscale exhibited larger disorientation. Orientation gradients develop for a particular alignment. While the c-axis parallel loading produced the largest breakdown, this loading also required 50% larger stress. Preliminary studies of alpha and beta phase mechanical interaction were conducted based on material parameters

Figure 3.10: Disorientation at max strain before divergence of FE solution in α-particles with 2 spacings

fitted to data for 1173 K. Distortion of finite elements representing the softer beta phase often led to FE convergence issues and limited the maximum compressive strain achieved. Orientation of c-axis of alpha particle with respect to loading direction had a much larger effect on disorientation versus particle separation.

Chapter 4

Highly efficient fast Fourier transform method[1]

4.1 Introduction

Mesoscale modeling has often been employed to investigate microstructure evolution under external loading, for example of polycrystalline or composite materials [73]. Image-based simulations of realistic microstructures enable comparisons directly with in-situ experiments. Such simulations usually require high resolution and thus present computational challenges. The finite element (FE) method is the prevailing numerical method to solve the governing equations of such problems. However, the FE method does not scale well for heterogeneous nonlinear materials because direct factorization of the global tangent matrix is required for robustness. As an alternative to the FE method, fast Fourier transform (FFT) based methods are becoming increasingly popular to solve boundary value problems defined over representative volume elements (RVEs) [55]. FFT-based methods are more efficient than the FE method, especially for large scale problems with refined mesh resolution [72], since the global matrix factorization is avoided. Also, FFT-based calculations are performed on regular grids, making it straightforward to transfer experimental data, including electron

---

[1]This Chapter has been adapted from "Ma, R. and Truster, T.J., 2018. FFT-based homogenization of hypoelastic crystal plasticity model at finite strains. Computer Methods in Applied Mechanics and Engineering, under review".

or X-ray diffraction measurements [82], directly to the simulations without requiring extra effort for mesh generation.

The FFT-based method was first proposed by Moulinec and Suquet [63, 64]. The periodic equilibrium equation is reduced to the Lippman-Schwinger (L-S) equation when the polarization field is projected onto a homogeneous reference material. The L-S equation is conveniently solved by the Green's function method, and this process is iterated until stress equilibrium is achieved. The numerical robustness and convergence behavior of this basic scheme has been improved by reformulating as the Eyre-Milton scheme [16] or the augmented Lagrangian scheme [58], both of which have been found to be special cases of the polarization scheme [62]. Recently, the basic scheme was reenvisioned as the Neumann expansion of a linear operator [16] and alternatively solved by Krylov subspace methods for higher efficiency [96, 28]. Later, variational frameworks of the FFT-based methods were proposed to deal with infinite contrast problems [5] and improve the performance of the basic scheme [91]. The latter, termed as the Fourier-Galerkin scheme, uses trigonometric polynomials as the shape functions, and the Green's operator is independent of the reference material. A Newton-Krylov method is used to solve the discretized nonlinear equations to enforce strain compatibility, and the conjugate gradient method proves to be the most efficient linear solver [61]. Recently, the Fourier-Galerkin framework was applied to solve infinitesimal strain problems [95] and finite strain problems [8]. Its consistent tangent stiffness can be explicitly implemented since this formulation is independent of the reference material.

The Fourier-Galerkin scheme, although efficient and robust, was not yet been extended to solve finite strain crystal plasticity (CP) problems, where extremely high efficiency is required to perform image-based simulations. Also, when solving either stress-driven or concurrent multiscale modeling problems, the homogenized tangent stiffness relating the effective RVE stress to effective RVE strain is advantageous for consistent linearization [14] compared with finite difference secant approximations. The homogenized stiffness was defined from the deformation energy point of view, but only upper and lower bounds were derived for linear elastic materials [92]. Thus, the algorithmic tangent stiffness has not yet been derived for the Fourier-Galerkin scheme, especially for highly heterogeneous nonlinear cases.

The FFT-based method was first applied to simulate polycrystalline material behavior by Lebensohn under small deformations [42]. This computational approach was then validated against in-situ experiments of polycrystalline copper [43]. However, until recently, only limited investigations were performed to solve finite strain CP problems using FFT-based methods. The first attempt was published by Eisenlohr et al. [14], based on previous work [40] for composite materials. Upon this framework, different FFT schemes (basic scheme, Eyre-Milton scheme, and augmented Lagrangian scheme) and nonlinear equation solvers (Richardson, GMRES, and inexact GMRES) were compared to find a robust and efficient combination to solve CP problems [79]. This scheme was further employed to calibrate the yield surface of AA3104 aluminum alloy by means of full-field virtual experiments with 500 grains [97]. Later, the efficiency of this scheme was enhanced by a semi-explicit time-integration CP formulation defined in the current configuration [66]. Other recent extensions include a finite difference approximation to remove ringing artifacts [90] and GPU parallel programming to accelerate the FFT evaluation [32]. Most of the aforementioned investigations are based on the fixed-point scheme with augmented Lagrangian method [58]. Thus, the numerical behavior depends significantly on the chosen reference material and consistent linearization is difficult to be performed.

The current investigation launches from the Fourier-Galerkin scheme [8], which is independent of the reference material and more efficient than other FFT-based methods [61]. A general interface is proposed between the FFT-based method and objective rate constitutive models, which is widely used in FE software including WARP3D [12]. One advantage of objective rate constitutive models compared with hyperelastic models is that small strain elasto-plastic models can be directly used without modification, including the return mapping algorithm. The consistent tangent stiffness is derived for this interface by pulling back the Jacobian matrix from the unrotated configuration to the reference configuration. Finite strain CP kinematic equations based on the Green-Naghdi rate were proposed in [50], providing a general interface for most existing CP constitutive models. Also, the algorithmic homogenized tangent stiffness is derived for the Fourier-Galerkin scheme, which is essential for concurrent multiscale modeling [35] and mixed boundary condition treatment [29]. The proposed local and homogenized tangent stiffness expressions improve

the convergence behavior of the Newton iteration and the conjugate gradient (CG) solver. The entire framework is implemented in FORTRAN utilizing OpenMP parallelism, and investigated through a series of finite strain CP examples with various levels of heterogeneity.

This chapter is organized as follows: In Section 4.2, the Fourier-Galerkin method is reviewed, and the homogenized tangent stiffness is derived for mixed boundary conditions and multiscale modeling. In Section 4.3, a general interface is proposed to combine the FFT-based method and objective rate constitutive models. The consistent tangent stiffness is pulled back directly from the unrotated configuration to the reference configuration. Numerical tests are used in Section 4.4 to verify and analyze the proposed FFT-based method against the FE method and other FFT-based methods. Also, the inexact Newton method is incorporated to further improve its efficiency. Section 4.5 summarizes the current investigation with major conclusions.

4.2   Homogenization of the Fourier-Galerkin method

This section begins with an overview of the Fourier-Galerkin method. Then the tangent stiffness homogenization of this scheme is derived, and it is applied herein to solve problems with mixed boundary conditions in an implicit fashion. Distinguishing implementation aspects are highlighted.

4.2.1   The Fourier-Galerkin method

The Fourier-Galerkin method is previously proposed in [91] and briefly summarized below. The relevant boundary value problems are defined in a regular shaped representative volume element (RVE) denoted by B, which is a rectangle for 2D problems and a cuboid for 3D problems (Figure 4.1). Heterogeneous materials are represented in this region through a discretization into pixels (2D) or voxels (3D), and periodic boundary conditions are prescribed.

For finitely-deforming bodies under quasi-static conditions, the balance of linear momentum can be expressed in the reference configuration as

$$\text{Div}\,\mathbf{P} = \mathbf{0} \text{ in } B, \quad \mathbf{P} \cdot \mathbf{n} - \#, \quad \langle \mathbf{F} \rangle = \bar{\mathbf{F}} \tag{4.1}$$

where Div represents divergence in the reference configuration, $\mathbf{P}$ is the first Piola-Kirchhoff stress, $\mathbf{n}$ is the outward unit normal vector, and $\bar{\mathbf{F}}$ is the applied RVE average deformation gradient. Here, $\langle \cdot \rangle$ denotes the volume average of a field computed using the trapezoidal rule. Periodic and anti-periodic boundary conditions are denoted by $\#$ and $-\#$, respectively. The weak form is derived by multiplying the strong form (4.1) with an arbitrary periodic displacement perturbation $\mathbf{w}$:

$$\int_B \mathbf{w} \cdot \text{Div}\,\mathbf{P} \; \mathrm{d}\Omega = 0, \quad \forall\, \mathbf{w} \in \mathrm{L}^2_\# \tag{4.2}$$

in which $\mathrm{L}^2_\#$ denotes a space of periodic functions over B where each vector (tensor) component is square-integrable [91]. Performing integration by parts yields:

$$\int_B \delta\tilde{\mathbf{F}} : \mathbf{P} \; \mathrm{d}\Omega = 0, \quad \forall\, \delta\tilde{\mathbf{F}} \in \mathrm{L}^2_\#, \nabla \times \delta\tilde{\mathbf{F}} = \mathbf{0}. \tag{4.3}$$

Note that $\delta\tilde{\mathbf{F}}$ is the gradient of a virtual displacement field, for example $\delta\tilde{\mathbf{F}} = \nabla\mathbf{w}$, and therefore must be compatible (i.e. its curl vanishes). Also, the virtual work contribution vanishes over the boundary, since the displacement perturbation is periodic and the traction field $\mathbf{P} \cdot \mathbf{n}$ is anti-periodic. In contrast to the FE method, the FFT-based methods usually discretize the deformation gradient $\mathbf{F}$ instead of the displacement $\mathbf{u}$. Specifically, in the Fourier-Galerkin method, the Green operator $\mathbb{G}$ is introduced to project an arbitrary second order tensor field $\delta\mathbf{F}$ into its curl-free components $\delta\tilde{\mathbf{F}}$ [91], thereby relaxing the requirement

for the compatible test function field:

$$\int_B (\mathbb{G} * \delta\mathbf{F}) : \mathbf{P} \ \mathrm{d}\Omega = 0, \quad \forall \delta\mathbf{F} \in \mathrm{L}_\#^2 \tag{4.4a}$$

$$\hat{\mathbb{G}}_{ijkl} = \begin{cases} 0 & \boldsymbol{\xi} = \mathbf{0} \\ \frac{\delta_{ik}\xi_j\xi_l}{\|\boldsymbol{\xi}\|^2} & \boldsymbol{\xi} \neq \mathbf{0} \end{cases} \tag{4.4b}$$

Here, $*$ denotes convolution, a superimposed hat denotes the quantities in Fourier space, and $\boldsymbol{\xi}$ is the frequency vector. Taking advantage of the self-adjoint property of the $\mathbb{G}$ operator, the weak form (4.4a) of equilibrium in the RVE can be expressed for arbitrary (possibly incompatible) test functions $\delta\mathbf{F}$ as follows:

$$\int_B \delta\mathbf{F} : (\mathbb{G} * \mathbf{P}) \ \mathrm{d}\Omega = 0, \quad \forall \delta\mathbf{F} \in \mathrm{L}_\#^2. \tag{4.5}$$

To evaluate the integral in equation (4.5), the RVE B is first discretized into a regular grid of points:

$$x_i = \left(-\frac{1}{2} + \frac{1}{2N_i}, -\frac{1}{2} + \frac{3}{2N_i}, \ldots, \frac{1}{2} - \frac{1}{2N_i} \right) \times L_i, \quad i = 1, 2, 3 \tag{4.6}$$

where x_i is the grid point coordinates, N_i is the total number of grid points, and L_i is the RVE length in the i th direction. In the current research, only odd numbered N_i are considered to avoid the influence of the Nyquist frequency. Then, the trigonometric polynomial shape functions can be defined as

$$\mathbf{F}(\mathbf{x}) = \mathbf{F_k}\varphi_\mathbf{k}(\mathbf{x}), \quad \varphi_\mathbf{k}(\mathbf{x}) = \frac{1}{\prod_{j=1}^3 N_j} \sum_\mathbf{m} \left[\prod_{l=1}^3 \exp 2\pi i \left(\frac{m_l x_l}{L_l} - \frac{k_l m_l}{N_l} \right) \right] \tag{4.7}$$

Here, $\mathbf{m}$ and $\mathbf{k}$ are the truncated frequency vectors. The periodic boundary condition on $\mathbf{F}$ is enforced by the periodicity property of the trigonometric polynomials.

Two integration strategies can be performed after discretizing the $\mathbb{G}$ operator. One utilizes the Plancherel theorem and properties of trigonometric polynomials to analytically evaluate the integrals, leading to the Galerkin approximation (Ga) algorithm. The other utilizes the trapezoidal rule, leading to the Galerkin approximation with numerical

integration (GaNi) algorithm [95]. In this chapter, the GaNi scheme is employed to achieve better numerical efficiency. Evaluating (4.5) by the trapezoidal rule, taking advantage of the Kronecker delta property of the trigonometric polynomials, and considering the arbitrariness of $\delta\mathbf{F}$ leads to the discretized equations:

$$\mathbb{G} * \mathbf{P} = \mathbf{0} \tag{4.8a}$$

$$\mathcal{F}^{-1}\left[\hat{\mathbb{G}} : \mathcal{F}\left(\mathbf{P}\right)\right] = \mathbf{0} \tag{4.8b}$$

where $\mathcal{F}$ and $\mathcal{F}^{-1}$ represent respectively forward and backward Fourier transformation. Since (4.8a) appears similar to the strong form (4.1) satisfied at each grid point, the Fourier-Galerkin method with numerical integration is equivalent to a spectral collocation method.

The nonlinear equation (4.8a) in terms of $\mathbf{F}$ can be solved by the Newton-Raphson method. Since the projection operator $\mathbb{G}$ is independent of the deformation gradient, consistent linearization of equation (4.8a) is possible for an arbitrary Newton iteration (i):

$$\mathbb{G} * \left(\mathbf{P}^{(i)} + \mathbf{A}^{(i)} : \Delta\mathbf{F}^{(i+1)}\right) = \mathbf{0} \tag{4.9a}$$

$$\mathbb{G} * \left(\mathbf{A}^{(i)} : \Delta\mathbf{F}^{(i+1)}\right) = -\mathbb{G} * \mathbf{P}^{(i)}. \tag{4.9b}$$

The conversion to equation (4.9b) utilizes the linearity of the $\mathbb{G}$ operator. Equation (4.9b) can be solved by the Newton-Krylov method with a conjugate gradient solver. The existence and uniqueness of the solution has been proven in [96].

In the original formulation, a hyperelastic material was assumed where $\mathbf{P}$ equals to $\partial W/\partial\mathbf{F}$ and $\mathbf{A}$ equals to $\partial\mathbf{P}/\partial\mathbf{F}$. One contribution of the current work is to derive and implement a general interface between the Fourier-Galerkin method and hypoelastic-plastic materials, in particular a crystal plasticity material model.

4.2.2 Homogenized tangent stiffness

The homogenized tangent stiffness of the RVE problem is essential for treating mixed boundary conditions and for concurrent multiscale modeling within the Newton-Raphson method. In the former case, it is used to update the average deformation gradient $\bar{\mathbf{F}}$ according

to the prescribed average stress $\bar{\mathbf{P}}$. In the latter, it is used to update the macroscopic displacement field [39]. The analytical stiffness evaluation shown below requires only one call to the constitutive subroutine or recall from memory per grid point, as opposed to 6 or 9 constitutive computations per grid point for the finite difference evaluation. This cost savings is greater for more involved constitutive models, such as crystal plasticity. Previously, the homogenized tangent stiffness was computed from either volume average [14] or finite difference [33] methods. Recently, an analytical expression was achieved by utilizing the Lippmann-Schwinger equation [25], but this solution applies to the basic scheme which depends on the reference material. Here, the analytical form of the consistent homogenized tangent stiffness is derived for the Fourier-Galerkin method that is appropriate for highly heterogeneous and nonlinear material.

The homogenized tangent stiffness $\bar{\mathbf{A}}$ is a fourth order tensor defined as

$$\mathrm{d}\,\langle \mathbf{P} \rangle = \bar{\mathbf{A}} : \mathrm{d}\,\langle \mathbf{F} \rangle = \left\langle \frac{\partial \mathbf{P}\,(\mathbf{F})}{\partial \mathbf{F}} : \frac{\partial \mathbf{F}}{\partial \langle \mathbf{F} \rangle} \right\rangle : \mathrm{d}\,\langle \mathbf{F} \rangle. \tag{4.10}$$

In this equation, $\bar{\mathbf{A}}$ is defined as the volume average of the inner-product between local stiffness and local strain perturbations caused by the macroscopic strain $\langle \mathbf{F} \rangle = \bar{\mathbf{F}}$.

For the history dependent material response considered in Section 4.3, the RVE deformation is tracked through a quasistatic time step series. Hence, the first term $\partial \mathbf{P}\,(\mathbf{F})\,/\partial \mathbf{F}$ in (4.10) is the algorithmic consistent tangent $\mathbf{A}$ at each grid point obtained from the material update routine as shown in Section 4.3.2

$$\mathbf{A}\,(\mathbf{F}) = \frac{\partial \mathbf{P}\,(\mathbf{F})}{\partial \mathbf{F}}. \tag{4.11}$$

The second term $\partial \mathbf{F}/\partial \bar{\mathbf{F}}$ can be obtained from the Fourier-Galerkin discrete equation (4.8a) by taking the derivative on both sides:

$$\mathbb{G} * \left(\frac{\partial \mathbf{P}\,(\mathbf{F})}{\partial \mathbf{F}} : \frac{\partial \mathbf{F}}{\partial \bar{\mathbf{F}}} \right) = \mathbf{0}. \tag{4.12}$$

Note that the current RVE deformation gradient can be decomposed into an average part and a perturbation part:

$$\mathbf{F} = \bar{\mathbf{F}} + \tilde{\mathbf{F}}, \quad \left\langle \tilde{\mathbf{F}} \right\rangle = \mathbf{0} \tag{4.13}$$

where the perturbation part $\tilde{\mathbf{F}}$ should be compatible, and its volume average should be zero.

Differentiating equation (4.13) with respect to $\bar{\mathbf{F}}$ leads to an expression relating macroscale and microscale strains:

$$\frac{\partial \mathbf{F}}{\partial \bar{\mathbf{F}}} = \mathbf{I} + \frac{\partial \tilde{\mathbf{F}}}{\partial \bar{\mathbf{F}}}. \tag{4.14}$$

Here, $\mathbf{I}$ is the fourth order identity tensor. Substituting equations (4.11) and (4.14) into equation (4.12) and employing the linearity of the $\mathbb{G}$ operator produces an implicit expression for the second term $\partial \mathbf{F}/\partial \bar{\mathbf{F}}$ representing how a change in macroscale $\bar{\mathbf{F}}$ affects the microscale perturbation $\tilde{\mathbf{F}}$:

$$\mathbb{G} * \left(\mathbf{A} : \frac{\partial \tilde{\mathbf{F}}}{\partial \bar{\mathbf{F}}} \right) = -\mathbb{G} * \mathbf{A}. \tag{4.15}$$

This system of equations for the $81 \times N_1 \times N_2 \times N_3$ unknowns within $\partial \tilde{\mathbf{F}}/\partial \bar{\mathbf{F}}$ has direct analogy with the consistent tangent of the FE^2 approach relating macroscale and microscale displacement degrees of freedom, contained for example in [39]. It can be solved by the conjugate gradient method under the following constraint:

$$\frac{1}{V} \int_B \frac{\partial \tilde{\mathbf{F}}}{\partial \bar{\mathbf{F}}} dV = \mathbf{0}. \tag{4.16}$$

Both the compatibility constraint and (4.16) are ensured by the properties of the $\mathbb{G}$ operator and the conjugate gradient algorithm [95]. This solution along with (4.14) can be substituted into definition (4.10) to yield the homogenized stiffness tensor $\bar{\mathbf{A}}$.

It should be noted that equation (4.15) can be decomposed and implemented as 4 (2D) or 9 (3D) independent equations, as suggested in [25]. In this way, a previously implemented conjugate gradient solver can be reused, and the total amount of required memory can be reduced.

4.2.3 Mixed boundary conditions

The Fourier-Galerkin method is extended to treat mixed boundary conditions as an application of the homogenized tangent stiffness. The loading directions need to be grid-aligned instead of being arbitrary [29].

At the start of each time step, the components of macroscopic strain $\mathbf{F}_{BC}$ and stress $\mathbf{P}_{BC}$ are prescribed as boundary conditions, where individual components are exclusively of strain or stress type. Two Newton loops are required to search for the final solution. The strain iteration searches for the equilibrium stress state according to equation (4.8a) under given homogenized deformation gradient $\bar{\mathbf{F}}$. The stress iteration searches for the homogenized deformation gradient which fulfills the prescribed stress boundary condition $\bar{\mathbf{P}} = \mathbf{P}_{BC}$. Each strain component corresponding to the prescribed $\mathbf{P}_{BC}$ is updated at each stress Newton iteration until the homogenized stress $\bar{\mathbf{P}}$ converges to $\mathbf{P}_{BC}$ with the following convergence criteria satisfied:

$$\frac{\left\| \bar{\mathbf{P}} - \mathbf{P}_{BC} \right\|}{\left\| \bar{\mathbf{P}} \right\|} < \text{tol.} \tag{4.17}$$

An algorithm for this two-loop procedure is presented in Appendix B. To summarize briefly, at the start of a time step, the deformation gradient components corresponding to the prescribed stress components are extrapolated by the current $(\mathbf{P}_{BC,n+1})$ and previous $(\mathbf{P}_{BC,n})$ stress boundary conditions as in equation (4.18a); subsequent iterations proceed using equation (4.18b):

$$\bar{\mathbf{F}}_{ij}^{(1)} = \bar{\mathbf{F}}_n + \left(\frac{\partial \bar{\mathbf{F}}}{\partial \bar{\mathbf{P}}} \right)_{ijkl} (\mathbf{P}_{BC,n+1} - \mathbf{P}_{BC,n})_{kl} \tag{4.18a}$$

$$\bar{\mathbf{F}}_{ij}^{(i+1)} = \bar{\mathbf{F}}_{ij}^{(i)} + \left(\frac{\partial \bar{\mathbf{F}}}{\partial \bar{\mathbf{P}}} \right)_{ijkl} \left(\bar{\mathbf{P}}^{(i)} - \mathbf{P}_{BC,n+1} \right)_{kl} \tag{4.18b}$$

The average compliance tensor $\partial \bar{\mathbf{F}} / \partial \bar{\mathbf{P}}$ is computed as follows. The 9×9 stiffness tensor $\bar{\mathbf{A}}$ is first solved from equations (4.10) and (4.15). Rows corresponding to the essential boundary conditions are set to zero, while the diagonal entries are set to one. Then the compliance tensor is calculated as the inverse of the modified stiffness tensor.

4.2.4 Implementation aspects

In order to combine the Fourier-Galerkin method with general Green-Naghdi rate based hypoelastic-plastic constitutive models, a highly-efficient program is developed and programmed in FORTRAN to solve large-scale, 3-D solid models with periodic boundary conditions. The discrete FFT from Intel Math Kernel Library is utilized in the current program. Also, the projection operator $\mathbb{G}$ is organized such that the zero frequency is in the middle of the array. Therefore, "fftshift" is performed by multiplying the Fourier basis function to be consistent with the discrete FFT algorithm. All quantities corresponding to the same tensor component are aligned continuously in the memory to improve the cache efficiency. The deformation field is recovered by least squares projection via Lagrangian finite element formulations, assuming that the deformation gradient in each element is constant.

4.3 Hypoelastic type crystal plasticity model

A hypoelastic crystal plasticity framework utilizing the Green-Naghdi objective stress rate was developed for the finite element method in [57], accounting for the evolution of crystal lattice rotation. Extensions to multi-hardening variables for unequal slip system resistance and to nonlocal computation of geometrically necessary dislocations were performed in [50] and [86], respectively. Section 4.3.1 summarizes the general kinematic equations of this CP framework. However, this framework has currently been implemented in WARP3D with an inconsistent material tangent stiffness that lacks contributions of rotation between the reference and current configuration. Therefore, in Section 4.3.2, we propose a general interface connecting the FFT-based method and objective rate constitutive models. We derive the direct pull back of the local tangent stiffness from the unrotated configuration to the reference configuration to ensure accelerated convergence when inserted into the Fourier-Galerkin method (equation (4.9b)).

4.3.1 Kinematic equations

Within a finitely deforming body described by the map $\phi\left(\mathbf{X}, t\right)$ for a collection of material points $\mathbf{X}$ at time t, the classical multiplicative decomposition of the deformation gradient yields

$$\mathbf{F} = \mathbf{F}^e \mathbf{F}^p \tag{4.19}$$

where $\mathbf{F} = \partial\phi/\partial\mathbf{X}$ is total deformation gradient and $\mathbf{F}^e$, $\mathbf{F}^p$ represent correspondingly the elastic part and plastic part. The velocity gradient tensor $\mathbf{L}$ is usually decomposed into the symmetric part $\mathbf{D}$ and skew part $\mathbf{W}$:

$$\mathbf{L} = \dot{\mathbf{F}}\mathbf{F}^{-1} = \mathbf{D} + \mathbf{W} \tag{4.20}$$

For crystal plasticity (CP) modeling, it is commonly assumed that the plastic velocity gradient $\tilde{\mathbf{l}}^p$ in the lattice frame can be decomposed into the tensorial summation of the resolved shear strain rate $\dot{\gamma}^{(s)}$ on each slip system:

$$\tilde{\mathbf{l}}^p = \sum_{s=1}^{n_{slip}} \dot{\gamma}^{(s)} \left(\tilde{\mathbf{b}}^{(s)} \otimes \tilde{\mathbf{n}}^{(s)} \right) \tag{4.21}$$

The orientation of slip system (s) is represented by the normalized Burgers vector $\tilde{\mathbf{b}}^{(s)}$ and the slip plane normal $\tilde{\mathbf{n}}^{(s)}$. The relation between $\tilde{\mathbf{l}}^p$ and the plastic velocity gradient $\mathbf{l}^p$ in the corotational, intermediate frame is a transformation using the plastic rotation tensor from the polar decomposition $\mathbf{F}^p = \mathbf{R}^p\mathbf{U}^p$. Quantities $\mathbf{d}^p$ and $\mathbf{w}^p$ in the intermediate configuration, relevant to the Green-Naghdi rate, are defined as the symmetric and skew part of $\mathbf{l}^p$:

$$\mathbf{d}^p = \sum_{s=1}^{n_{slip}} \dot{\gamma}^{(s)} \mathbf{R}^{pT} \tilde{\mathbf{m}}^{(s)} \mathbf{R}^p, \quad \tilde{\mathbf{m}}^{(s)} = \text{sym}\left(\tilde{\mathbf{b}}^{(s)} \otimes \tilde{\mathbf{n}}^{(s)} \right) \tag{4.22a}$$

$$\mathbf{w}^p = \sum_{s=1}^{n_{slip}} \dot{\gamma}^{(s)} \mathbf{R}^{pT} \tilde{\mathbf{q}}^{(s)} \mathbf{R}^p, \quad \tilde{\mathbf{q}}^{(s)} = \text{skew}\left(\tilde{\mathbf{b}}^{(s)} \otimes \tilde{\mathbf{n}}^{(s)} \right) \tag{4.22b}$$

where $\tilde{\mathbf{m}}^{(s)}$ and $\tilde{\mathbf{q}}^{(s)}$ represent the symmetric and skew parts of the slip system tensor. According to the derivations in [57] assuming small elastic strains, the constitutive equation

66

is specified by the Green-Naghdi rate $\check{\boldsymbol{\sigma}}$ of the Cauchy stress $\boldsymbol{\sigma}$, as

$$\check{\boldsymbol{\sigma}} = \mathbf{C} : \left(\mathbf{D} - \mathbf{R}\mathbf{d}^p\mathbf{R}^T\right) - \mathbf{R}\mathbf{w}^p\mathbf{R}^T\boldsymbol{\sigma} + \boldsymbol{\sigma}\mathbf{R}\mathbf{w}^p\mathbf{R}^T = \dot{\boldsymbol{\sigma}} + \boldsymbol{\sigma}\boldsymbol{\Omega} - \boldsymbol{\Omega}\boldsymbol{\sigma} \qquad (4.23)$$

where $\mathbf{F} = \mathbf{R}\mathbf{U}$ and $\boldsymbol{\Omega} = \dot{\mathbf{R}}\mathbf{R}^T$. In this equation, the lattice rotation caused by the plastic strain gradient is explicitly considered, making it suitable for large strain problems. The constitutive relation simplifies greatly when stated in the corotational frame

$$\dot{\mathbf{t}} = \mathbf{C}_0 : (\mathbf{d} - \mathbf{d}^p) + \mathbf{R}\mathbf{w}^p\mathbf{R}^T\mathbf{t} - \mathbf{t}\mathbf{R}\mathbf{w}^p\mathbf{R}^T \qquad (4.24)$$

where $\mathbf{t}$ is the unrotated Cauchy stress, $\mathbf{d} = \mathbf{R}^T\mathbf{D}\mathbf{R}$ is the strain rate tensor in the corotational frame, and $\mathbf{C}_0$ is the tensor of elastic material moduli in the corotational frame.

In order to avoid tying the derivations to a specific choice of a slip system hardening model, the CP constitutive relation for plastic slip and hardening evolution can be expressed in the general form:

$$\dot{\gamma}^{(s)} = \dot{\gamma}^{(s)}\left(\mathbf{t}, \{\boldsymbol{\xi}\}\right), \quad \dot{\boldsymbol{\xi}} = \dot{\boldsymbol{\xi}}\left(\mathbf{t}, \boldsymbol{\xi}\right) \qquad (4.25)$$

where $\boldsymbol{\xi} = \{\xi^{(1)}, \xi^{(2)}, \ldots, \xi^{(n)}\}$ is a set of internal hardening variables. The typical dependence on the generic form of the local Jacobian matrices, for example $\partial\mathbf{t}/\partial\mathbf{d}$, can be found in previous work [57, 50]. Significantly, this generalized stress update algorithm clearly isolates the kinematics from the model dependent terms such that a variety of constitutive models, for example mechanical threshold model [38] and dislocation density based model [49], are easily accommodated.

4.3.2 Consistent tangent stiffness in reference configuration

The material model's objective time integration is carried out on the unrotated configuration to be independent of superposed rigid body motions. The geometric transformation of material stiffness from unrotated configuration to reference configuration for the Green-Naghdi objective rate was approximately computed previously in [26]. Such approximation usually leads to slower convergence rate and increase in computation time [18]. Recently, consistent linearization of Jaumann rate based elasto-plastic material model was derived [75].

In this section, the Green-Naghdi rate based material stiffness is consistently transformed into the reference configuration. Note that such exact geometric transformation yields a non-symmetric tangent stiffness, which has limited influence on FFT-based methods since the global stiffness matrix is never explicitly assembled or factorized.

Herein, we employ the time integration scheme from [50] using the midpoint rule to evolve the material state from a generic time step t_n to $t_{n+1} = t_n + \Delta t$. The target of this section is to pull back the local tangent from the unrotated configuration to the reference configuration

$$\frac{\partial \mathbf{t}_{n+1}}{\partial \Delta \mathbf{d}_{n+\frac{1}{2}}} \Rightarrow \frac{\partial \mathbf{P}_{n+1}}{\partial \mathbf{F}_{n+1}} \tag{4.26}$$

where the increment notation $\Delta(\cdot) = (\cdot)\Delta t$ is introduced. In this equation, the strain rate $\mathbf{d}_{n+\frac{1}{2}}$ is defined in the unrotated configuration corresponding to $\mathbf{D}_{n+\frac{1}{2}}$ at an intermediate time step, given as follows:

$$\Delta \mathbf{D}_{n+\frac{1}{2}} \equiv \mathrm{sym}\left[(\mathbf{F}_{n+1} - \mathbf{F}_n)\mathbf{F}_{n+\frac{1}{2}}^{-1}\right], \quad \Delta \mathbf{d}_{n+\frac{1}{2}} = \mathbf{R}_{n+\frac{1}{2}}^T \Delta \mathbf{D}_{n+\frac{1}{2}} \mathbf{R}_{n+\frac{1}{2}}. \tag{4.27}$$

Here, $\mathbf{F}_{n+\frac{1}{2}}$ is defined by the midpoint rule

$$\mathbf{F}_{n+\frac{1}{2}} = \frac{1}{2}\left(\mathbf{F}_{n+1} + \mathbf{F}_n\right) = \mathbf{R}_{n+\frac{1}{2}}\mathbf{U}_{n+\frac{1}{2}}. \tag{4.28}$$

The relation between $\mathbf{t}_{n+1}$ and $\mathbf{P}_{n+1}$ reads

$$\mathbf{P}_{n+1} = J_{n+1}\mathbf{R}_{n+1}\mathbf{t}_{n+1}\mathbf{R}_{n+1}^T\mathbf{F}_{n+1}^{-T}. \tag{4.29}$$

Then, the tangent stiffness in both configurations can be defined in terms of total differentials of the respective algorithmic equations as

$$\mathrm{d}\mathbf{P}_{n+1} = \mathbf{A} : \mathrm{d}\mathbf{F}_{n+1}, \quad \mathrm{d}\mathbf{t}_{n+1} = \mathbf{c} : \mathrm{d}\Delta\mathbf{d}_{n+\frac{1}{2}}. \tag{4.30}$$

The unrotated configuration moduli $\mathbf{c}$ emerges from the total derivative of the algorithmic counterpart of (4.24) and has been presented in [57]. Then, the relationship between the

algorithmic moduli $\mathbf{A}$ and $\mathbf{c}$ is obtained by directly differentiating (4.29). This involved derivation is presented in Appendix A.

4.4   Numerical results and discussion

In this section, the Voce model is used to illustrate the accuracy and efficiency of the current FFT-based method compared with the FE method and a reference FFT implementation. The Voce model typically adopts a power-law relation without temperature effects. All slip systems are assumed to have isotropic resistance with equal saturation stress. The relation between resolved shear strain rate $\dot{\gamma}^{(s)}$ and resolved shear stress $\tau^{(s)}$ in the Voce model reads

$$\dot{\gamma}^{(s)} = \frac{\dot{\gamma}_0}{\tilde{\tau}} \left| \frac{\tau^{(s)}}{\tilde{\tau}} \right|^{n-1} \tau^{(s)}. \tag{4.31}$$

Here, (s) denotes the slip system, $\dot{\gamma}_0$ is the reference slip rate, and $\tilde{\tau}$ replaces $\boldsymbol{\xi}$ in equation (4.25) as the hardening variable. The slip system resistance $\tilde{\tau}$ is decomposed into the intrinsic (yield) resistance τ_y and the extrinsic (hardening) resistance τ_w

$$\tilde{\tau} = \tau_y + \tau_w. \tag{4.32}$$

The extrinsic resistance τ_w evolves as a function of the slip system activity $\dot{\gamma}^{(s)}$

$$\dot{\tau}_w = \theta_0 \left(1 - \frac{\tau_w}{\tau_v} \right)^m \sum_{s=1}^{n_{slip}} \left| \dot{\gamma}^{(s)} \right| \tag{4.33}$$

where θ_0 is the initial hardening rate, and the work hardening saturation strength τ_v sets the upper bound of τ_w. The exponents m and n are separate parameters.

All numerical tests herein are performed on a cluster with compute nodes running CentOS 6.7 having 20 Intel Xeon Cores and 512 GB memory. The finite element code WARP3D [12], reference DAMASK FFT-based method [14], and proposed Fourier-Galerkin method are each written in FORTRAN and are compiled with Intel FORTRAN and Math Kernel Library (MKL) at the highest permissible optimization level. Jobs are run on a single node with the number of threads indicated in the problem description. The CP material subroutines in the

FE and Fourier-Galerkin codes are exactly identical. These similarities provide a platform for fair comparison of the methods.

However, certain differences in implementation also influence the methods' relative efficiency and are summarized below. First, the finite elements used in this investigation are 8-node B-bar elements with 8-point integration, while in the FFT-based method the Galerkin approximation with numerical integration (GaNi) is adopted with one integration point per grid point. Therefore, the stress update in the FE method costs 8 times as much as the FFT-based method when the total number of elements and grid points are the same. This difference is not important when multiple threads are used for stress update, see discussions below. Incidentally, since $\mathbf{u}$ and $\mathbf{F}$ are the primary unknown field for the FE and FFT-based methods, respectively, the latter method has 3 times the number of global degrees of freedom. Second, periodic boundary conditions (PBC) are used in the FE method to quantitatively compare with the FFT-based method results. These conditions are achieved by means of eliminating the dependent displacements in the equilibrium equations, which avoids increasing the total number of equations and computational cost. Third, in the FE method, the Pardiso direct solver is used, and the termination criteria of each Newton step is when the global iterated residual norm $\|\mathbf{R}_k\|$ is less than $\eta\|\mathbf{R}_0\|$ for a specified tolerance η. In the FFT-based method, the conjugate gradient (CG) solver (called DCG) from the MKL library is used, and the strain iteration loop is stopped when $\|\delta\mathbf{F}_k\| \leq \eta\|\Delta\mathbf{F}\|$. Lastly, odd numbers of grid points or elements are used for each simulation to avoid the influence of the Nyquist frequency. This approach slightly increases the computation cost of DFT but leads to strain compatibility and stress equilibrium simultaneously [8].

In the following sections, the results from the FFT-based method are first verified against the FE method. Key emphasis is placed on the local stress distribution, the orientation distribution and the algorithmic convergence rate. After that, the inexact Newton method is applied to the FFT-based method to further improve the efficiency, and the relative influence of CG tolerance and Newton tolerance are discussed. Lastly, the computational cost of the FFT-based method is compared with the FE method and a reference FFT-based method.
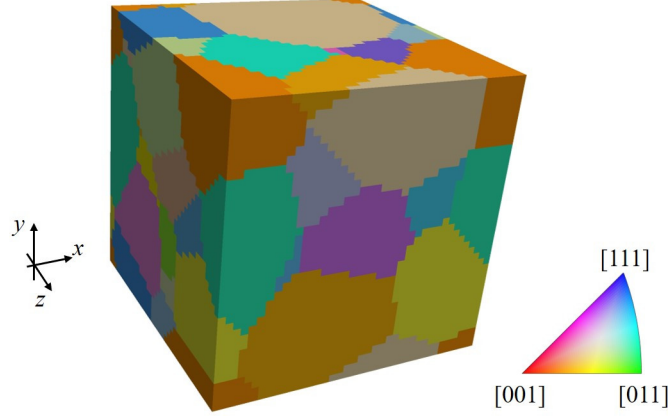
Figure 4.1: Spatial discretization of periodic RVE with mesh/grid resolution of $39 \times 39 \times 39$. Each color represents a randomly chosen initial orientation considering FCC crystal symmetry.

Table 4.1: Material parameters based on those from [14]

	C_{11}	C_{12}	C_{44}	$\dot{\gamma}_0$	τ_y	τ_v	θ_0	n	m
Unit	GPa	GPa	GPa	ms^{-1}	MPa	MPa	MPa	-	-
Value	106.75	60.41	28.34	1.0	31	63	75	20	2.25

4.4.1 Verification and validation

To verify the FFT-based method against the FE method, a periodic representative volume element (RVE) with 30 randomly oriented grains is generated by Neper [71]. An FCC crystal structure with 12 slip systems is considered here along with the material parameters in Table 4.1 [14]. The RVE is discretized into $39 \times 39 \times 39$ voxels, as shown in Figure 4.1. Uniaxial tension is applied in a series of 1000 equal increments of strain to reach the following total values of strain and stress:

$$\mathbf{F} = \begin{bmatrix} 1.5 & 0.0 & 0.0 \\ 0.0 & * & 0.0 \\ 0.0 & 0.0 & * \end{bmatrix}, \quad \mathbf{P} = \begin{bmatrix} * & * & * \\ * & 0.0 & * \\ * & * & 0.0 \end{bmatrix}. \tag{4.34}$$

Various results from the FE and FFT-based methods are compared in Figure 4.2 to Figure 4.4. Since both numerical methods are Galerkin-based and are solving the same boundary value problem (constitutive relation, geometry, loading), all computed differences can be attributed to differences in the approximating shape functions and mesh resolution.

71
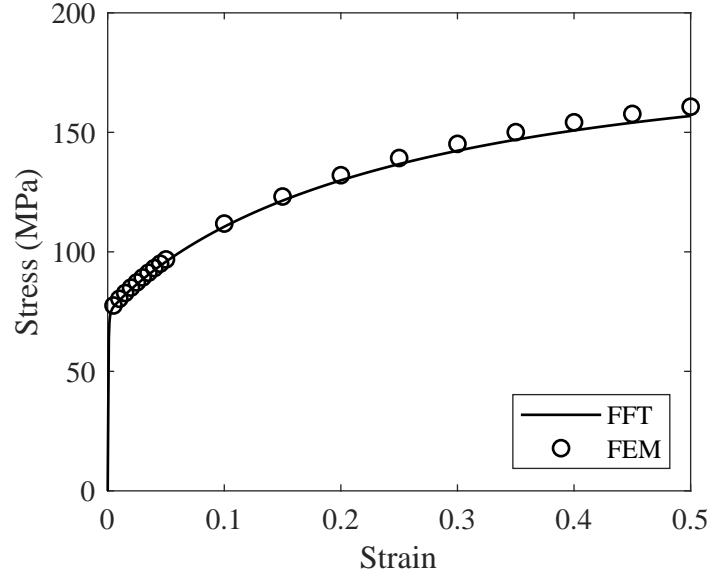
Figure 4.2: Homogenized stress-strain relation from FFT-based method and FE method

From the homogenized stress-strain curve in Figure 4.2, the homogenized loading stress (σ_{xx}) of the FFT-based method appears slightly lower than the FE method. A similar trend is also observed in [14], but our difference is much less obvious. Crystal orientation and local stress distributions are presented in Figure 4.3. The grains experience similar fragmentation and rotation in each case. Stress concentrations at triple junctions of grain boundaries are captured in both methods. Even though the general distributions are similar, certain differences regarding local perturbations still exist, for example in the longitude stress at the upper right edge. Also, the transverse stress in the FE method seems to be more affected by the voxelated, non-smooth grain boundary. Similar trends are also found in Figure 4.4 by examining the von Mises stress distribution along the RVE diagonal. The stress field within the grains are similar for both methods. Larger discrepancy is observed at the grain boundaries, where material heterogeneity and therefore stress discontinuity exists. Such stress perturbations at grain boundaries may cause stress concentrations and lead to failure hot spots [51]. Also, at position 0.8, stress oscillations appear in the FFT results which are attributed to the Gibbs phenomena. Both methods are expected to converge to a similar computed response as the grid resolution increases and the grain boundary smoothness increases.
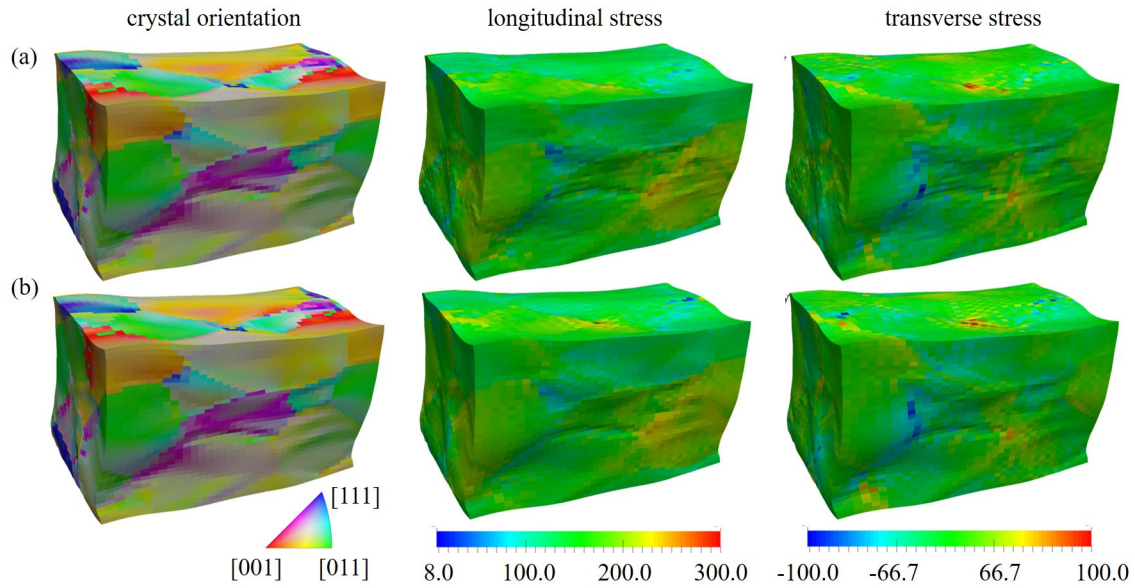
Figure 4.3: Local stress distribution (MPa) when homogenized strain $\bar{F}_{xx} = 1.5$. (a) FFT-based method; (b) FE method.
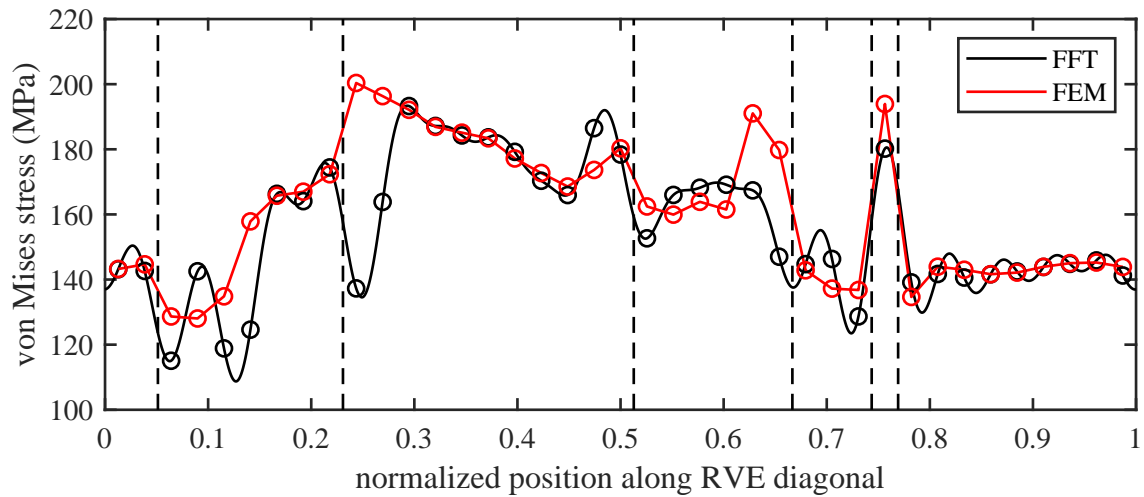
Figure 4.4: Von Mises stress distribution along RVE diagonal when homogenized strain $\bar{F}_{xx} = 1.5$. FE stress field is recovered by piecewise linear interpolation; FFT stress field is recovered by trigonometric polynomial interpolation.
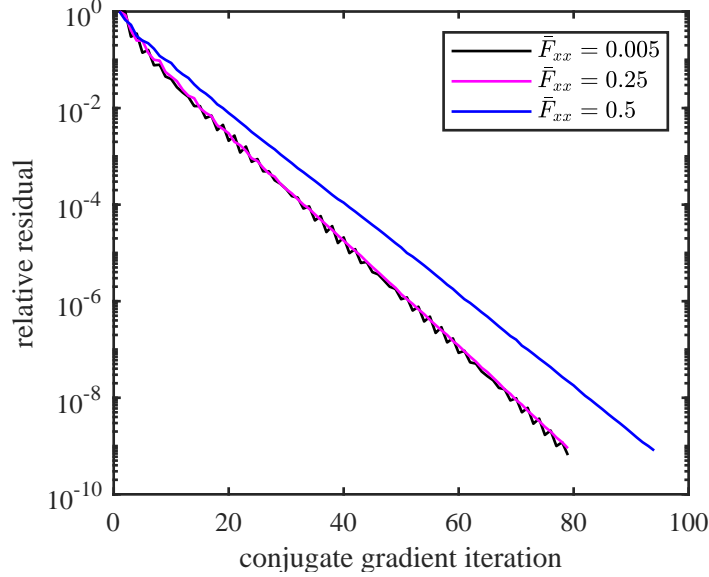
Figure 4.5: Convergence progress of conjugate gradient solver.

Convergence progress of the CG solver in the FFT-based simulation is presented on a logarithmic scale in Figure 4.5. Non-monotonic convergence of the residual is observed when $\bar{F}_{xx}$ equals to 1.005. Such oscillations have been observed for hyperelastic materials in [65] and may be caused by the derivative calculation in the Fourier space. Large phase contrast can also trigger osciallations [96] and can be reduced through the Galerkin approximation (Ga) scheme when two-grid integration is used [61]. Presently, the transition between elastic and plastic response in certain grains manifests as a large phase contrast when $\bar{F}_{xx}$ equals to 1.005, leading to such oscillations. When the deformation gradient is large enough ($\bar{F}_{xx} = 1.25$), all the grains in the RVE deform plastically, and the phase contrast is less obvious. In this case, oscillations are only observed in the first several iterations. We remark that the CG convergence rate decreases as the deformation gradient further increases into the finite strain region. This may be caused by the geometric stiffness induced phase contrast increase.

The evolution of the residual norm from the Newton algorithm is shown in Figure 4.6 (a) and (b) respectively for the strain iteration and the stress iteration. The residual norm convergence rates reflect the accurate linearization of the local material tangent $\mathbf{A}$ and the global homogenized tangent $\bar{\mathbf{A}}$. Both of the iteration loops converge at a rate between super-linear and quadratic. The global applied strain $\bar{\mathbf{F}}$ appears to have a limited influence on the convergence behavior. A better initial guess, such as extrapolating the

74
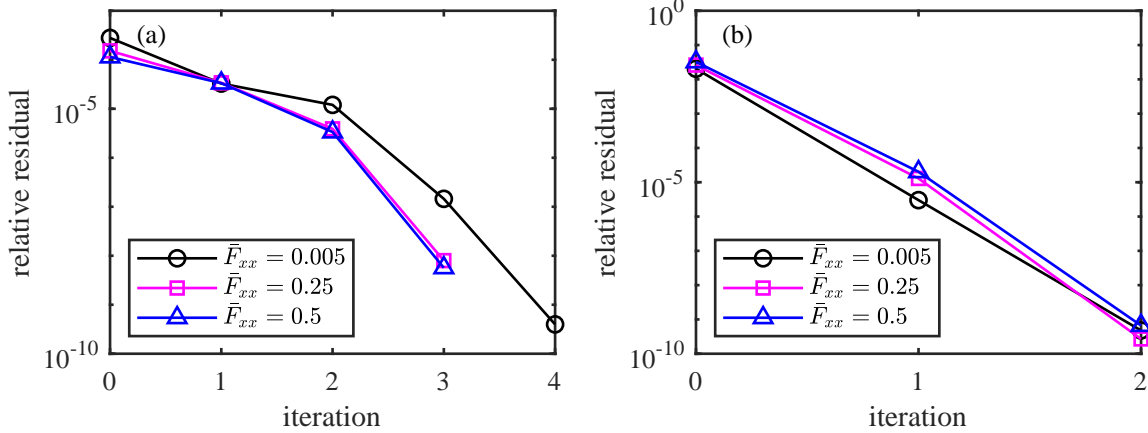
Figure 4.6: Convergence progress of Newton iteration. (a) Strain iteration; (b) Stress iteration.

microscale/polarization field at the grid points to the next load step, could also reduce the initial error and number of Newton iterations.

4.4.2 Inexact Newton method and phase contrast study

In the previous simulation, a constant CG tolerance (equal to 1.0×10^{-8}) is applied during every Newton iteration. Note that the deformation gradient field remains compatible during every CG iteration, so that the global Newton nonlinear solver can search for a stress field corresponding to the compatible strain field. Since the earliest Newton updates of a new step are often imprecise, it is usually not necessary to solve the linear system (4.9b) accurately. In this section, the inexact Newton method with evolving CG tolerance is applied to the FFT-based method to further improve its numerical efficiency.

The evolving CG tolerance is determined according to previous experience of the convergence rate in Figure 4.5 and 4.6. The initial CG tolerance is set as $\eta_{CG} = 1.0 \times 10^{-4}$. The evolving CG tolerance is set as $\eta_{CG} = \|\mathbf{R}_{NR}\|^2/10$ to ensure quadratic convergence rate. The lower bound of η_{CG} is set as 1.0×10^{-8}, which is the constant CG solver tolerance in the previous simulation and also for the reference case labeled exact Newton method in this section.

A cubic RVE ($39 \times 39 \times 39$) with a spherical inclusion (with a diameter across 22 grid points) is constructed to investigate the influence of evolving CG tolerance on the method's
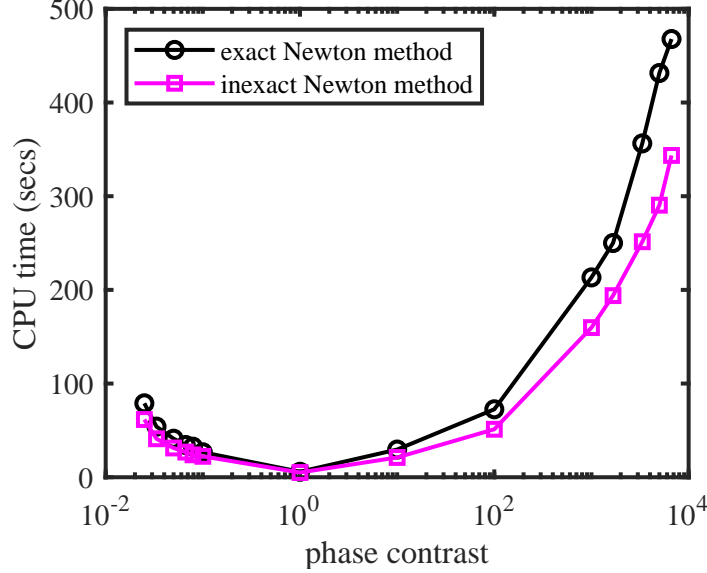
Figure 4.7: Computational cost of exact Newton method and inexact Newton method for varying elastic phase contrasts.

numerical behavior. The volume fraction of the spherical inclusion is about 11.3 %. For simplicity, both the matrix and the inclusion are isotropic hypoelastic materials. The Young's modulus of the matrix is $E = 12000.0$ MPa, and the modulus of the inclusion is set to ρE where ρ is the phase contrast. Poisson's ratio is 0.3 for both materials. Constant-volume tension boundary conditions are applied to a level of strain equals to 0.1.

The effect of the inexact Newton method on computational efficiency is shown in Figure 4.7 with the phase contrast ρ ranging from 2.5×10^{-2} to 6.7×10^3. A square root relationship is observed between the CPU time and the phase contrast for both exact Newton method and inexact Newton method, consistent with the theoretical analysis in [96]. The total CPU time reduces by about 25% between the exact and inexact cases. Such improved efficiency is more obvious for the cases with greater contrast ratio ρ, where more CG and Newton iterations are required. Therefore, the inexact Newton method is beneficial for crystal plasticity problems, where strong heterogeneity can exist between grains of different orientation.

To further investigate the influence of evolving CG tolerance on the global Newton iteration, Figure 4.8 presents the residual norm history and required CG iterations for two extreme cases of phase contrast corresponding to $\rho = 2.5 \times 10^{-2}$ and $\rho = 6.7 \times 10^3$, respectively. The exact CG and inexact CG curves in Figure 4.8 (a) and (c) indicate the value

of the CG residual at the completion of the CG algorithm for the associated Newton iteration on the horizontal axis. Note that the exact CG case has an essentially constant level for all iterations while the inexact CG has larger values at earlier Newton iterations. Meanwhile, the exact NR and inexact NR curves indicate the residual norm history of the strain Newton iteration loop. For the $\rho = 2.5 \times 10^{-2}$ case, the relaxed CG tolerance has no influence on the global Newton iterations. While for the $\rho = 6.7 \times 10^3$ case the inexact Newton method converges somewhat more slowly than the exact Newton method, the prescribed tolerance is still reached within 3 iterations. Both cases indicate that an inexact linear solution has minimal effect during the first iteration.

The benefit of the relaxed CG tolerance is shown in Figure 4.8 (b) and (d), where the number of CG iterations (which require one matrix multiplication and two DFT applications) is decreased by a factor of two to four at the earliest Newton iteration. This reduction is responsible for the lower CPU time in Figure 4.7. For this hypoelastic material example, the global Newton residual is only slightly influenced by the relaxed CG tolerance, and additional balancing of the computational cost between the CG solver and Newton solver could be pursued. Note that the number of material stress and state updates is directly proportional to the number of Newton iterations, so that this balance must be more carefully evaluated, e.g. for the crystal plasticity case in Section 4.4.3.

4.4.3 Computational effectiveness

The major advantage of FFT-based methods over the FE method is that the former avoids the stiffness matrix factorization, which is costly for large scale problems. Also, the integration points coincide with the grid points, making it convenient for implementation. On the other hand, the stress update process for more involved material models, for example crystal plasticity model, can be a significant fraction of the overall execution time. Therefore, we quantitatively analyze the accuracy and efficiency of both types of methods as the total number of grid points increases.

The benchmark problem for this section is an RVE composed of $3 \times 3 \times 3$ grains with randomly distributed orientations and cubical shape in order to avoid the influence of voxelated grain boundaries as the mesh resolution increases. Constant-volume tension
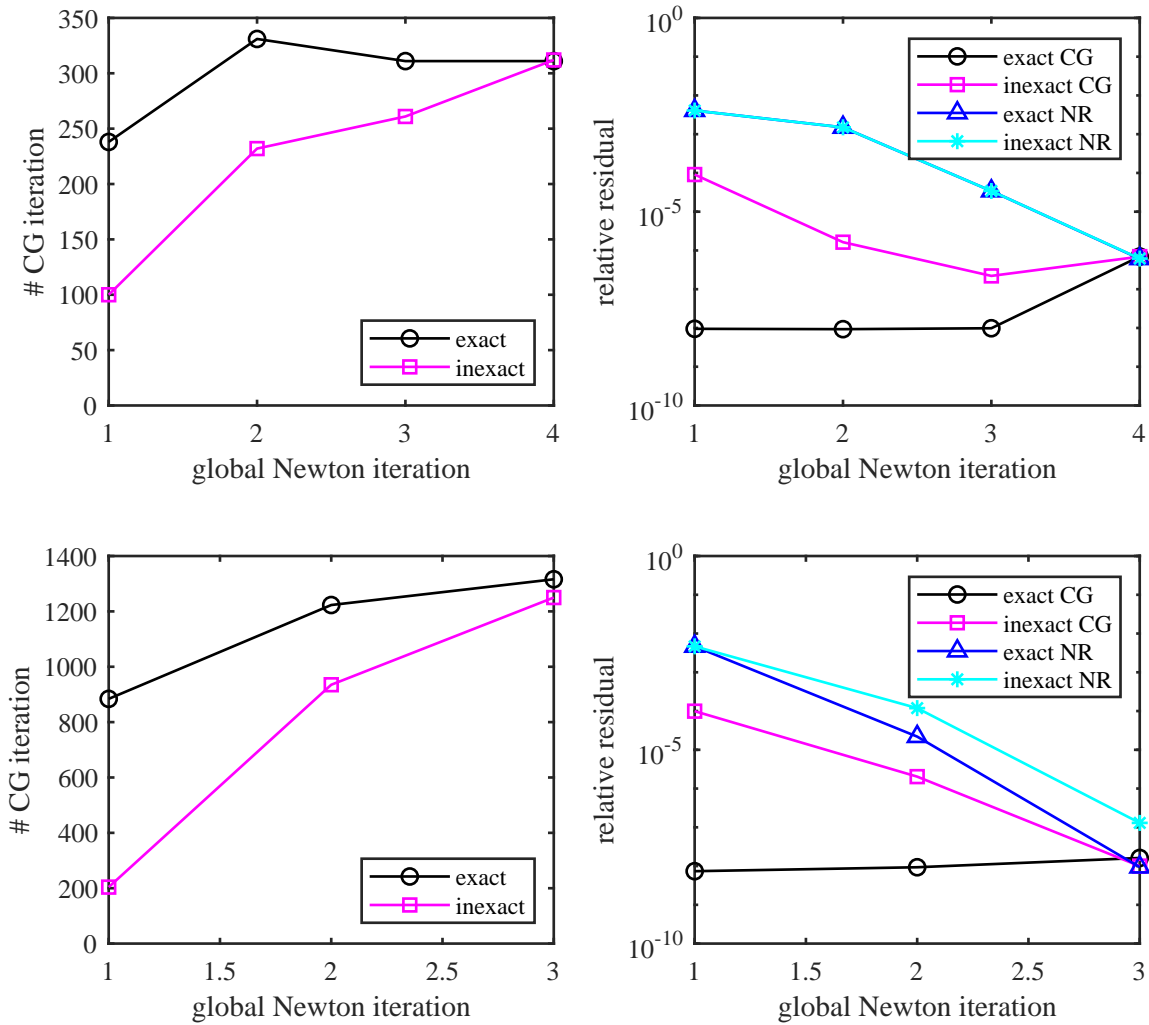
Figure 4.8: Influence of CG tolerance on convergence progress: (a) residual norm history, phase contrast $\rho = 2.5 \times 10^{-2}$; (b) conjugate gradient iterations, phase contrast $\rho = 2.5 \times 10^{-2}$; (c) residual norm history, phase contrast $\rho = 6.7 \times 10^{3}$; (d) conjugate gradient iterations, phase contrast $\rho = 6.7 \times 10^{3}$.

loading is employed, with $F_{xx} = 1.1$ and $F_{yy} = F_{zz} = \sqrt{1/F_{xx}}$. The Voce material parameters are retained from Table 4.1. Five mesh resolutions are tested: $39 \times 39 \times 39$, $57 \times 57 \times 57$, $69 \times 69 \times 69$, $87 \times 87 \times 87$, $99 \times 99 \times 99$. All simulations are performed with 9 computing threads. Only the first three resolutions are tested for the FE case due to the computational time.

Comparison with finite element (direct solver)

First, the influence of mesh resolution on the homogenized stress-strain curve is shown in Figure 4.9. The mesh resolution does not affect the homogenized stress-strain curve, and the difference between the FFT-based method and the FE method is negligible. This observation is contrary to the conclusion in [14], where an FFT-based method converges to the exact solution at relatively low resolution and the FE method gradually approaches to the FFT solution. In their investigation, each grain contains approximately 82, 650, and 5000 elements for FE method at different mesh resolutions. In the current investigation, each grain contains approximately 2200 and 6900 elements for the first two mesh resolutions. Also, the planar grain boundaries are accurately captured for each mesh resolution, as opposed to Voronoi tessellations in [14] where the inclined grain boundaries are approximated by voxels in a stair-step pattern with the size decreasing upon mesh refinement. Therefore, our results suggest that approximately 2200 elements per grain is a large enough resolution to capture the homogenized stress-strain curve for both the FFT-based method and the FE method for cubic shaped grains.

The influence of mesh resolution on the computational cost is presented in Figure 4.10. Figure 4.10 (a) and (b) present the CPU time for the FFT-based method and the FE method, respectively. Generally, the FFT-based method is much more efficient than the FE method. The CG solver scalability (including discrete Fourier transform) is about linear, while the factorization scalability is about N^3. The outcome is that the FE method requires about 10 times more runtime than the FFT-based method on the coarse mesh with a disparity that increases for finer meshes. In fact, the finest FFT simulation finishes in almost less time than the coarsest FE simulation. In both cases, the CPU time for the stress update is almost linear with respect to the total number of elements. The FE method costs about
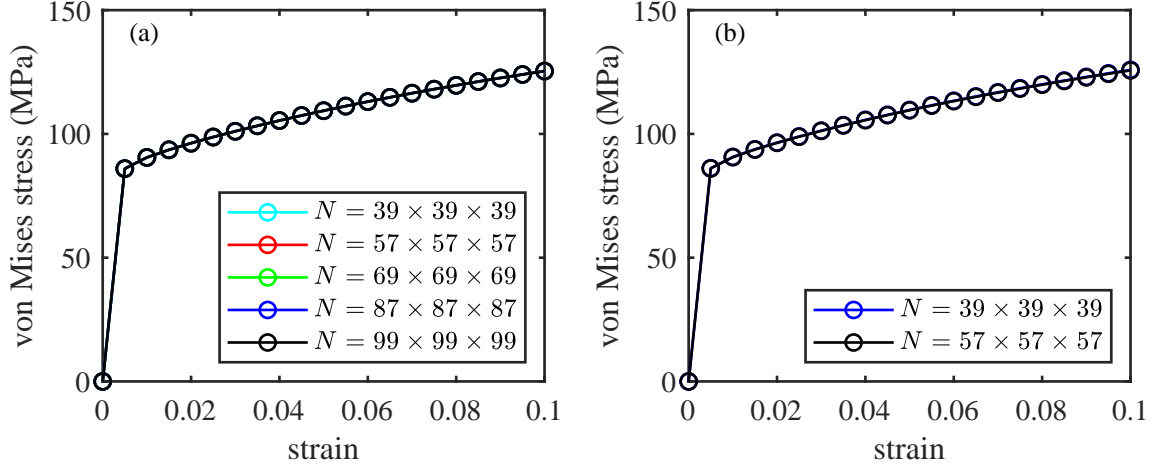
Figure 4.9: Influence of mesh resolution on homogenized stress evolution. (a) FFT-based method; (b) FE method.
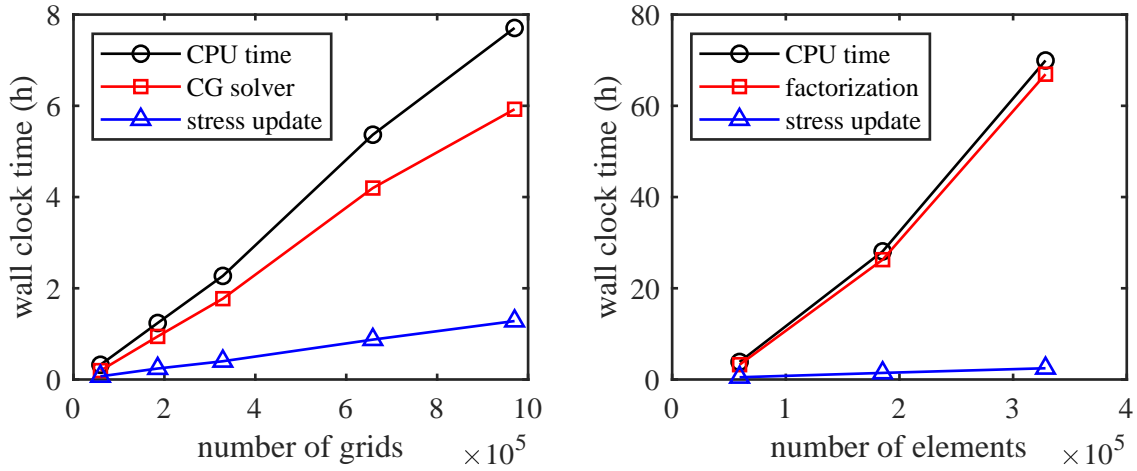
Figure 4.10: Relationship between computation cost and total number of grid points. (a) FFT-based method; (b) FE method.

8 times more time for the stress update, since one finite element has 8 integration points. Such a difference is not significant when multiple threads are used for the stress update and when the linear solver becomes the most time consuming part.

Comparison with other crystal plasticity FFT implementation

In this section, the Fourier-Galerkin method is compared with the Düsseldorf Advanced Material Simulation Kit (DAMASK), a widely used FFT-based implementation for crystal

plasticity modeling at finite strains. Stress equilibrium is used as the convergence criteria:

$$\frac{\|\text{Div } \mathbf{P}\|}{\|\bar{\mathbf{P}}\|} \leq \text{tol.} \tag{4.35}$$

This convergence criteria is also used in the Fourier-Galerkin method to enable an exact comparison. The suggested relative tolerance 5.0×10^{-4} [79] is used in this section. In DAMASK, the nonlinear GMRES solver from PETSc is utilized to solve the Lippman-Schwinger equation. The convergence behavior depends on the choice of reference material, which is updated at every Newton iteration.

The example RVE from the FE method comparison is adopted herein, and the loading history is maintained. Figure 4.11 compares the Cauchy stress distribution between the Fourier-Galerkin method and DAMASK. The distribution of σ_{xx} stress in the loading direction is generally similar, but certain differences exist. For example, some stress oscillations are more obvious in the Fourier-Galerkin method, while the peak stresses at boundaries are generally higher in DAMASK. Such differences are entirely a consequence of the kinematics and objective stress rate differences of the two formulations. The former employs the Green-Naghdi rate while the latter effectively employs the Truesdell-Noll rate, and the updates of the lattice orientations at finite strains probably differ. Otherwise, both formulation effectively utilize trigonometric polynomial basis functions, the Voce material model and parameters, and the same mesh resolution and loading history, and both are solving the equilibrium governing equation by trapezoidal numerical integration. This equivalence is confirmed by solving an RVE model composed of hyperelastic Saint Venant Kirchhoff material in each phase. The grid point results between simulations using DAMASK and the hyperelastic Fourier-Galerkin code [7] agree up to machine precision times the convergence tolerance. For brevity, this comparison is not shown here.

The total computational cost in wall clock time versus the number of grid points is shown in Figure 4.12; both simulations are performed on an Intel Xeon E5-2630 processor with 9 computing threads. It is observed that the total CPU time increases almost linearly for both the Fourier-Galerkin method and DAMASK. In general, the total CPU time of DAMASK is about 5 times larger than the Fourier-Galerkin method regardless of the total number of grid
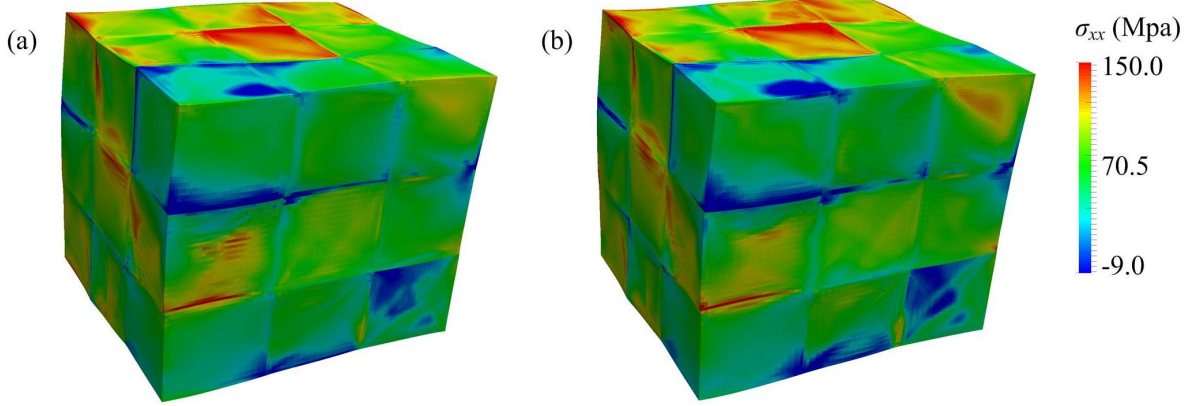
Figure 4.11: Tensile stress (σ_{xx}) distribution when $F_{xx} = 1.1$ under constant-volume tension boundary condition (det $\mathbf{F} = 1$) on $99 \times 99 \times 99$ grids. (a) Fourier-Galerkin method; (b) DAMASK.

points. Several algorithmic and implementational differences between these two codes can explain this cost difference. We believe the primary contribution factor is that the nonlinear GMRES solver adopted in DAMASK generally requires more constitutive updates as well as more memory to store the orthogonal Krylov subspace vectors. Therefore, it is less efficient for more involved crystal plasticity models. This point is motivated by Figure 4.13 below. We consider all other differences to be secondary. Firstly, the theoretical basis of both codes is identical up to CP kinematics and other aspects as mentioned in the preceding paragraph. Secondly, the projection operator in DAMASK depends on the reference material, which is updated by computations in each global iteration. Thirdly, the parallelism strategy in DAMASK is distributed memory using PETSc and the FFTw library, while in the Fourier-Galerkin code herein the strategy is shared memory using the Intel MKL library. Lastly, both codes are implemented in FORTRAN, compiled with level 2 optimization using Intel compiler on the same machine, and programmed with reasonably high levels of vectorization and optimized programming.

The residual norm evolution of the Fourier-Galerkin method and DAMASK are shown in Figure 4.13 (a) and (b), respectively, for load step 200 and $F_{xx} = 1.1$. The convergence rate of the Fourier-Galerkin method (Figure 4.13 (a)) appears to be almost independent of the grid resolution. Fewer Newton iterations are required at the expense of searching longer for the best CG solution during each iteration. Such cost could be reduced by adopting the
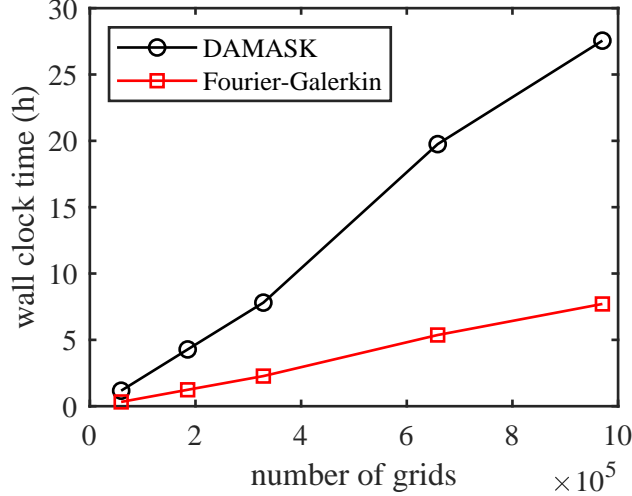
Figure 4.12: Total computational cost of Fourier-Galerkin method and DAMASK for same convergence criteria and tolerance.

inexact Newton strategy as shown in Section 4.4.2. Quadratic convergence rate is achieved because of the consistent linearization of the governing equation (4.8a) and the accurate pull-back of material stiffness from the corotational frame to the reference configuration. In comparison, DAMASK with nonlinear GMRES solver requires more Newton iterations and the convergence rate is linear. The linear solver is more robust for higher contrast problems [79] at the expense of more global iterations, which is less efficient for more involved constitutive models. It is interesting to find that the convergence behavior of DAMASK depends on the grid resolution. This observation may be explained by the efficiency of the GMRES solver. As the grid resolution increases, GMRES is applied to systems with more degrees of freedom. Therefore, more previous solutions need to be stored to achieve the same level of accuracy. Meanwhile, the Fourier-Galerkin method with CG solver possesses a convergence rate estimate depending only on the modulus contrast radio. For larger nonlinear problems, the tangent modulus at each grid point changes only slightly since similar stress states are encountered at intermediate grid points.

4.5   Conclusion

This manuscript presents a general framework that combines the FFT-based method, objective stress rate constitutive models and treatment of mixed boundary conditions. More
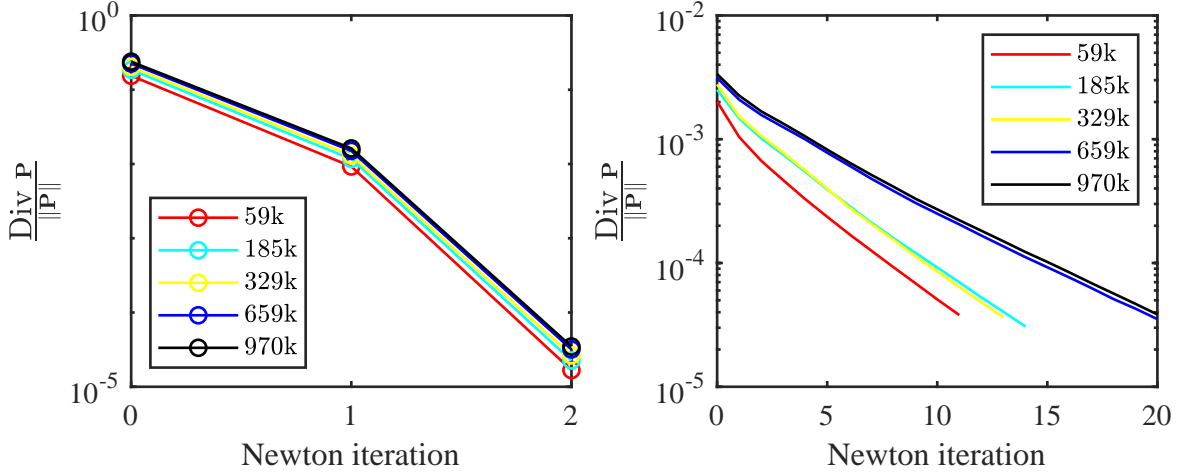
Figure 4.13: Convergence behavior of global Newton iteration when $F_{xx} = 1.1$ under constant-volume tension boundary condition ($\det \mathbf{F} = 1$). (a) Fourier-Galerkin method; (b) DAMASK.

specifically, a hypoelastic crystal plasticity (CP) framework utilizing the Green-Naghdi rate is incorporated into this FFT-based method. The algorithmic homogenized tangent stiffness for the Fourier-Galerkin method is derived in order to accommodate mixed boundary conditions. The inexact Newton method is introduced to further improve the numerical efficiency. The accuracy and computational cost of the Fourier-Galerkin method is compared with the FE method and another widely used FFT-based implementation (DAMASK). Major conclusions are summarized below:

1. The FFT-based method and FE method produce almost the same homogenized stress-strain response. Certain differences exist in the local stress distributions, especially at grain boundaries where stress concentrations exist.

2. The convergence rate of the global Newton iteration for the FFT-based method is between superlinear and quadratic, indicating that both the local and homogenized tangent stiffness are consistent.

3. The inexact Newton method can reduce the total computational cost by about 25%. More sophisticated strategies to balance the convergence progress of the linear solver and the nonlinear solver could further improve the method's efficiency.

4. The computational cost of the Fourier-Galerkin method versus the number of grid points is approximately linear. This cost is much less compared with the FE method and other FFT-based methods. The most time consuming part is the linear solver (FFT-based method) and the factorization (FE method).

5. For modeling identical RVE, the Fourier-Galerkin method requires more CG linear solver iterations and less nonlinear Newton iterations than DAMASK in a single time step under the same convergence tolerance. This balance makes it more efficient overall than DAMASK for simulations with involved constitutive models such as CP, at the expense of robustness for solving high-contrast problems.

Future work will target the following challenges. First, preconditioning will be introduced to the Krylov subspace solver to improve the robustness of the Fourier-Galerkin method. More specifically, proper preconditioning may improve the Fourier-Galerkin method to converge for domains with infinite contrast, for example damage evolution along grain boundaries. Second, the method will be extended to become a multiscale FE-FFT modeling framework. Multiscale modeling can provide essential information to explain the in-situ observed microstructure evolution, for example grain fragmentation and misorientation evolution.

Chapter 5

FE-FFT multiscale modeling

5.1 Introduction

Nowadays, there is an increasing demand to combine theory and numerical simulation to explain experimental observations. In order to directly compare experimental measurement with simulation results, image-based simulation is usually required which presents great challenge to high performance computations. Multiscale modeling method has been proposed to handle this problem [54], which is comparable to the full-field simulation but requires much less computational resources [41]. There is still a great demand to find a more efficient multiscale modeling algorithm that is able to predict local microstructure evolution of a real structure.

Thanks to the tremendous development of modern computers, multiscale modeling technique has been employed to investigate the local texture evolution. Different homogenization algorithms have been proposed to achieve this objective. The piorneering work was based on Taylor homogenization [83], where it is assumed that all grains at one macroscopic material point have the same deformation pattern. Later, grain cluster method based homogenization was proposed to relax the equal-strain assumption [88, 15]. In the grain cluster method, the total strain energy of microscale model was minimized, which induces grain interface mismatch. Extensive investigations have been performed to incorporate self-consistent method [74], eigenstrain based method [98], and finite element method [59, 19, 47] as the microscopic homogenization method to simulate local texture evolution. However, they are

either computationally expensive or not full-field simulation, making them inappropriate for large scale modeling

Recently, fast Fourier transform (FFT) based method has been combined with finite element method to solve the microscopic unit cell problem [81]. Compared with FE method, FFT-based method is more efficient especially for high-resolution simulations, and periodic boundary condition is handled naturally. The microscale FFT method can solve either phase field model [36] or crystal plasticity model [34]. Recently, the FE-FFT framework is further employed to investigate the local lattice strain evolution of aluminum alloy in a hierarchical manner [87]. But the aforementioned investigations are based on infinitesimal strain assumption. Finite strain based FE-FFT modeling is attempted in [25], and a consistent algorithm was derived to homogenize the tangent stiffness. Only heterogeneous microstructure with hyperelastic model is simulated. Till now, finite strain FE-FFT multiscale modeling is never developed to solve crystal plasticity model, which is essential for a deep understanding of the industrial processing.

The FFT-based method was originally proposed to solve stress equilibrium equation in heterogeneous elastic media [63, 64], which is later named the basic scheme. The polarization field is projected to a homogeneous reference media, and the resultant Lippman-Schwinger equation can be solved by Green's function method. The basic scheme was later reformulated to improve the numerical efficiency [16] and robustness [58]. A more general polarization scheme was later proposed [62, 65], and its numerical behavior was compared in detail with the Eyre-Milton scheme and the augmented Lagrange scheme. By realizing that the above mentioned iterative algorithm is equivalent to the Neumann expansion of the Green operator, the FFT-based governing equation was further solved by Newton-Krylov method [96], and the numerical efficiency is significantly improved. The FFT-based method was also applied to model the texture evolution of polycrystalline material [79], with different numerical solver compared to improve the robustness for high-contrast problems. The original FFT-based method was recently reformulated in a variational way, i.e. the Fourier Galerkin method, and further applied to solve infinitesimal strain [95] and finite strain [8] RVE problem. This method is independent of the reference material, thus consistent linearization is possible. The

Fourier-Galerkin method was further utilized to solve hypoelastic crystal plasticity model, and a consistent homogenized tangent stiffness was derived.

The current investigation launches from the previous work where the Fourier-Galerkin method is employed to solve a hypoelastic crystal plasticity model, and consistent homogenized tangent stiffness was derived. The novel contribution is that, for the first time, the FE-FFT multiscale modeling framework is built to solve finite strain crystal plasticity model. Furthermore, the current FE-FFT multiscale modeling framework possesses several key features. It is a finite strain based hypoelastic type model, and the crystal plasticity implementation has a general interface to incorporate most existing constitutive models. Consistent linearization is derived for both macroscale and microscale Newton-Raphson iteration, so that quadratic convergence rate is achieved in both scales. The Fourier-Galerkin method is utilized as the microscale BVP solver, which is more efficient than other FFT-based methods.

This chapter is organized as follows: In Section 5.2, the finite strain Fourier-Galerkin method is reviewed, and the Green-Naghdi rate based hypoelastic crystal plasticity material model is outlined. In Section 5.3, the macroscopic finite element kinematics is introduced, and concurrent FE-FFT multiscale modeling framework is proposed. Numerical tests are used in Section 5.4 to verify and analyze the proposed multiscale modeling framework. Section 5.5 summarizes the current investigation with major conclusions.

5.2   Periodic microscale problem

The microscopic equilibrium equation is solved by the FFT-based method. The recently proposed Fourier-Galerkin method [8] is adopted, which is more efficient than other FFT-based methods. A general interface was previously proposed to connect the FFT-based method and hypoelastic elasto-plasticity model. This algorithm is briefly reviewed in this section, followed by the crystal plasticity kinetics.

5.2.1 Fourier-Galerkin method

The microscale problem is defined in the representative volume element (RVE) in reference configuration. The RVE is discretized into regular shaped grids, with periodic boundary condition prescribed. For any point within the unit cell, quasistatic equilibrium equation reads:

$$\mathrm{Div}\,\mathbf{P} = \mathbf{0} \text{ in } B, \quad \mathbf{P} \cdot \mathbf{n} - \#, \quad \langle \mathbf{F} \rangle = \bar{\mathbf{F}} \tag{5.1}$$

where Div represents the divergence with respect to the initial coordinates, $\mathbf{P}$ is the first P-K stress, and $\mathbf{n}$ is the normal direction of the unit cell surface. The surface traction is anti-periodic, as denoted by $-\#$. The volume averaged deformation gradient $\langle \mathbf{F} \rangle$ equals to the externally applied boundary condition $\bar{\mathbf{F}}$.

Then, the weak form can be derived by assuming that the displacement perturbation field is periodic and the surface traction field is anti-periodic:

$$\int_B \delta \tilde{\mathbf{F}} : \mathbf{P} \; \mathrm{d}\Omega = 0, \quad \forall \delta \tilde{\mathbf{F}} \in \mathrm{L}^2_\#, \nabla \times \delta \tilde{\mathbf{F}} = \mathbf{0}. \tag{5.2}$$

Here, the space $\mathrm{L}^2_\#$ is a square integrable periodic function field. The weight function $\tilde{\mathbf{F}}$ is an arbitrary compatible deformation gradient field, which equals to the gradient of the displacement perturbation field. Such compatible field is difficult to determine during the implementation. Fortunately, the Green operator $\mathbb{G}$ can project arbitrary second order tensor field to its curl-free part, and can be employed to release the compatibility restriction. Utilizing the self-adjoint property of the $\mathbb{G}$ operator, the weak form (5.2) can be reformulated as:

$$\int_B \delta \mathbf{F} : (\mathbb{G} * \mathbf{P}) \; \mathrm{d}\Omega = 0, \quad \forall \delta \mathbf{F} \in \mathrm{L}^2_\#. \tag{5.3}$$

Here, $*$ represents convolution operation which can be conveniently calculated in the Fourier space. The new weight function $\mathbf{F}$ is arbitrary second order tensor field without having to be compatible. The weak (5.3) can be further discretized by trigonometric polynomials. After discretization by trigonometric polynomial function and performing numerical integration

using trapezoid rule, we get the following discretized form:

$$\mathbb{G} * \mathbf{P} = \mathbf{0} \tag{5.4}$$

which is a nonlinear equation defined on all the grid points This equation (5.4) can be solved by Newton-Raphson method considering the linear property of the $\mathbb{G}$ operator:

$$\mathbb{G} * \left(\mathbf{A}^{(i)} : \Delta \mathbf{F}^{(i+1)} \right) = -\mathbb{G} * \mathbf{P}^{(i)}. \tag{5.5}$$

Here, $\mathbf{A}^{(i)}$ is the material point tangent stiffness at the i th iteration. This equation can be efficiently solved by conjugate gradient method.

5.2.2 Crystal plasticity

This section introduces an incrementally objective crystal plasticity model based on Green-Naghdi rate. The elastic-plastic constitutive relation is defined in the current configuration:

$$\check{\boldsymbol{\sigma}} = \mathbf{C} : \left(\mathbf{D} - \mathbf{R}\mathbf{d}^p\mathbf{R}^T \right) - \mathbf{R}\mathbf{w}^p\mathbf{R}^T\boldsymbol{\sigma} + \boldsymbol{\sigma}\mathbf{R}\mathbf{w}^p\mathbf{R}^T = \dot{\boldsymbol{\sigma}} + \boldsymbol{\sigma}\boldsymbol{\Omega} - \boldsymbol{\Omega}\boldsymbol{\sigma} \tag{5.6}$$

where $\check{\boldsymbol{\sigma}}$ is Green-Naghdi rate, $\mathbf{D} = (\nabla\mathbf{v} + \mathbf{v}\nabla)/2$ is the strain rate, and $\mathbf{R}$ is the rotation tensor. The plastic velocity gradient $\mathbf{l}^p = \mathbf{d}^p + \mathbf{w}^p = \dot{\mathbf{F}}^p\mathbf{F}^{p-1}$ can be decomposed into the symmetric part $\mathbf{d}^p$ and the skew symmetric part $\mathbf{w}^p$. The spin tensor $\boldsymbol{\Omega} = \dot{\mathbf{R}}\mathbf{R}^T$. Material integration can be performed conveniently when the elastic-plastic relation is pulled back to the unrotated configuration:

$$\dot{\mathbf{t}} = \mathbf{C}_0 : \left(\mathbf{d} - \bar{\mathbf{d}}^p \right) + \mathbf{R}\bar{\mathbf{w}}^p\mathbf{R}^T\mathbf{t} - \mathbf{t}\mathbf{R}\bar{\mathbf{w}}^p\mathbf{R}^T \tag{5.7}$$

where $\mathbf{C}_0$ is the elastic stiffness tensor in unrotated configuration. The unrotated strain rate $\mathbf{d} = \mathbf{R}^T\mathbf{D}\mathbf{R}$. The plastic velocity gradient $\mathbf{d}^p$ is the summation of shear strain on each slip

system:

$$\mathbf{d}^p = \sum_{s=1}^{n_{slip}} \dot{\gamma}^{(s)} \mathbf{R}^{pT} \tilde{\mathbf{m}}^{(s)} \mathbf{R}^p, \quad \tilde{\mathbf{m}}^{(s)} = \mathrm{sym}\left(\tilde{\mathbf{b}}^{(s)} \otimes \tilde{\mathbf{n}}^{(s)}\right) \tag{5.8}$$

$$\mathbf{w}^p = \sum_{s=1}^{n_{slip}} \dot{\gamma}^{(s)} \mathbf{R}^{pT} \tilde{\mathbf{q}}^{(s)} \mathbf{R}^p, \quad \tilde{\mathbf{q}}^{(s)} = \mathrm{skew}\left(\tilde{\mathbf{b}}^{(s)} \otimes \tilde{\mathbf{n}}^{(s)}\right) \tag{5.9}$$

where $\dot{\gamma}^{(s)}$ is the shear strain rate on slip system (s), and the slip direction and slip system normal direction is represented by $\tilde{\mathbf{b}}^{(s)}$ and $\tilde{\mathbf{n}}^{(s)}$, respectively. The shear strain rate $\dot{\gamma}^{(s)}$ is determined by the resolved shear stress $\tau^{(s)}$ and slip system resistance. Without loss of generality, the classical Voce model is used in the current investigation:

$$\dot{\gamma}^{(s)} = \frac{\dot{\gamma}_0}{\tilde{\tau}} \left| \frac{\tau^{(s)}}{\tilde{\tau}} \right|^{n-1} \tau^{(s)}. \tag{5.10}$$

Here, $\tilde{\tau}$ is the hardening variable, $\dot{\gamma}_0$ is the reference strain rate, and n is the strain rate sensitivity coefficient. The hardening variable is decomposed into the intrinsic part τ_y and the extrinsic part $\bar{\tau}$, which evolves as the shear strain increases:

$$\tilde{\tau} = \tau_a + \tau_y(T, \dot{\varepsilon}) \frac{\mu(T)}{\mu_0} + \bar{\tau}(\varepsilon_p, T, \dot{\varepsilon}) \frac{\mu(T)}{\mu_0} \tag{5.11a}$$

$$\tau_y(T, \dot{\varepsilon}) = \hat{\tau}_y \left[1 - \left(\frac{kT}{\mu(T)b^3 g_{0,y}} \ln \frac{\dot{\varepsilon}_{0,y}}{\dot{\gamma}_0} \right)^{1/q_y} \right]^{1/p_y} \tag{5.11b}$$

$$\tau_v(T, \dot{\varepsilon}) = \hat{\tau}_v \left[1 - \left(\frac{kT}{\mu(T)b^3 g_{0,v}} \ln \frac{\dot{\varepsilon}_{0,v}}{\dot{\gamma}_0} \right)^{1/q_v} \right]^{1/p_v} \tag{5.11c}$$

$$\frac{d\bar{\tau}}{dt} = \theta_0 \left(1 - \frac{\bar{\tau}}{\tau_v(T, \dot{\varepsilon})} \right)^m \sum_{s=1}^{n_{slip}} |\dot{\gamma}^{(s)}| \tag{5.11d}$$

Detailed explanation of the material parameters can be found in [51]. The material parameters used in this investigation is shown in Table 5.1.

91

Table 5.1: Material parameters for the MTS model throughout this investigation

Elastic		Yield		Saturation		MTS model	
E	78.8 Gpa	$\hat{\tau}_y$	155 MPa	$\hat{\tau}_y$	25 MPa	τ_a	0.0 MPa
ν	0.33	$g_{0,y}$	0.007808	$g_{0,v}$	0.0048	n	20
μ_0	29.6 GPa	p_y	0.5	p_v	0.5	b	3.5×10^{-7} mm
D_0	0.0 MPa	q_y	2	q_v	2	m	1
T_0	204 K	$\varepsilon_{0,y}$	1.0×10^{13}	$\varepsilon_{0,v}$	1.0×10^7	θ_0	180.0 MPa

5.3 Macroscopic boundary value problem and concurrent coupling

In this section, the total Lagrangian formulation for solving macroscopic boundary value problems is first summarized. The macroscale framework is traditional finite element method, except that the material response is updated through an RVE problem. The coupling of macroscale and microscale response is achieved according to the Hill-Mandel principle [9], which is introduced next.

5.3.1 Macroscale finite element problem

Total Lagrangian formulation of finite element is adopted here, which is a natural choice to be consistent with the FFT-based method. The quantities with superscript M on the right means it is defined in macroscale. The equilibrium equation is defined in the reference configuration: The strong form (5.12a):

$$\text{Div } \mathbf{P}^M + \rho_0^M \mathbf{B}^M = \mathbf{0} \tag{5.12a}$$

$$\boldsymbol{\phi}^M = \bar{\boldsymbol{\phi}}^M \quad \text{on } \Gamma^u \tag{5.12b}$$

$$\mathbf{P}^M \cdot \mathbf{N}^M = \mathbf{T}^M \quad \text{on } \Gamma^\sigma \tag{5.12c}$$

where ρ_0^M is the initial density, $\mathbf{P}^M$ is the first Piola-Kirchhoff stress, $\mathbf{B}^M$ represents the body force, and $\boldsymbol{\phi}^M$ maps the initial coordinate $\mathbf{X}$ to the current coordinate $\mathbf{x}$. The essential boundary condition $\bar{\boldsymbol{\phi}}^M$ is defined on Γ^u, while the natural boundary condition $\mathbf{T}^M$ is defined

on Γ^σ. The equivalent weak form of the equilibrium equation (5.12a) is derived as:

$$\int_\Omega \nabla \mathbf{w}^M : \mathbf{P}^M \ \mathrm{d}\Omega - \int_\Omega \mathbf{w}^M \cdot \rho_0^M \mathbf{B}^M \ \mathrm{d}\Omega - \int_{\Gamma^\sigma} \mathbf{w}^M \cdot \mathbf{T}^M \ \mathrm{d}A = 0 \qquad (5.13)$$

where the arbitrary displacement perturbation field $\mathbf{w}$ is square integrable. To solve the weak form (5.13) using finite element method, the displacement field is discretized using finite element shape function:

$$\int_\Omega \nabla \mathbf{N}^T : \mathbf{P} \ \mathrm{d}\Omega - \int_\Omega \mathbf{N}^T \cdot \rho_0^M \mathbf{B}^M \ \mathrm{d}\Omega - \int_{\Gamma^\sigma} \mathbf{N}^T \cdot \mathbf{T}^M \ \mathrm{d}A = 0 \qquad (5.14)$$

where $\mathbf{N}$ is the finite element shape function. In this way, the unknown continuous displacement field satisfying the equilibrium equation is relaxed to a vector of unknown nodal displacement defined at the finite element nodes. The nonlinear equation (5.14) can be solved by Newton-Raphson method. By doing so, the linearized form of (5.14) is required:

$$\left[\int_\Omega \nabla \mathbf{N}^T : \mathbf{A} \nabla \mathbf{N} \ \mathrm{d}\Omega \right] \Delta \mathbf{u} = \mathbf{f}_{ext} - \mathbf{f}_{int} \qquad (5.15a)$$

$$\mathbf{f}_{ext} = \int_\Omega \mathbf{N}^T \cdot \rho_0^M \mathbf{B}^M \ \mathrm{d}\Omega + \int_{\Gamma^\sigma} \mathbf{N}^T \cdot \mathbf{T}^M \ \mathrm{d}A \qquad (5.15b)$$

$$\mathbf{f}_{int} = \int_\Omega \nabla \mathbf{N}^T : \mathbf{P} \ \mathrm{d}\Omega \qquad (5.15c)$$

where $\Delta \mathbf{u}$ is the displacement of the current Newton iteration, $\mathbf{f}_{int}$ is the internal force vector, and $\mathbf{f}_{ext}$ is the external force vector.

5.3.2 Concurrent multiscale algorithm

The schematic of concurrent multiscale framework is shown in Figure 5.1. The macroscopic stress $\mathbf{P}^M$ and strain $\mathbf{F}^M$ are defined as the volume average of corresponding microscopic quantities:

$$\mathbf{P}^M = \langle \mathbf{P} \rangle, \quad \mathbf{F}^M = \langle \mathbf{F} \rangle. \qquad (5.16)$$
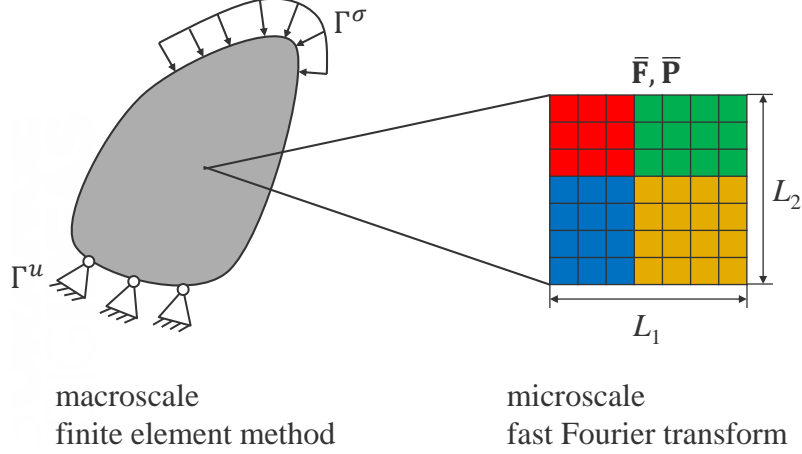
Figure 5.1: Schematic of FE-FFT multiscale modeling framework.

This coupling follows the Hill-Mandel principle, where the macroscale stress power equals to the microscale stress power:

$$\mathbf{P}^M : \dot{\mathbf{F}}^M = \langle \mathbf{P} : \dot{\mathbf{F}} \rangle. \tag{5.17}$$

However, to enable the macroscale Newton iteration, the homogenized tangent stiffness should be provided by the RVE problem. In the current investigation, the algorithmic homogenized stiffness is calculated analytically, as proposed previously, by solving the following equation:

$$\mathbb{G} * \left(\mathbf{A} : \frac{\partial \tilde{\mathbf{F}}}{\partial \bar{\mathbf{F}}} \right) = -\mathbb{G} * \mathbf{A} \tag{5.18}$$

under the constraint

$$\frac{1}{V} \int_B \frac{\partial \tilde{\mathbf{F}}}{\partial \bar{\mathbf{F}}} dV = \mathbf{0}. \tag{5.19}$$

Here, $\mathbf{A}$ is the material point tangent stiffness, $\bar{\mathbf{F}}$ is the average strain acting on the unit cell, and $\tilde{\mathbf{F}}$ is the strain perturbation caused by $\bar{\mathbf{F}}$. After solving equation (5.18) for $\partial \tilde{\mathbf{F}}/\partial \bar{\mathbf{F}}$, the homogenized tangent stiffness can be reconstructed by noting that

$$\bar{\mathbf{A}} = \left\langle \mathbf{A} : \frac{\partial \tilde{\mathbf{F}}}{\partial \bar{\mathbf{F}}} \right\rangle. \tag{5.20}$$

The algorithm of the concurrent multiscale modeling is shown in Algorithm 1.

Algorithm 1: Concurrent FE-FFT multiscale modeling

---

1 **for** $n \leftarrow 1$ **to** nstep **do**
2   **while** $\|\mathbf{f}^{int} - \mathbf{f}^{ext}\| < $ *tol.* **do**
3   assemble
4          $\Delta \mathbf{u}$
5   call `FFT_finite_3d`($\bar{\mathbf{F}}_{n+1}$, $\bar{\mathbf{F}}_n$, $\mathbf{F}_n$, $\mathbf{t}_n$, *history*)
6   calculate $\mathbf{f}^{int}$
7   **end**
8 **end**
9
10 **Function** `FFT_finite_3d`($\bar{\mathbf{F}}_{n+1}$, $\bar{\mathbf{F}}_n$, $\mathbf{F}_n$, $\mathbf{t}_n$, *history*):
11   **while** $R > $ tol. **do**
12   update $\mathbf{P}_{n+1}$: $\mathbf{P}_{n+1} = f\left(\mathbf{F}_{n+1}, \mathbf{P}_n, \text{history}\right)$
13   solve for $\Delta\tilde{\mathbf{F}}$: $\mathbb{G} * \left(\mathbf{A}_{n+1} : \Delta\tilde{\mathbf{F}}\right) = -\mathbb{G} * \mathbf{P}_{n+1}$
14   update $\mathbf{F}_{n+1}$: $\mathbf{F}_{n+1} = \mathbf{F}_{n+1} + \Delta\tilde{\mathbf{F}}$
15   update residual: $R = \|\Delta\tilde{\mathbf{F}}\|$
16   **end**
17 **return**

5.4   Numerical results and discussion

In this section, a one-element simulation is performed to illustrate the capability of the current FE-FFT multiscale modeling framework. The homogenized stress-strain response is presented, together with local stress distribution in microscale. Also, the convergence behavior of the finite element problem is analyzed.

5.4.1   Single element verification

A single element simulation is used to verify the multiscale modeling implementation. In the macroscale, uniaxial tension boundary condition is applied to a hexagonal element with 8 integration points. All integration points have the same initial microstructure, which is represented by an RVE problem with $3 \times 3 \times 3$ grid points as shown in Figure 5.2. Each unit cell contains two grains with the initial orientation shown in Figure 5.2. Mechanical threshold (MTS) model is used as the constitutive relation, with the material parameters shown in Table 5.1.
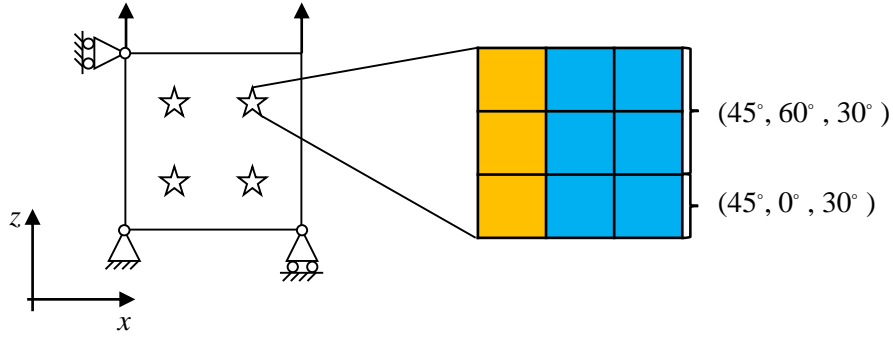
Figure 5.2: Example of FE-FFT multiscale modeling.
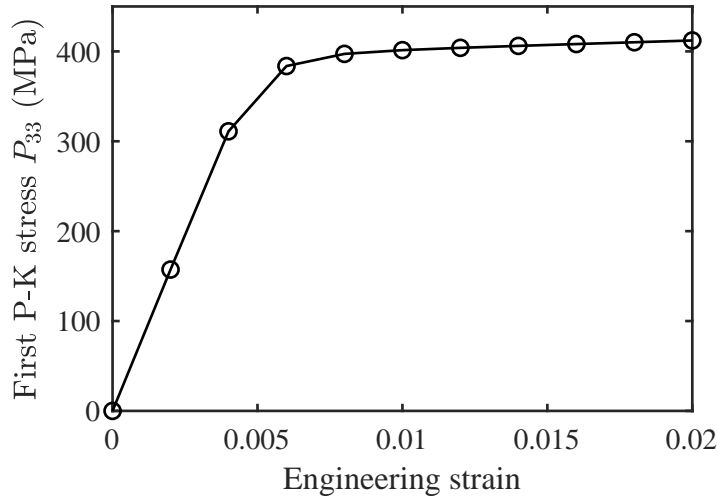
Figure 5.3: Stress strain curve of FE-FFT multiscale modeling.

The homogenized stress-strain curve is shown in Figure 5.3. The plastic strain behavior of the MTS model is captured in the stress strain response. Figure 5.4 shows the unrotated Cauchy stress distribution within the unit cell. It is observed that the heterogeneous behavior of polycrystalline material is well captured. Grain with stiffer initial orientation carries more loading under the uniaxial boundary condition, and stress jump occurs at the grain boundary.

The convergence progress of the macroscopic Newton iteration is shown in Figure 5.5. Relative residual evolution of four conditions are compared, including small strain increment at smaller strain (Figure 5.5 (a)), small strain increment at larger strain (Figure 5.5 (b)), large strain increment at smaller strain (Figure 5.5 (c)), and large strain increment at larger strain (Figure 5.5 (d)). Three different tangent stiffness are compared. In all the figures, 'symmetric' represents algorithmic homogenized tangent
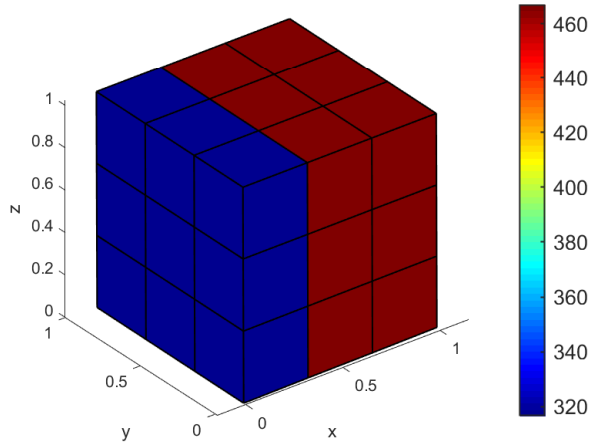
Figure 5.4: Unrotated Cauchy stress of FE-FFT multiscale modeling.

stiffness calculated from symmetric material tangent stiffness, 'unsymmetric' represents algorithmic homogenized tangent stiffness calculated from unsymmetric material tangent stiffness, and 'finite difference' means the macroscopic tangent stiffness is calculated using finite difference method. The symmetric material tangent stiffness is adopted in finite element software WARP3D to reduce the required memory [12]. It is observed that when the strain increment is about 0.002, all three tangent stiffness results into the same convergence rate, which is super-linear. However, if the strain increment is 0.02, it is observed that the homogenized tangent stiffness based on the symmetric material stiffness results in linear convergence rate. The convergence rate can be improved by either using finite difference method, or remove the symmetry assumption of the material tangent stiffness.

5.5 Conclusion

In this work, the concurrent FE-FFT multiscale modeling framework is derived and implemented. The kinematics in both scales are finite strain based, making it suitable to modeling the realistic thermal-mechanical processing at large strains. In the macroscale, total Lagrangian formulation is employed, and the stress updated is achieved by solving an microscale RVE problem using FFT-based method. Major conclusions are summarized below:

97
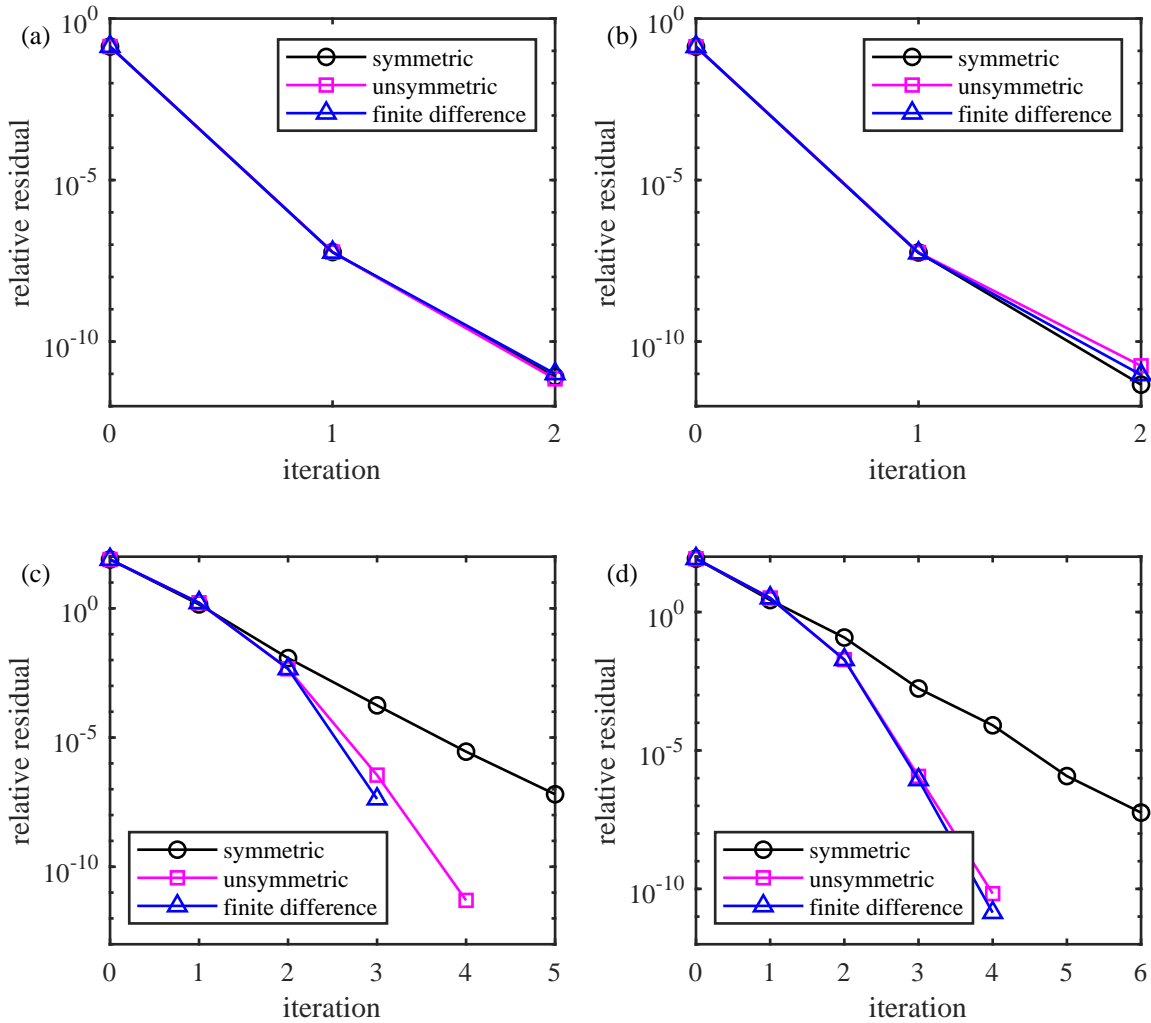
Figure 5.5: Convergence progress of macroscopic finite element iteration. (a) Small strain increment $\Delta F_{zz} = 0.002$, step 5 $F_{zz} = 1.01$ (b) Small strain increment $\Delta F_{zz} = 0.002$, step 10 $F_{zz} = 1.02$ (c) Large strain increment $\Delta F_{zz} = 0.02$, step 5 $F_{zz} = 1.1$ (d) Large strain increment $\Delta F_{zz} = 0.02$, step 10 $F_{zz} = 1.2$

1. The homogenized stress-strain response and the local plastic anisotropy is well captured simultaneously by the concurrent FE-FFT multiscale modeling framework.

2. The convergence rate of the macroscopic Newton iteration is linear, even with consistent homogenized tangent stiffness. Further investigation is required to improve this convergence rate to quadratic.

Chapter 6

Concluding Remarks and Future Work

6.1　Concluding Remarks

As concluding remarks, the objective of this dissertation is to investigate the effect of processing parameters on the breakdown efficiency of microtextured regions (MTRs). The breakdown efficiency usually depends on the loading path, the morphology of microtextured regions, and its position within the specimen. The effect of loading direction is first investigated, where idealized MTRs with pure initial orientation is constructed for crystal plasticity finite element simulations. Two extensions are performed later to take into account the influence from realistic microstructure and β phase. In order to take into account the MTR morphology and its position within the specimen, a high-efficient FE-FFT multiscale modeling framework was derived and developed.

Significant conclusions and contributions of the present work are as follows:

- Crystal plasticity finite element method was employed to investigate the effect of loading direction on the breakdown efficiency. The original constitutive relation was extended to capture the strain softening of Ti-6242 observed above 1172 K. The previously crystal plasticity framework in WARP3D was extended such that different critical resolved stresses can be assigned to different slip systems. This feature is

100

essential for the modeling of Ti-6242, which is highly anisotropic. Another feature of the current implementation is that it provides a general interface for other crystal plasticity constitutive relations, where model dependent terms are isolated. The simulation results are validated against high-temperature compression experiments and EBSD measurement. It is found that the loading direction has a significant influence on the evolution of microtextured regions. When the compression direction is $0°$ to the billet axis, disorientation within MTRs is obvious but c-axis still remains aligned due to the competing mechanism between two prismatic slip systems. When the compression direction is $45°$ to the billet axis, lattice reorientation is obvious but the disorientation is less obvious. When compressed along the billet radial direction, the c-axis is most scattered but the extent is limited by the total plastic strain. The divergence of reorientation velocity is further presented in the Rodrigues' space to predict the MTR breakdown efficiency of arbitrary loading direction.

- Crystal plasticity modeling of α and β phase Ti-6242 of mechanical processing at high temperature is performed using the WARP3D finite element code. Mesoscale results of texture evolution in ideal-oriented microtextured regions (MTR) from previous term were used to inform microscale models of alpha particle distributions to determine the effect of heterogeneity on the MTR evolution. For the cases of strain history imposed on the microscale models, the disorientation remained small when the mesoscale disorientation was small and became larger when the mesoscale exhibited larger disorientation. Orientation gradients develop for a particular alignment. While the c-axis parallel loading produced the largest breakdown, this loading also required 50% larger stress. Preliminary studies of alpha and beta phase mechanical interaction were conducted based on material parameters fitted to data for 1173 K. Distortion of finite elements representing the softer beta phase often led to FE convergence issues and limited the maximum compressive strain achieved. Orientation of c-axis of alpha particle with respect to loading direction had a much larger effect on disorientation versus particle separation.

- A general interface between the FFT-based method and objective rate constitutive model is derived and implemented before the efficient FE-FFT multiscale modeling framework is implemented. In particular, the Green-Naghdi rate based crystal plasticity kinematics are incorporated in the Fourier-Galerkin method. The consistent homogenized tangent stiffness is derived to enable mixed boundary condition and concurrent multiscale modeling. A consistent linearization of the objective rate constitutive relation is proposed to increase the convergence rate. The idea of inexact Newton method is utilized to further improve the numerical efficiency of this framework. The implemented FFT-based method is verified against finite element method, and the numerical efficiency is compared with FE method and other FFT-based methods. It is observed that the FFT-based method and FE method have the same homogenized mechanical response, although certain discrepancy regarding the local stress distribution exists especially at the grain boundaries. The superlinear convergence rate of the stress update iterations and strain update iterations indicate that the linearization is consistent in both scales. The computational cost of the Fourier-Galerkin method is orders of magnitude less than the FE method, and about 4/5 less than other FFT-based method. The major reason for the lower computational cost is attributed to less nonlinear Newton iterations required by the Fourier-Galerkin method and material update routines.

- A concurrent FE-FFT multiscale modeling framework is derived and implemented, which is suitable to correlate macroscopic structural feature and microscopic microstructure evolution. In the macroscale, finite element with total Lagrangian formulation is utilized to solve the boundary value problems; while in the microscale, the previously developed FFT-based method is utilized to solve the unit cell problems. The key features of our implement are: (1) the coupling between two scales is consistent with algorithmic tangent stiffness; (2) the microscopic FFT-based method is efficient compared with FE method and other FFT-based methods; (3) the microscopic constitutive relation is objective rate constitutive model, so that infinitesimal constitutive relations can be incorporated with objectivity. A single

element test is performed to verify and investigate the convergence progress. The FE-FFT multiscale modeling method is capable to capture the homogenized stress-strain response, and microscale stress distribution can be capture simultaneously. However, it is found that the convergence rate of the finite element iteration is linear instead of being quadratic, which requires further investigation for improvement.

6.2 Future Work

The FE-FFT multiscale modeling framework is derived and developed in this dissertation to investigate the behavior of microtextured regions under different loading conditions. This framework is capable of correlating the mechanical behavior at different length scales, and is potential for further application to explain microstructure evolution under macroscopic boundary conditions. A selection of the possible next steps is outlined in the following sections.

6.2.1 High performance FE-FFT implementation

The current FE-FFT multiscale modeling framework is implemented serially in MATLAB, limiting its ability to simulate realistic structures with more degrees of freedom. A natural extension of this dissertation is to transfer the developed multiscale modeling framework to a high-performance computing environment. Message Passing Interface (MPI) parallel programming will significantly improve the speed of the code, where the finite element problem is solved by the master node while the unit cell problems are solved by the slave nodes. Fortunately, a widely used finite element code, FEAP, enables such implementation with simple interface for unit cell problem. Similar implementation is achieved in [34], but it is based on infinitesimal strain assumption.

Two aspects will be focused regarding the development of highly-efficient multiscale modeling framework and its parallel efficiency. First, novel parallel programming strategy will be employed to improve the efficiency of this framework. The basic parallel unit is finite element instead of integration point, which will reduce the communication cost between different nodes [47]. The parallel efficiency will also be investigated, i.e. the relationship

between CPU time and total number of CPUs. Second, the numerical behavior of this framework will also be investigated, namely the numerical stability of FFT-based method for high-contrast problem under large strains.

6.2.2 Influence of MTR morphology and position on its breakdown efficiency

The developed FE-FFT multiscale modeling framework can also be applied to investigate the influence of MTR morphology and its position on the breakdown efficiency. The MTR morphology is a microscale feature of the material, while its position within the specimen is a macroscopic feature. The multiscale modeling technique is a ideal platform for analyzing such problems with acceptable computational cost.

It is expected that using this numerical technique, a optimal strain path to break down the MTRs will be predicted instead of only loading directions in Chapter 2. The strain path does not have to be monotonic; for example, the billet can be first rolled in one direction and then rolled in another direction to achieve an optimal breakdown efficiency. The multiscale modeling is able to quantitatively suggest when to change the strain path and which strain path should be chosen. Furthermore, previous experiments suggest that the breakdown efficiency of MTRs also depends on its morphology [4] and its position within the specimen [22]. This effect is also expected to be captured by this multiscale modeling framework.

One major assumption of this dissertation is that α phase controls the local deformation distribution and β phase is negligible at the processing temperature. This is true for lower processing temperatures in the α/β region. If the processing temperature further increases, the effect of β matrix should be considered which brings more numerical challenges. The major challenge is that Lagrangian mesh is not capable to capture the large strain gradient generated when hard α_p particles are embedded in soft β phase. More sophisticated numerical strategies are required to overcome this challenge.

Bibliography

[1] Babu, B. and Lindgren, L.-E. (2013). Dislocation density based model for plastic deformation and globularization of Ti-6Al-4V. *International Journal of Plasticity*, 50:94–108. 10

[2] Bache, M., Cope, M., Davies, H., Evans, W., and Harrison, G. (1997). Dwell sensitive fatigue in a near alpha titanium alloy at ambient temperature. *International Journal of Fatigue*, 19(93):83–88. 2, 8, 9

[3] Bantounas, I., Lindley, T. C., Rugg, D., and Dye, D. (2007). Effect of microtexture on fatigue cracking in Ti6Al4V. *Acta Materialia*, 55(16):5655–5665. 24, 29

[4] Bieler, T. R. and Semiatin, S. L. (2002). The origins of heterogeneous deformation during primary hot working of Ti6Al4V. *International Journal of Plasticity*, 18(9):1165–1189. 3, 4, 9, 10, 29, 37, 41, 45, 104

[5] Brisard, S. and Dormieux, L. (2010). FFT-based methods for the mechanics of composites: A general variational framework. *Computational Materials Science*, 49(3):663–671. 5, 56

[6] Choi, Y. S., Groeber, M. A., Turner, T. J., Dimiduk, D. M., Woodward, C., Uchic, M. D., and Parthasarathy, T. A. (2012). A crystal-plasticity FEM study on effects of simplified grain representation and mesh types on mesoscopic plasticity heterogeneities. *Materials Science and Engineering: A*, 553:37–44. 25

[7] de Geus, T. W. J. and Vondřejc, J. (2017). GooseFFT. http://goosefft.geus.me. 81

[8] de Geus, T. W. J., Vondřejc, J., Zeman, J., Peerlings, R. H. J., and Geers, M. G. D. (2017). Finite strain FFT-based non-linear solvers made simple. *Computer Methods in Applied Mechanics and Engineering*, 318(Supplement C):412–430. 5, 56, 57, 70, 87, 88

[9] De Souza Neto, E. A., Blanco, P. J., Sánchez, P. J., and Feijóo, R. (2015). An rve-based multiscale theory of solids with micro-scale inertia and body force effects. *Mechanics of Materials*, 80:136–144. 92

[10] Deka, D., Joseph, D. S., Ghosh, S., and Mills, M. J. (2006). Crystal plasticity modeling of deformation and creep in polycrystalline Ti-6242. *Metallurgical and Materials Transactions A*, 37(5):1371–1388. 11, 12, 14, 15, 19, 45, 46

[11] Dodds, R. (2014a). WARP3D: 3-D nonlinear finite element analysis of solids for fracture and fatigue processes. *University of Illinois at Urbana-Champaign, Urbana-Champaign, IL*. 12, 13, 24

[12] Dodds, R. (2014b). WARP3D: 3-D nonlinear finite element analysis of solids for fracture and fatigue processes. *University of Illinois at Urbana-Champaign, Urbana-Champaign, IL*. 57, 69, 97

[13] Echlin, M. P., Stinville, J. C., Miller, V. M., Lenthe, W. C., and Pollock, T. M. (2016). Incipient slip and long range plastic strain localization in microtextured Ti-6Al-4V titanium. *Acta Materialia*, 114:164–175. 24, 29

[14] Eisenlohr, P., Diehl, M., Lebensohn, R. A., and Roters, F. (2013). A spectral method solution to crystal elasto-viscoplasticity at finite strains. *International Journal of Plasticity*, 46:37–53. x, 56, 57, 62, 69, 71, 72, 79

[15] Eisenlohr, P., Tjahjanto, D., Hochrainer, T., Roters, F., and Raabe, D. (2009). Texture prediction from a novel grain cluster-based homogenization scheme. *International journal of material forming*, 2(1):523. 86

[16] Eyre, D. J. and Milton, G. W. (1999). A fast numerical scheme for computing the response of composites using grid refinement. *The European Physical Journal-Applied Physics*, 6(1):41–47. 5, 56, 87

[17] Fan, X. and Yang, H. (2011). Internal-state-variable based self-consistent constitutive modeling for hot working of two-phase titanium alloys coupling microstructure evolution. *International Journal of Plasticity*, 27(11):1833–1852. 10

[18] Fish, J. and Shek, K. (1999). Computational aspects of incrementally objective algorithms for large deformation plasticity. *International Journal for numerical methods in engineering*, 44(6):839–851. 67

[19] Fritzen, F. and Hodapp, M. (2016). The finite element square reduced (FE2R) method with gpu acceleration: towards three-dimensional two-scale simulations. *International Journal for Numerical Methods in Engineering*, 107(10):853–881. 86

[20] Germain, L., Gey, N., Humbert, M., Bocher, P., and Jahazi, M. (2005). Analysis of sharp microtexture heterogeneities in a bimodal IMI 834 billet. *Acta Materialia*, 53(13):3535–3543. 2, 3, 9, 10

[21] Germain, L., Gey, N., Humbert, M., Vo, P., Jahazi, M., and Bocher, P. (2008). Texture heterogeneities induced by subtransus processing of near α titanium alloys. *Acta Materialia*, 56(16):4298–4308. 2, 3, 9, 10

[22] Gey, N., Bocher, P., Uta, E., Germain, L., and Humbert, M. (2012). Texture and microtexture variations in a near-α titanium forged disk of bimodal microstructure. *Acta Materialia*, 60(6):2647–2655. 3, 4, 10, 41, 104

[23] Ghosh, S., Shahba, A., Tu, X., Huskins, E. L., and Schuster, B. E. (2016). Crystal plasticity fe modeling of ti alloys for a range of strain-rates. part ii: Image-based model with experimental validation. *International Journal of Plasticity*, 87(Supplement C):69–85. 10

[24] Glavicic, M. G., Bartha, B. B., Jha, S. K., and Szczepanski, C. J. (2009). The origins of microtexture in duplex Ti alloys. *Materials Science and Engineering: A*, 513:325–328. 2, 3, 9, 10

[25] Göküzüm, F. S. and Keip, M.-A. (2018). An algorithmically consistent macroscopic tangent operator for FFT-based computational homogenization. *International Journal for Numerical Methods in Engineering*, 113(4):581–600. 5, 62, 63, 87

[26] Healy, B. and Dodds, R. (1992). A large strain plasticity model for implicit finite element analyses. *Computational Mechanics*, 9(2):95–112. 67

[27] Heckel, T., Tovar, A. G., and Christ, H.-J. (2010). Fatigue of the near-alpha Ti-alloy Ti6242. *Experimental Mechanics*, 50(4):483–489. 8

[28] Kabel, M., Böhlke, T., and Schneider, M. (2014). Efficient fixed point and Newton-Krylov solvers for FFT-based homogenization of elasticity at large deformations. *Computational Mechanics*, 54(6):1497–1514. 56

[29] Kabel, M., Fliegener, S., and Schneider, M. (2016). Mixed boundary conditions for FFT-based homogenization at finite strains. *Computational Mechanics*, 57(2):193–210. 57, 64

[30] Khan, A. S., Kazmi, R., and Farrokh, B. (2007). Multiaxial and non-proportional loading responses, anisotropy and modeling of ti6al4v titanium alloy over wide ranges of strain rates and temperatures. *International Journal of Plasticity*, 23(6):931–950. 10

[31] Khan, A. S., Yu, S., and Liu, H. (2012). Deformation induced anisotropic responses of ti6al4v alloy part ii: A strain rate and temperature dependent anisotropic yield criterion. *International Journal of Plasticity*, 38(Supplement C):14–26. 10

[32] Knezevic, M. and Savage, D. J. (2014). A high-performance computational framework for fast crystal plasticity simulations. *Computational Materials Science*, 83:101–106. 57

[33] Kochmann, J., Brepols, T., Wulfinghoff, S., Svendsen, B., and Reese, S. (2018). On the computation of the exact overall consistent tangent moduli for non-linear finite strain homogenization problems using six finite perturbations. In *6th European Conference on Computational Mechanics (ECCM 6)*, pages 1–12. 62

[34] Kochmann, J., Wulfinghoff, S., Ehle, L., Mayer, J., Svendsen, B., and Reese, S. (2017a). Efficient and accurate two-scale FE-FFT-based prediction of the effective material behavior of elasto-viscoplastic polycrystals. *Computational Mechanics*. 5, 87, 103

[35] Kochmann, J., Wulfinghoff, S., Ehle, L., Mayer, J., Svendsen, B., and Reese, S. (2017b). Efficient and accurate two-scale FE-FFT-based prediction of the effective material behavior of elasto-viscoplastic polycrystals. *Computational Mechanics*. 57

[36] Kochmann, J., Wulfinghoff, S., Reese, S., Mianroodi, J. R., and Svendsen, B. (2016). Two-scale FE-FFT-and phase-field-based computational modeling of bulk microstructural

evolution and macroscopic material behavior. *Computer Methods in Applied Mechanics and Engineering*, 305:89–110. 5, 87

[37] Kok, S., Beaudoin, A., and Tortorelli, D. (2002a). A polycrystal plasticity model based on the mechanical threshold. *International Journal of Plasticity*, 18(5):715–741. 19

[38] Kok, S., Beaudoin, A., and Tortorelli, D. (2002b). A polycrystal plasticity model based on the mechanical threshold. *International Journal of Plasticity*, 18(5):715–741. 67

[39] Kouznetsova, V. V. (2002). *Computational homogenization for the multi-scale analysis of multi-phase materials*. PhD thesis, Technische Universiteit Eindhoven. 62, 63

[40] Lahellec, N., Michel, J.-C., Moulinec, H., and Suquet, P. (2003). Analysis of inhomogeneous materials at large strains using fast Fourier transforms. In *IUTAM symposium on computational mechanics of solid materials at large strains*, pages 247–258. Springer. 57

[41] Lebensohn, R., Castañeda, P. P., Brenner, R., and Castelnau, O. (2011). Full-field vs. homogenization methods to predict microstructure–property relations for polycrystalline materials. In *Computational Methods for Microstructure-Property Relationships*, pages 393–441. Springer. 86

[42] Lebensohn, R. A. (2001). N-site modeling of a 3D viscoplastic polycrystal using fast Fourier transform. *Acta Materialia*, 49(14):2723–2737. 57

[43] Lebensohn, R. A., Brenner, R., Castelnau, O., and Rollett, A. D. (2008). Orientation image-based micromechanical modelling of subgrain texture evolution in polycrystalline copper. *Acta Materialia*, 56(15):3914–3926. 57

[44] Leo Prakash, D. G., Honniball, P., Rugg, D., Withers, P. J., Quinta da Fonseca, J., and Preuss, M. (2013). The effect of β phase on microstructure and texture evolution during thermomechanical processing of $\alpha + \beta$ Ti alloy. *Acta Materialia*, 61(9):3200–3213. 2, 3, 9, 10

[45] Li, H., Sun, X., and Yang, H. (2016). A three-dimensional cellular automata-crystal plasticity finite element model for predicting the multiscale interaction among heterogeneous deformation, DRX microstructural evolution and mechanical responses in titanium alloys. *International Journal of Plasticity*, 87:154–180. 10

[46] Liu, J., Khan, A. S., Takacs, L., and Meredith, C. S. (2015). Mechanical behavior of ultrafine-grained/nanocrystalline titanium synthesized by mechanical milling plus consolidation: Experiments, modeling and simulation. *International Journal of Plasticity*, 64(Supplement C):151–163. 10

[47] Lopes, I. R., Pires, F. A., and Reis, F. (2018). A mixed parallel strategy for the solution of coupled multi-scale problems at finite strains. *Computational Mechanics*, 61(1-2):157–180. 86, 103

[48] Ma, A., Roters, F., and Raabe, D. (2006a). A dislocation density based constitutive model for crystal plasticity FEM including geometrically necessary dislocations. *Acta Materialia*, 54(8):2169–2179. 19

[49] Ma, A., Roters, F., and Raabe, D. (2006b). A dislocation density based constitutive model for crystal plasticity FEM including geometrically necessary dislocations. *Acta Materialia*, 54(8):2169–2179. 67

[50] Ma, R., Pilchak, A. L., Semiatin, S. L., and Truster, T. J. (2018). Modeling the evolution of microtextured regions during α/β processing using the crystal plasticity finite element method. *International Journal of Plasticity*, 107:189–206. 57, 65, 67, 68

[51] Ma, R., Truster, T. J., Puplampu, S. B., and Penumadu, D. (2017). Investigating mechanical degradation due to fire exposure of aluminum alloy 5083 using crystal plasticity finite element method. *International Journal of Solids and Structures*. 72, 91

[52] Mainprice, D., Hielscher, R., and Schaeben, H. (2011). Calculating anisotropic physical properties from texture data using the MTEX open-source package. *Geological Society, London, Special Publications*, 360(1):175–192. 24, 46

[53] Mandal, S., Gockel, B. T., Balachandran, S., Banerjee, D., and Rollett, A. D. (2017). Simulation of plastic deformation in Ti-5553 alloy using a self-consistent viscoplastic model. *International Journal of Plasticity*. 10, 40

[54] Matou, K., Geers, M. G. D., Kouznetsova, V. G., and Gillman, A. (2017). A review of predictive nonlinear theories for multiscale modeling of heterogeneous materials. *Journal of Computational Physics*, 330(Supplement C):192–220. 4, 86

[55] Matouš, K., Geers, M. G. D., Kouznetsova, V. G., and Gillman, A. (2017). A review of predictive nonlinear theories for multiscale modeling of heterogeneous materials. *Journal of Computational Physics*, 330(Supplement C):192–220. 55

[56] Messner, M., Beaudoin, A., and Dodds, R. (2015a). Consistent crystal plasticity kinematics and linearization for the implicit finite element method. *Engineering Computations*, 32(6):1526–1548. 11, 12, 13, 14, 16, 17, 18

[57] Messner, M., Beaudoin, A., and Dodds, R. (2015b). Consistent crystal plasticity kinematics and linearization for the implicit finite element method. *Engineering Computations*, 32(6):1526–1548. 65, 66, 67, 68

[58] Michel, J. C., Moulinec, H., and Suquet, P. (1999). Effective properties of composite materials with periodic microstructure: a computational approach. *Computer Methods in Applied Mechanics and Engineering*, 172(1):109–143. 5, 56, 57, 87

[59] Miehe, C., Schröder, J., and Schotte, J. (1999). Computational homogenization analysis in finite plasticity simulation of texture development in polycrystalline materials. *Computer methods in applied mechanics and engineering*, 171(3-4):387–418. 5, 86

[60] Miller, V., Echlin, M., Beyerlein, I., and Pollock, T. (2016). Polycrystal plasticity simulation of microtextured titanium. In *Proceedings of the 13th World Conference on Titanium*, pages 209–214. John Wiley & Sons, Inc. 3, 11

[61] Mishra, N., Vondřejc, J., and Zeman, J. (2016). A comparative study on low-memory iterative solvers for FFT-based homogenization of periodic media. *Journal of Computational Physics*, 321(Supplement C):151–168. 56, 57, 74

[62] Moulinec, H. and Silva, F. (2014). Comparison of three accelerated FFT-based schemes for computing the mechanical response of composite materials. *International Journal for Numerical Methods in Engineering*, 97(13):960–985. 56, 87

[63] Moulinec, H. and Suquet, P. (1994). A fast numerical method for computing the linear and nonlinear mechanical properties of composites. *Comptes Rendus de L'Académie des Sciences. Série II, Mécanique, Physique, Chimie, Astronomie*, 318(11):1417–1423. 5, 56, 87

[64] Moulinec, H. and Suquet, P. (1998). A numerical method for computing the overall response of nonlinear composites with complex microstructure. *Computer Methods in Applied Mechanics and Engineering*, 157(1-2):69–94. 5, 56, 87

[65] Moulinec, H., Suquet, P., and Milton, G. (2018). Convergence of iterative methods based on Neumann series for composite materials: theory and practice. *International Journal for Numerical Methods in Engineering*, 114(10):1103–1130. 74, 87

[66] Nagra, J. S., Brahme, A., Lebensohn, R. A., and Inal, K. (2017). Efficient fast Fourier transform-based numerical implementation to simulate large strain behavior of polycrystalline materials. *International Journal of Plasticity*, 98:65–82. 57

[67] Pilchak, A., Szczepanski, C., Shaffer, J., Salem, A., and Semiatin, S. (2013). Characterization of microstructure, texture, and microtexture in near-alpha titanium mill products. *Metallurgical and Materials Transactions A*, 44(11):4881–4890. xi, 2, 3, 8, 9, 11, 21, 22, 23

[68] Pilchak, A. L. (2013). Fatigue crack growth rates in alpha titanium: Faceted vs. striation growth. *Scripta Materialia*, 68(5):277–280. 2, 9

[69] Pilchak, A. L., Shank, J., Tucker, J. C., Srivatsa, S., Fagin, P. N., and Semiatin, S. L. (2016). A dataset for the development, verification, and validation of microstructure-sensitive process models for near-alpha titanium alloys. *Integrating Materials and Manufacturing Innovation*, 5(1):14. xi, xii, 3, 4, 11, 19, 20, 21, 22, 31, 40

[70] Quey, R., Dawson, P., and Driver, J. (2012). Grain orientation fragmentation in hot-deformed aluminium: Experiment and simulation. *Journal of the Mechanics and Physics of Solids*, 60(3):509–524. 35, 37

[71] Quey, R., Dawson, P. R., and Barbe, F. (2011). Large-scale 3D random polycrystals for the finite element method: Generation, meshing and remeshing. *Computer Methods in Applied Mechanics and Engineering*, 200(1720):1729–1745. 71

[72] Robert, C. and Mareau, C. (2015). A comparison between different numerical methods for the modeling of polycrystalline materials with an elastic-viscoplastic behavior. *Computational Materials Science*, 103:134–144. 55

[73] Roters, F., Eisenlohr, P., Hantcherli, L., Tjahjanto, D. D., Bieler, T. R., and Raabe, D. (2010). Overview of constitutive laws, kinematics, homogenization and multiscale methods in crystal plasticity finite-element modeling: Theory, experiments, applications. *Acta Materialia*, 58(4):1152–1211. 55

[74] Segurado, J., Lebensohn, R. A., LLorca, J., and Tomé, C. N. (2012). Multiscale modeling of plasticity based on embedding the viscoplastic self-consistent formulation in implicit finite elements. *International Journal of Plasticity*, 28(1):124–140. 4, 86

[75] Seifert, T. and Maier, G. (2008). Consistent linearization and finite element implementation of an incrementally objective canonical form return mapping algorithm for large deformation inelasticity. *International journal for numerical methods in engineering*, 75(6):690–708. 67, 119

[76] Semiatin, S. and Bieler, T. (2001a). Effect of texture and slip mode on the anisotropy of plastic flow and flow softening during hot working of ti-6al-4v. *Metallurgical and Materials Transactions A*, 32(7):1787–1799. 12

[77] Semiatin, S. and Bieler, T. (2001b). Effect of texture changes on flow softening during hot working of Ti-6Al-4V. *Metallurgical and Materials Transactions A*, 32(7):1871–1875. 19, 27, 41

[78] Semiatin, S., Seetharaman, V., and Weiss, I. (1998). Hot workability of titanium and titanium aluminide alloysan overview. *Materials Science and Engineering: A*, 243(1-2):1–24. 12

[79] Shanthraj, P., Eisenlohr, P., Diehl, M., and Roters, F. (2015). Numerically robust spectral methods for crystal plasticity simulations of heterogeneous materials. *International Journal of Plasticity*, 66:31–45. 57, 81, 83, 87

[80] Smith, B. D., Shih, D. S., and McDowell, D. L. (2013). Cyclic plasticity experiments and polycrystal plasticity modeling of three distinct ti alloy microstructures. *International Journal of Plasticity*. 10

[81] Spahn, J., Andrä, H., Kabel, M., and Müller, R. (2014). A multiscale approach for modeling progressive damage of composite materials using fast Fourier transforms. *Computer Methods in Applied Mechanics and Engineering*, 268(Supplement C):871–883. 5, 87

[82] Tari, V., Lebensohn, R. A., Pokharel, R., Turner, T. J., Shade, P. A., Bernier, J. V., and Rollett, A. D. (2018). Validation of micro-mechanical FFT-based simulations using high energy diffraction microscopy on Ti-7Al. *Acta Materialia*, 154:273–283. 56

[83] Tome, C., Canova, G., Kocks, U., Christodoulou, N., and Jonas, J. (1984). The relation between macroscopic and microscopic strain hardening in fcc polycrystals. *Acta metallurgica*, 32(10):1637–1653. 4, 86

[84] Tóth, L., Neale, K., and Jonas, J. (1989). Stress response and persistence characteristics of the ideal orientations of shear textures. *Acta Metallurgica*, 37(8):2197–2210. 37

[85] Truster, T. J. and Nassif, O. (2017a). Variational projection methods for gradient crystal plasticity using Lie algebras. *International Journal for Numerical Methods in Engineering*, 110(4):303–332. 12

[86] Truster, T. J. and Nassif, O. (2017b). Variational projection methods for gradient crystal plasticity using lie algebras. *International Journal for Numerical Methods in Engineering*, 110(4):303–332. 65

[87] Upadhyay, M. V., Van Petegem, S., Panzner, T., Lebensohn, R. A., and Van Swygenhoven, H. (2016). Study of lattice strain evolution during biaxial deformation of stainless steel using a finite element and fast Fourier transform based multi-scale approach. *Acta Materialia*, 118:28–43. 87

[88] Van Houtte, P., Li, S., Seefeldt, M., and Delannay, L. (2005). Deformation texture prediction: from the taylor model to the advanced lamel model. *International Journal of Plasticity*, 21(3):589–624. 4, 86

[89] Venkatesh, V., Tamirisa, S., Sartkulvanich, J., Calvert, K., Dempster, I., Saraf, V., Salem, A., Rokhlin, S., Broderick, T., Glavicic, M., et al. (2016). ICME of microtexture evolution in dual phase titanium alloys. In *Proceedings of the 13th World Conference on Titanium*, pages 1907–1912. Wiley Online Library. 2, 9

[90] Vidyasagar, A., Tutcuoglu, A. D., and Kochmann, D. M. (2018). Deformation patterning in finite-strain crystal plasticity by spectral homogenization with application to magnesium. *Computer Methods in Applied Mechanics and Engineering*, 335:584–609. 57

[91] Vondřejc, J., Zeman, J., and Marek, I. (2014). An FFT-based Galerkin method for homogenization of periodic media. *Computers and Mathematics with Applications*, 68(3):156–173. 5, 56, 58, 59

[92] Vondřejc, J., Zeman, J., and Marek, I. (2015). Guaranteed upper-lower bounds on homogenized properties by FFT-based Galerkin method. *Computer Methods in Applied Mechanics and Engineering*, 297:258–291. 56

[93] Weiss, I., Froes, F., Eylon, D., and Welsch, G. (1986). Modification of alpha morphology in Ti-6Al-4V by thermomechanical processing. *Metallurgical and Materials Transactions A*, 17(11):1935–1947. 9

[94] Woodfield, A., Gorman, M., Corderman, R., Sutliff, J., and Yamrom, B. (1996). Titanium'95: Science and Technology. *Institute of Materials, Birmingham, UK*, pages 1116–23. 9

[95] Zeman, J., de Geus, T., Vondřejc, J., Peerlings, R. H., and Geers, M. G. (2017). A finite element perspective on nonlinear FFT-based micromechanical simulations. *International Journal for Numerical Methods in Engineering*. 5, 56, 61, 63, 87

[96] Zeman, J., Vondřejc, J., Novák, J., and Marek, I. (2010). Accelerating a FFT-based solver for numerical homogenization of periodic media by conjugate gradients. *Journal of Computational Physics*, 229(21):8065–8071. 56, 61, 74, 76, 87

[97] Zhang, H., Diehl, M., Roters, F., and Raabe, D. (2016). A virtual laboratory using high resolution crystal plasticity simulations to determine the initial yield surface for sheet metal forming operations. *International Journal of Plasticity*, 80:111–138. 57

[98] Zhang, X. and Oskay, C. (2015). Eigenstrain based reduced order homogenization for polycrystalline materials. *Computer Methods in Applied Mechanics and Engineering*, 297:408–436. 86

Appendices

A Derivation of consistent tangent stiffness for hypoelastic plastic model in reference configuration

This section presents the steps to derive the consistent tangent stiffness $\mathbf{A}$ in the reference configuration for the Green-Naghdi objective stress rate. A similar derivation process applies for Jaumann rate based hypoelastic models, where the orthogonal tensor $\mathbf{\Lambda}$ defined by $\dot{\mathbf{\Lambda}} = \mathbf{w} \cdot \mathbf{\Lambda}$ is used to construct the unrotated configuration [75]. It is assumed that the consistent elastoplastic tangent stiffness $\mathbf{c} = \mathrm{d}\mathbf{t}_{n+1}/\mathrm{d}\Delta\mathbf{d}_{n+\frac{1}{2}}$ is known. For brevity, we define the second order tensor $\mathbf{Q} = \mathbf{R}\mathbf{t}\mathbf{R}^T\mathbf{F}^{-T}$. By taking the derivative of both sides of equation (4.29), the general form of $\mathbf{A}$ reads:

$$\mathbf{A} = \frac{\mathrm{d}\mathbf{P}}{\mathrm{d}\mathbf{F}} = \mathbf{Q} \otimes \frac{\mathrm{d}J}{\mathrm{d}\mathbf{F}} + J\frac{\mathrm{d}\mathbf{Q}}{\mathrm{d}\mathbf{F}} \tag{1}$$

Here, J is the determinant of the deformation gradient. The first term in equation (1) is well established. The second term in equation (1) can be computed using the product rule:

$$\frac{\partial Q_{ij}}{\partial F_{kl}} = \frac{\partial R_{im}}{\partial F_{kl}}\left(\mathbf{t}\mathbf{U}^{-1}\right)_{mj} + R_{im}\frac{\partial t_{mn}}{\partial F_{kl}}U_{nj}^{-1} + (\mathbf{R}\mathbf{t})_{im}\frac{\partial R_{mn}^T}{\partial F_{kl}}F_{nj}^{-T} + \sigma_{im}\frac{\partial F_{mj}^{-T}}{\partial F_{kl}}. \tag{2}$$

The fourth term in equation (2) is well established. To compute the first and third term in equation (2), the derivative of the rotation matrix $\mathbf{R}$ with respect to $\mathbf{F}$ reads:

$$\frac{\partial R_{ij}}{\partial F_{kl}} = \det(\mathbf{Y})^{-1}\left[(\mathbf{R}\mathbf{Y}\mathbf{R}^T)_{ik}Y_{lj} - (\mathbf{R}\mathbf{Y})_{il}(\mathbf{R}\mathbf{Y})_{kj}\right], \quad \mathbf{Y} = (\mathrm{tr}(\mathbf{U}))\,\mathbf{I} - \mathbf{U} \tag{3}$$

where $\mathbf{U}$ is the right stretch tensor. The second term in equation (2) involves the derivative of $\mathbf{t}_{n+1}$ with respect to $\mathbf{F}_{n+1}$. According to the definition of elastoplastic tangent stiffness $\mathbf{c}$ and the strain tensor $\mathbf{d}_{n+\frac{1}{2}}$ defined in equation (4.27), the following equation can be presented:

$$\frac{\mathrm{d}\mathbf{t}_{n+1}}{\mathrm{d}\mathbf{F}_{n+1}} = \frac{\mathrm{d}\mathbf{t}_{n+1}}{\mathrm{d}\mathbf{d}_{n+\frac{1}{2}}} : \frac{\mathrm{d}\mathbf{d}_{n+\frac{1}{2}}}{\mathrm{d}\mathbf{F}_{n+1}} = \mathbf{c} : \frac{\mathrm{d}\left(\mathbf{R}_{n+\frac{1}{2}}^T\Delta\mathbf{D}_{n+\frac{1}{2}}\mathbf{R}_{n+\frac{1}{2}}\right)}{\mathrm{d}\mathbf{F}_{n+1}} \tag{4}$$

Special attention has to be paid when calculating the derivative of $\mathbf{R}_{n+\frac{1}{2}}$ with respect to $\mathbf{F}_{n+1}$

$$\frac{\partial \mathbf{R}_{n+\frac{1}{2}}}{\partial \mathbf{F}_{n+1}} = \frac{1}{2} \frac{\partial \mathbf{R}_{n+\frac{1}{2}}}{\partial \mathbf{F}_{n+\frac{1}{2}}}. \tag{5}$$

The derivative of the strain rate $\mathbf{D}_{n+\frac{1}{2}}$ with respect to the deformation gradient $\mathbf{F}_{n+1}$ reads:

$$\Delta \mathbf{D}_{n+\frac{1}{2}} = \text{sym } \Delta \mathbf{L}_{n+\frac{1}{2}}, \quad \left(\frac{\mathrm{d} \Delta \mathbf{L}_{n+\frac{1}{2}}}{\mathrm{d} \mathbf{F}_{n+1}} \right)_{ijkl} = \left(\mathbf{I} - \frac{1}{2} \Delta \mathbf{L}_{n+\frac{1}{2}} \right)_{ik} \left(\mathbf{F}_{n+\frac{1}{2}}^{-1} \right)_{lj}. \tag{6}$$

Combining equation (1), (2), (4) and (6), we can get the consistent tangent stiffness $\mathbf{A}$ in the reference configuration.

B   Mixed boundary condition algorithm

The algorithm extending the Fourier-Galerkin method to treat mixed boundary condition is shown in Algorithm 2. In this algorithm, the inner loop (strain loop) seeks the stress equilibrium state using equation (4.8a), while the outer loop (stress loop) iterates until the homogenized stress converges to the prescribed stress boundary condition.

Algorithm 2: Fourier-Galerkin method with mixed boundary condition.

---

1 **for** $n \leftarrow 1$ **to** nstep **do**

2   **if** *Strain boundary condition* **then** $\Delta\bar{\mathbf{F}} = \Delta\bar{\mathbf{F}}_{BC}$;

3   **else** $\Delta\bar{\mathbf{F}} = \bar{\mathbf{A}}_n^{-1}\Delta\bar{\mathbf{P}}_{BC}$;

4   **while** true **do**

5         $\mathbf{F}_{n+1} = \mathbf{F}_{n+1} + \Delta\bar{\mathbf{F}}$;

6   solve for $\Delta\tilde{\mathbf{F}}$: $\mathbb{G} * \left(\mathbf{A}_n : \Delta\tilde{\mathbf{F}}\right) = -\mathbb{G} * \left(\mathbf{A}_n : \Delta\bar{\mathbf{F}}\right)$;

7   update $\mathbf{F}_{n+1}$: $\mathbf{F}_{n+1} = \mathbf{F}_{n+1} + \Delta\tilde{\mathbf{F}}$;

8   **while** $R >$ tol. **do**

9   update $\mathbf{P}_{n+1}$: $\mathbf{P}_{n+1} = f\left(\mathbf{F}_{n+1}, \mathbf{P}_n, \text{history}\right)$;

10   solve for $\Delta\tilde{\mathbf{F}}$: $\mathbb{G} * \left(\mathbf{A}_{n+1} : \Delta\tilde{\mathbf{F}}\right) = -\mathbb{G} * \mathbf{P}_{n+1}$;

11   update $\mathbf{F}_{n+1}$: $\mathbf{F}_{n+1} = \mathbf{F}_{n+1} + \Delta\tilde{\mathbf{F}}$;

12   update residual: $R = \|\Delta\tilde{\mathbf{F}}\|$;

13   **end**

14         $\bar{\mathbf{P}} = \langle\mathbf{P}_{n+1}\rangle$;

15   **if** $\frac{\|\bar{\mathbf{P}}-\mathbf{P}_{BC}\|}{\|\bar{\mathbf{P}}\|} <$ tol. **then** break;

16   update $\bar{\mathbf{A}}_{n+1}$ using equation (4.15);

17   update $\Delta\bar{\mathbf{F}}$: $\Delta\bar{\mathbf{F}} = -\bar{\mathbf{A}}_{n+1}^{-1}\left(\bar{\mathbf{P}} - \mathbf{P}_{BC}\right)$;

18   **end**

19 **end**

C   Flow chart of the microstructure based simulation

In this section, the major procedures of the microstructure prediction in Chapter 2 are presented. The major objective of this section is to summarize the commonly used procedures for crystal plasticity finite element simulations, and call for possible improvements such that the efficiency and reliability of the prediction can be increased.

The first step is to choose an appropriate material model according to the deformation mechanism of this material and calibrate the material parameters. The selection of proper material model is crucial, and the researcher should fully consider the major deformation mechanism that controls the local strain, such as crystal structure, twinning, grain boundary sliding, etc. The most used material calibration is through manual adjusting according to experiment stress-strain curve. In this dissertation, the calibration process is performed based on Taylor homogenization to increase the efficiency.

The second step is to generate a statistically equivalent (or even image-based) representative volume element (RVE) for the simulation. Essential microstructure features should be captured in the RVE, for example grain size distribution, initial orientation distribution, twinning fraction, etc. In order to perform point-to-point comparison between simulation and experiment, image-based microstructure can be generated.

Lastly, the mesoscale simulations should be validated against microstructure measurement to make sure the result is reliable. Such measurement techniques include but is not limited to, average lattice orientation from X-ray diffraction, local orientation evolution from EBSD, etc. Then the simulation is believed to be reliable and can be utilized to predicted desired quantities.
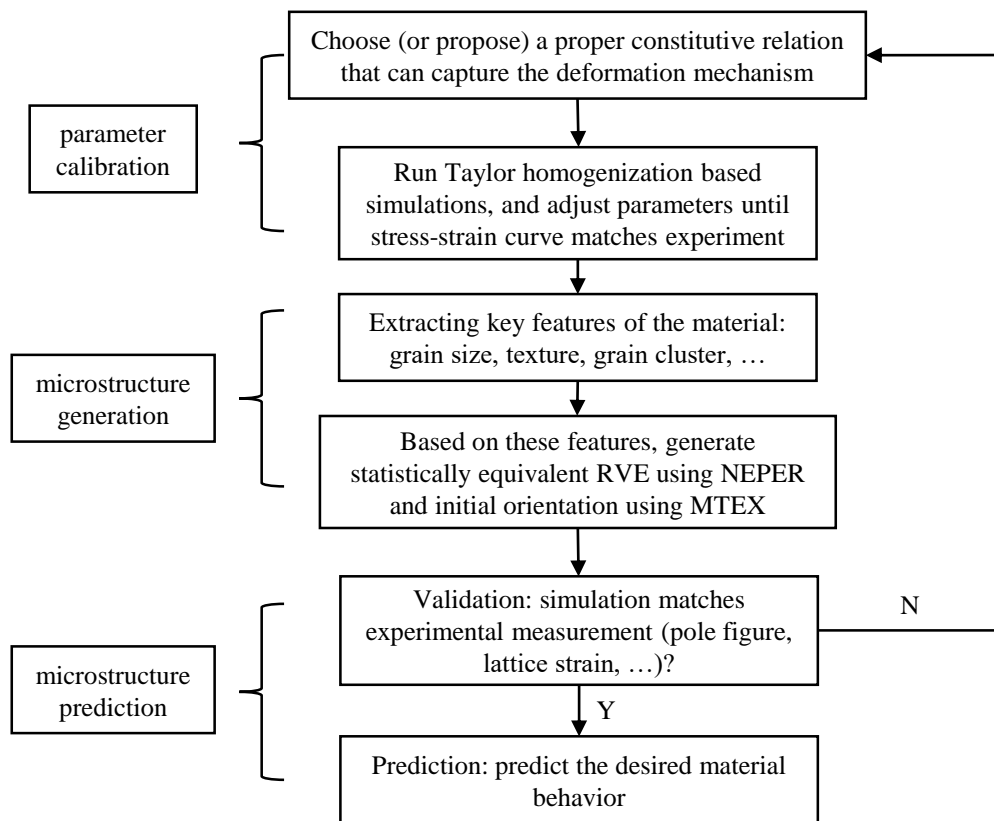
Figure C.1: Work flow of the microstructure prediction simulation.

Vita

Ran Ma was born in Harbin, China on February 15, 1990. He got his BS degree in Welding Science and Technology from Harbin Institute of Technology, China in July, 2013. He got his MS degree in Materials Processing Engineering from Harbin Institute of Technology, China in July, 2015.

Ran Ma is currently pursuing a Doctorate Degree in Civil and Environmental Engineering Department from the University of Tennessee, Knoxville. He has accepted a position as a postdoc in Department of Civil Engineering and Engineering Mechanics at Columbia University.